Multiphase Numerical Simulations of Dielectric Fluid Immersion Cooling Scenarios including Effects of Nucleation Site Density and Bubble Departure Diameter Functions

by

Jonathan Loc Nguyen

A thesis submitted to the Graduate Faculty of
Auburn University
in partial fulfillment of the
requirements for the Degree of
Master of Science

Auburn, Alabama
August 1, 2015

Keywords: numerical simulation, two-phase, dielectric fluid, electronics cooling, immersion cooling, computational fluid dynamics

Copyright 2015 by Jonathan Loc Nguyen

Approved by

Roy W. Knight, Chair, Assistant Professor of Mechanical Engineering
Sushil H. Bhavnani, Professor of Mechanical Engineering
Daniel K. Harris, Associate Professor of Mechanical Engineering

Abstract

Multiphase numerical simulations have typically been restricted to a few standard functions for key boiling parameters, such as nucleation site density and bubble departure diameter. In this study, ANSYS Icepak and ANSYS Fluent were used to model and simulate dielectric fluid immersion cooling of multichip modules in pool and flow boiling scenarios using a variety of functions for nucleation site density and bubble departure diameter. Numerical results were validated against experimental data for the same geometry and working fluid.

The pool boiling numerical model used in this study was a reduced form of an experimental setup, which consisted of four equally spaced die arranged in a square pattern and centered on a printed circuit board (PCB). The numerical model consisted of a single die and PCB vertically suspended in a large, quiescent pool of Novec 649. Heat was uniformly dissipated from the die at fluxes ranging from 3 to 12 W/cm^2. This study involved the comparison of several functions for two boiling parameters: nucleation site density and bubble departure diameter. Four combinations of the built-in functions available in Fluent were simulated with results exhibiting varying degrees of agreement with experimental data and overall demonstrating relatively unpredictable behavior. Parametric studies were performed with user-defined functions for twelve expressions for nucleation site density, six for bubble departure diameter, and a combination of the two functions. The worst results over predicted wall superheat by an average of 3.4°C for heat

fluxes in the range of 3 to 12 W/cm^2. The best agreement was seen when experimental data for bubble departure diameter was implemented as a user-defined function; these results matched experimentally measured wall superheat within 1.3°C over the same heat flux range. Other pool boiling simulations used various functional forms for nucleation site density, variation of the level of subcooling and variation of the turbulence model.

The flow boiling numerical model used in this study was based on an experimental design for a small form factor, four die cartridge module that circulated subcooled Novec 649. The experimentally designed flow distributor used to direct Novec 649 over the die and enhance convective heat transfer was also replicated in the numerical model. Built-in functions for nucleation site density and bubble departure diameter were simulated to establish a baseline comparison with experimental data followed by the user-defined functions that performed best in the pool boiling simulations. It was found that although the nucleation site density and bubble departure diameter functions resulted in good agreement under pool boiling scenarios, modifications would be needed to adapt the functions for flow boiling.

Acknowledgements

I would like to thank my advisory committee: Dr. Roy W. Knight, Dr. Sushil H. Bhavnani and Dr. Daniel K. Harris for their encouragement and guidance throughout my time as a graduate student. I would especially like to thank my primary advisor, Dr. Knight, for instilling a passion for the thermal sciences way back when I was an undergraduate in his Thermodynamics II class. I could not have hoped for a better mentor to aid in my growth as an academic and as a person.

I would also like to thank the other students in my research group for making graduate school an absolutely wonderful experience full of great memories. I would like to thank Seth Fincher, who not only laid the foundation for this study but also helped me learn a lot about modeling and simulating with ANSYS Fluent.

Last but certainly not least, I would like to thank my mother, Cam; stepfather, Don; sister, Melanie; and brother-in-law, Matt, for their endless support in everything I do. I truly appreciate everything they have done for me in the darkest and brightest moments.

Table of Contents

List of Tables

List of Figures

List of Abbreviations

Abbreviations

ALWR	advanced light water reactor
BDD	bubble departure diameter, m
BWR	boiling water reactor
CFD	computational fluid dynamics
CHF	critical heat flux, W/cm^2
CRAC	computer room air conditioner
CT	computed tomography
CWH	chilled water header
DNB	departure from nucleate boiling
GRC	Green Revolution Cooling
IGBT	insulated-gate bipolar transistors
K-I	Kocamustafaogullari-Ishii
L-C	Lemmert-Chawla
NSD	nucleation site density, m^{-2}
ONB	onset of nucleate boiling
PCB	printed circuit board
PUE	power usage effectiveness
PWR	pressurized water reactor
RNG	renormalization group

RPI	Rensselaer Polytechnic Institute
SG	steam generator
T-K	Tolubinski-Kostanchuk
TDR	turbulent dissipation rate, m^2/s^3
TKE	turbulent kinetic energy, m^2/s^2
TSP	tube support plate
UDF	user-defined function

English Letter Symbols

A	area, m^2
A_b	fractional area of influence, m^2/m^2
C_p	specific heat, J/(kg·K)
D_w	bubble departure diameter, m
f	frequency of bubble departure, s^{-1}
g	gravitational acceleration, m/s^2
h	heat transfer coefficient, $W/(m^2 \cdot K)$
h_{lv}	latent heat of vaporization, J/kg
Ja	Jacob number
K	empirical constant for area of influence
k	thermal conductivity, W/(m·K)
$\dot{m}$	mass flow rate, kg/s
Nu	Nusselt number
N_w	nucleation site density, m^{-2}

P	pressure, Pa
Pr	Prandtl number
$\dot{q}$	heat rate, W
$\vec{R}$	interaction force, N
Ra	Rayleigh number
Re	Reynolds number
r	radius of vapor bubble, m
S	source term
T	temperature, K
t	periodic time, s
V	volume, m^3
$\vec{v}$	velocity, m/s
v_f	volume fraction

Greek Letter Symbols

α	thermal diffusivity, m^2/s
ΔT	temperature difference, K
μ	dynamic viscosity, kg/(m·s)
ρ	density, kg/m^3
$\emptyset$	contact angle, degrees
σ	surface tension, N/m
$\bar{\tau}$	stress-strain tensor

Subscripts

C	convective
E	evaporative
l	liquid property
p	primary phase
pool	bulk liquid pool
Q	quenching
q	secondary phase
sat	saturation
sb	slug bubble
sub	subcooled
td	turbulent dispersion
v	vapor property
vm	virtual mass
w	wall
wl	wall lubrication

Superscripts

″	per unit area, m^{-2}
‴	per unit volume, m^{-3}

Chapter 1

INTRODUCTION

As power consumption continues to increase not only from expanding data centers, such as those used by Amazon, Facebook and Google, but also from shrinking personal electronics, the ability to provide adequate cooling continues to evolve.

On one end of the spectrum, increasing the infrastructure to create larger data centers with more storage capacity results in increased cooling requirements due to a larger total heat output. For example, in a study by Moor Insights and Strategy, a typical server rack in 2014 can consist of 40-60 servers, which is an increase from the 12-15 servers per rack several years ago [1]. In terms of energy consumption, Koomey reported a 56% increase in electricity used by worldwide data centers and a 36% increase in electricity used by US data centers between 2005 and 2010 [2]. Furthermore, Villanova University researchers found that 2% of total US energy consumption was being used by data centers in 2014; of this percentage, half was being used for cooling [3]. Traditionally, data centers have been cooled using computer room air conditioners (CRACs); however, opportunities exist for more energy efficient, localized liquid immersion cooling.

On the other end of the spectrum, decreasing the size of personal electronics results in more heat-generating components over a given area, i.e. a larger power density. In 1965, Moore predicted the number of transistors on integrated circuits would double

nearly every two years; this is known as Moore's Law [4]. This growth in power density is not limited to personal electronics however, as server racks within data centers are also affected by Moore's Law. Regardless of the electronic equipment scale, the increasing power consumption and power density trends require improved cooling techniques beyond traditional air cooling methods.

1.1 Motivating Factors for Multiphase Liquid Immersion Cooling

Air cooling has been sufficient in previous years; however, as chip power dissipation continues to increase as projected by Moore's Law, new methods are required. Heat transfer using liquids, such as water, is more effective than using gases, such as air, due to the higher thermal conductivity. Although water would provide more effective cooling, for immersion cooling of electronics, nonconducting liquids known as dielectric fluids are needed. Examples include various mineral oils, fluorocarbon liquids and engineered fluids, such as Novec 649 manufactured by 3M.

Figure 1.1 from Geisler, et al. [5] shows the relative cooling capabilities of various fluids and heat transfer mechanisms based on the available driving temperature difference. As surface heat fluxes continue to rise, immersion in and boiling of fluorocarbons can provide the necessary cooling without requiring excessively large temperature rises. While exact energy savings will vary based on the existing infrastructure or implementation, several companies have advertised significant improvements with use of immersion cooling in their products. For example, 3M claims a 90% reduction in power usage over conventional air cooling techniques through the use of their passive, two-phase immersion method using their propriety dielectric fluid, Novec 649 [6]. Green Revolution Cooling (GRC) specializes in immersion cooling using

mineral oil baths. For data centers, GRC claims a 90-95% reduction in energy used for cooling [7] and for Bitcoin mining servers, GRC claims a 42% reduction in total power consumption [8].

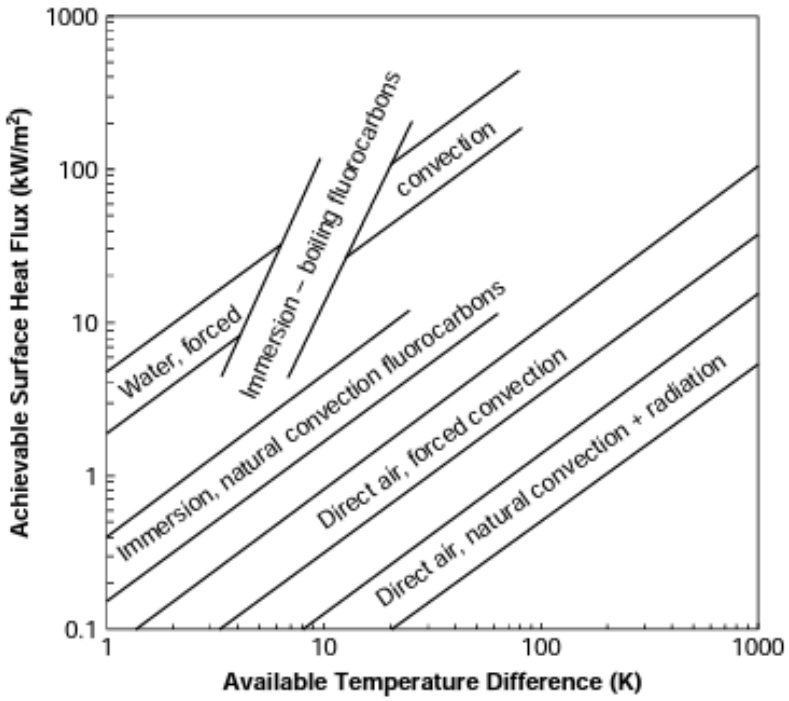

Figure 1.1: Variation of Achievable Surface Heat Flux with Available Temperature Difference for Various Heat Transfer Modes and Fluids [5]

Positive reports of energy savings are not limited to manufacturers advertising their products. In 2012, Intel completed a yearlong study and reported that servers submerged in GRC's mineral oil, GreenDEF, improved the Power Usage Effectiveness (PUE) rating from 1.6 to approximately 1.03 [9]. PUE is a measure of energy efficiency in which the total power used by the CPU is divided by the power supplied to the system; the optimal value is one. In 2014, reports indicated that Intel has continued to work on implementing liquid immersion cooling with 3M and Iceotope [10]. Other organizations,

such as Facebook [11] and the Mayo Clinic [12], have also explored liquid immersion cooling in recent years.

1.2 Numerical Modeling of Multiphase Heat Transfer

With recent interest in immersion and two-phase cooling using dielectric fluids, the primary focus of this study has been using commercially available computational fluid dynamics (CFD) programs, in particular ANSYS Fluent, to model pool and flow boiling heat transfer.

Fincher [13] laid the foundation for this work by using ANSYS Fluent built-in boiling functions to demonstrate strong agreement between numerical simulations and experimental data for several pool and flow boiling models involving the dielectric fluid Novec 649. This study continued to use ANSYS Fluent and focused on multiphase heat transfer; however, user defined functions (UDFs) based on experimental data were used in place of several built-in functions not only to allow better correlation between experiments and simulations but also to explore and present methods of setting key boiling parameters for future modeling.

For the work that follows, ANSYS Icepak was used to create the model, define geometric features and generate the mesh while ANSYS Fluent was used to set boiling parameters, define fluid properties and perform the iterative calculations. In continuation of Fincher's work, the boiling model in ANSYS Fluent remains the multiphase, Eulerian model known as the Rensselaer Polytechnic Institute (RPI) boiling model. Within this model, four empirically-based parameters determine the boiling physics; these are the nucleation site density, bubble departure diameter, bubble departure frequency and the area of influence.

The boiling functions in ANSYS Fluent were originally developed for water-based simulations. Implementations of the RPI boiling model in other CFD programs have successfully modeled boiling in nuclear applications [14, 15] and novel geometries [16]. By modifying certain boiling parameters, specifically the bubble departure diameter and nucleation site density, refrigerants, such as R-134 [17] and HFE-301 [18], and dielectric fluids, such as Novec 649 [13], have also been simulated.

1.3 Motivating Factors for User-Defined Functions (UDFs)

Typically, ANSYS Fluent offers two or three built-in functions per boiling property. Research using commercially available CFD programs has often been limited to these built-in functions; however, the work that follows utilizes user-defined functions (UDFs) in conjunction with experimental data to replace several built-in functions, in particular nucleation site density and bubble departure diameter.

As the use of liquid immersion and two-phase cooling increases, so too does the need to have numerical simulations that are less dependent on built-in functions and are more flexible, allowing simulations to better represent the desired system. The work that follows stems from the desire not only to illuminate how different boiling properties interact within ANSYS Fluent but also to provide more adequate correlations for boiling properties that incorporate experimental data.

This study begins by replicating Fincher's [13] pool boiling simulations of a single die, mounted on a printed circuit board, in a 15°C subcooled pool of Novec 649 using strictly the built-in boiling functions for bubble departure diameter and nucleation site density. This resulted in the generation of boiling curves for four cases that were compared to experimental data. Next, a parametric study was performed on two boiling

parameters—nucleation site density and bubble departure diameter—by implementing several user-defined functions (UDF) in place of the default boiling functions. When possible, previous experimental data for bubble departure diameter from Sridhar, et al. [19] was incorporated in the UDF. The resulting boiling curves were compared to experimental data. Additional equation forms for nucleation site density were explored, such as a piecewise nonlinear definition. The pool boiling simulations conclude with variations of the degree of subcooling and the turbulence model.

Flow boiling scenarios were also simulated using a numerical model based on an experimental cartridge module design. An initial baseline was established by setting all the boiling parameters to the default functions and comparing with experimental data as well as numerical results from Fincher [13]. The functions for nucleation site density and bubble departure diameter that resulted in the best agreement in pool boiling simulations were then incorporated into the flow boiling scenarios.

Chapter 2

LITERATURE REVIEW

This chapter begins by presenting the multiphase conservation equations in their general forms. Next, the Rensselaer Polytechnic Institute (RPI) boiling model developed by Kurul and Podowski is detailed along with how it is implemented in ANSYS Fluent 14.0. After discussing the built-in boiling functions included in ANSYS Fluent, alternative functions for nucleation site density and bubble departure diameter are presented.

Next, successful boiling simulations using the RPI boiling model, or one of its derivatives, in commercially available CFD programs are reviewed. The boiling simulations to be reviewed begin with water-based models and progress to dielectric fluids, in particular Novec 649. Lastly, numerical simulations involving both boiling and user-defined functions are presented.

2.1 Multiphase Conservation Equations

In ANSYS Fluent, the RPI model is one of the available multiphase, Eulerian models. All of the multiphase models are governed by the following conservation equations for continuity, momentum and energy [20]. For conservation of mass, or continuity, of phase q,

$$\frac{\partial}{\partial t}\left(v_{f,q}\rho_q\right) + \nabla \cdot \left(v_{f,q}\rho_q\vec{v}_q\right) = \sum_{p=1}^{n}\left(\dot{m}_{pq} - \dot{m}_{qp}\right) + S_q \tag{2.1}$$

where the subscripts p and q denote individual phases, v_f is the volume fraction, ρ is the density, $\vec{v}$ is the velocity vector and $\dot{m}_{pq}$ is the mass transfer from phase p to phase q and vice versa for $\dot{m}_{qp}$. S_q is a source term for mass and by default is zero. For conservation of momentum of phase q,

$$\frac{\partial}{\partial t}(v_f \rho \vec{v})_q + \nabla \cdot (v_f \rho \vec{v} \cdot \vec{v})_q = -v_{f,q} \nabla p + \nabla \cdot \bar{\tau}_q + v_{f,q} \rho_q \vec{g} + \sum_{p=1}^{n} (\vec{R}_{pq} + \dot{m}_{pq} \vec{v}_{pq} - \dot{m}_{qp} \vec{v}_{qp}) + (\vec{F}_q + \vec{F}_{lift,q} + \vec{F}_{wl,q} + \vec{F}_{vm,q} + \vec{F}_{td,q}) \tag{2.2}$$

where $\bar{\tau}_q$ is the stress-strain tensor, $\vec{g}$ is the gravitational acceleration, $\vec{R}_{pq}$ is an interaction force between phase p and q, $\vec{F}_q$ is a body force, $\vec{F}_{lift,q}$ is a lift force, $\vec{F}_{wl,q}$ is a wall lubrication force, $\vec{F}_{vm,q}$ is a virtual mass force, and $\vec{F}_{td,q}$ is a turbulent dispersion force. Depending on the boundary conditions and flow regime, several of the external forces may not be included during the iterative calculations. To ensure conservation of momentum is properly closed, the interaction force, $\vec{R}_{pq}$, which depends on friction, pressure and cohesion among others, is constrained with the following conditions:

$$\vec{R}_{pq} = -\vec{R}_{qp} \text{ and } \vec{R}_{qq} = 0 \tag{2.3}$$

For conservation of energy of phase q,

$$\frac{\partial}{\partial t}(v_{f,q} \rho_q h_q) + \nabla \cdot (v_{f,q} \rho_q \vec{u}_q h_q) = v_{f,q} \frac{\partial p_q}{\partial t} + \bar{\tau}_q : \nabla \vec{u}_q - \nabla \cdot \vec{q}_q + S_q + \sum_{p=1}^{n} (Q_{pq} + \dot{m}_{pq} h_{pq} - \dot{m}_{qp} h_{qp}) \tag{2.4}$$

where h_q is the specific enthalpy of phase q, $\vec{q}_q$ is the heat flux, S_q is a source term for enthalpy (chemical reaction, radiation, etc), Q_{pq} is the intensity of heat exchange between

phases and h_{pq} is the interphase enthalpy. To ensure conservation of energy is properly closed, the interphase heat exchange, Q_{pq}, is constrained with the following conditions:

$$Q_{pq} = -Q_{qp} \text{ and } Q_{qq} = 0 \tag{2.5}$$

2.2 Rensselaer Polytechnic Institute (RPI) Boiling Model

The RPI boiling model proposed by Kurul and Podowski will be detailed in this section as it is implemented in ANSYS Fluent according to the Fluent Theory Guide 14.0. Although originally developed for the nucleate boiling regime, others, such as Lavieville et al. [21] and Lifante et al. [22], have proposed modifications to extend the basic RPI model to more adequately simulate departure from nucleate boiling (DNB) and critical heat flux (CHF), respectively. Shown in the figure below is a typical pool boiling curve for heat-flux controlled boiling with the various boiling regimes indicated. In the figure, ONB denotes onset of nucleate boiling.

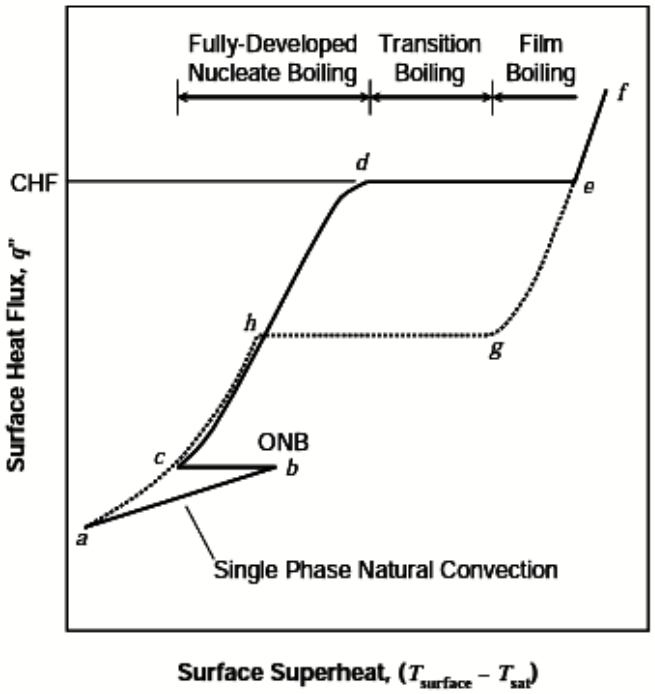

Figure 2.1: Typical Pool Boiling Curve for Heat Flux-Controlled Boiling [5]

The details and discussion that follow are for the basic RPI, nucleate wall boiling model. Boiling can occur despite the bulk fluid temperature being below the saturation temperature if the local wall temperature is sufficiently high; this is known as subcooled boiling. The energy that is transferred from the wall to the liquid goes several places, such as increasing the bulk fluid temperature or vaporizing liquid in contact with the wall surface. The separation of the wall heat flux into multiple components is the foundation of Kurul and Podowski's RPI boiling model. For the RPI model, the wall heat flux is separated into three quantities according to the following:

$$\dot{q}''_W = \dot{q}''_C + \dot{q}''_Q + \dot{q}''_E \tag{2.6}$$

where $\dot{q}''_W$ is the total wall heat flux and the subscripts C, Q and E denote convective, quenching and evaporative heat fluxes, respectively. For the convective heat flux, $\dot{q}''_C$,

$$\dot{q}''_C = h_C\left(T_w - T_{pool}\right)(1 - A_b) \tag{2.7}$$

where h_C is the single-phase heat transfer coefficient, T_w is the wall temperature and T_{pool} is the liquid temperature. The entire surface is not covered in nucleating bubbles. A distinction is made between the fractional area covered by bubbles, A_b, and the remainder of the wall that is covered by the fluid, $(1 - A_b)$. For the quenching heat flux, $\dot{q}''_Q$,

$$\dot{q}''_Q = \frac{2k_l}{\sqrt{\pi \alpha_l t}}\left(T_w - T_{pool}\right) \tag{2.8}$$

where the subscript l denotes the liquid phase, k_l is the thermal conductivity, t is the time period for bubble formation and departure and α_l is the thermal diffusivity. The

quenching heat flux is a measure of the energy transfer due to liquid filling the empty regions near the wall after a vapor bubble departs the surface. It is a cyclic averaged, time-dependent term, where each cycle is composed of bubble formation and departure. For the evaporative heat flux, $\dot{q}''_E$,

$$\dot{q}''_E = V_d N_w \rho_v h_{lv} f \tag{2.9}$$

where V_d is the volume of a bubble based on the bubble departure diameter, N_w is the active nucleation site density, ρ_v is the density of the vapor, h_{lv} is the latent heat of evaporation. The frequency of bubble departure, f, is also the inverse of the periodic time, t, given in Eq. (2.8). In order to close the above heat flux expressions, four parameters—area of influence, frequency of bubble departure, nucleate site density and bubble departure diameter—need to be further specified. Each of these parameters has at least one built-in function in Fluent along with the option of supplying a user-defined function. For the first parameter, the area of influence, A_b,

$$A_b = K \frac{N_w \pi (D_w)^2}{4} \tag{2.10}$$

where N_w is the nucleation site density and D_w is the bubble departure diameter. As will be discussed shortly, the nucleation site density is based on unbounded empirical relationships; therefore, to prevent numerical instabilities, the above expression is limited using a floor as follows:

$$A_b = \min\left(1, K \frac{N_w \pi (D_w)^2}{4}\right) \tag{2.11}$$

In both of the preceding expressions, K is an empirical constant that is often set to 4; however, the value can vary from 1.8 to 5. The default implementation of the area of influence parameter in Fluent uses another empirical correlation for K based on work by Del Valle and Kenning as follows [23]:

$$K = 4.8\exp\left(-\frac{Ja_{sub}}{80}\right) \tag{2.12}$$

where Ja_{sub} is the Jacob number for subcooled conditions and is defined by the following expression in which $\Delta T_{sub} = T_{sat} - T_{pool}$:

$$Ja_{sub} = \frac{\rho_l C_{pl} \Delta T_{sub}}{\rho_v h_{lv}} \tag{2.13}$$

For the second parameter, the frequency of bubble departure, f,

$$f = \frac{1}{t} = \sqrt{\frac{4g(\rho_l - \rho_v)}{3\rho_l D_w}} \tag{2.14}$$

where each of the terms has been defined previously. This is the default implementation of the bubble departure frequency in Fluent and is based on work by Cole [24]. For the third parameter, the active nucleation site density, N_w, is given by Eq. (2.15).

$$N_w = C^n (T_w - T_{sat})^n \tag{2.15}$$

Eq. (2.15) is the general expression for the active nucleation site density based on wall superheat, i.e. the temperature rise of the wall compared to the saturation temperature of the pool. C and n are empirical constants based on work by Lemmert and Chawla [25]. For the default implementation of nucleation site density in Fluent, the previous expression is used with $C = 210$ and $n = 1.805$. The resulting nucleation site density

from the above expression will have units of m^{-2} when the temperatures are in K or °C. For the fourth parameter, the bubble departure diameter, D_w is given by Eq. (2.16).

$$D_w = \min\left[0.0014\text{m}, (0.0006\text{m})e^{\left(-\frac{T_{sat}-T_{pool}}{45.0\text{K}}\right)}\right] \tag{2.16}$$

The above expression is the default implementation of the bubble departure diameter in Fluent and is based on an empirical correlation by Tolubinski and Kostanchuk [26]. The resulting bubble departure diameter from the above expression has units of meters when the temperature difference is in K or °C. The growth and departure phase of a vapor bubble is shown in Figure 2.2 along with several boiling parameters and the three heat flux components of the RPI boiling model.

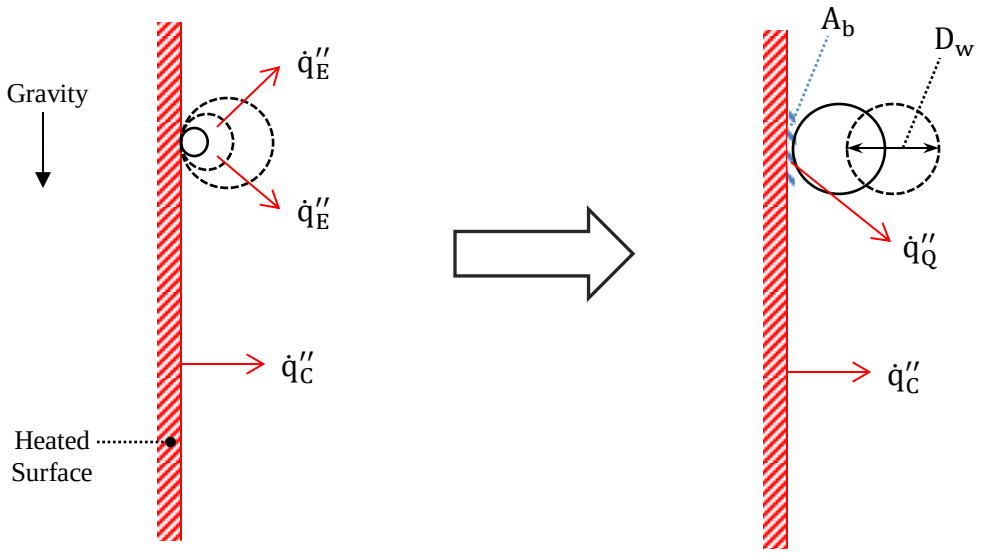

(a) Growth (b) Departure

Figure 2.2: One Cycle of (a) Bubble Growth and (b) Bubble Departure with the Three Heat Flux Components of the RPI Boiling Model

This concludes the introduction to the basic RPI boiling model in Fluent along with the closure relationships for the four default boiling parameters. The next section

will further explore the empirical relationships and experimental data from which the default boiling parameters in Fluent were derived. Particular emphasis is placed on the bubble departure diameter and nucleation site density.

2.3 Foundation of Boiling Functions in ANSYS Fluent

Because the bulk of this study involves using UDFs in place of Fluent's default bubble departure diameter and nucleation site density functions, this section will review the experimental setup and data that became the foundation of the Fluent functions. First, the work done by Tolubinsky and Kostanchuk on bubble departure diameter is presented followed by the work of Lemmert and Chawla on nucleation site density.

2.3.1 Bubble Departure Diameter

Tolubinsky and Kostanchuk used subcooled water boiling in a closed loop to experimentally determine vapor bubble dimensions, the generation frequency and the cycle averaged growth rate. Within the loop was a heated, stainless steel plate with dimensions of 55 x 2.5 x 0.25mm. Data was acquired primarily through high-speed photography with 2.5 times magnification (up to 20 times post-development) and 10,000 pictures per second [26].

The experiments performed by Tolubinsky and Kostanchuk included various pressures from 1 to 10 bar, degree of subcooling from 5 to 60^{o}C and heat fluxes from 0.05 to 1.0 MW/m^2. The top portion of Figure 2.3 is the maximum bubble departure diameter, d_{max}, and the frequency, f, as functions of the degree of subcooling. The bottom portion is the product of d_{max} and f also as a function of degree of subcooling. The arithmetical mean of the maximum horizontal or vertical dimension was used to

estimate the maximum diameter of the vapor bubbles for a given set of parameters.

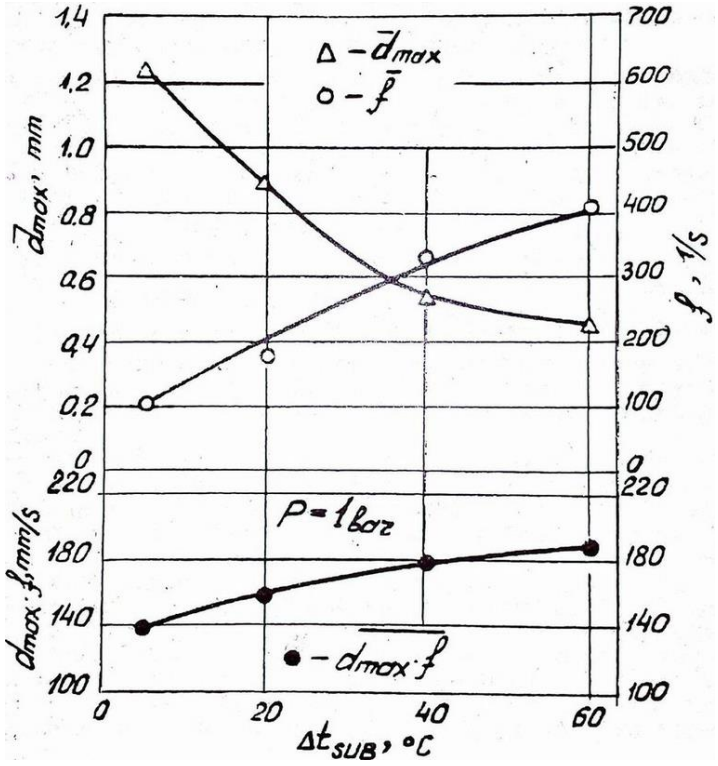

Figure 2.3: Dependence of Diameter $\mathbf{d_{max}}$, Generation Frequency $\boldsymbol{f}$, and Cycle Average Vapor Bubbles Growth Rate $\mathbf{d_{max}} \cdot \boldsymbol{f}$ at Pressure $\mathbf{P = 1}$ bar upon Subcooling [26]

The experimental data presented in Figure 2.3 significantly influenced the default bubble departure diameter closure relation in ANSYS Fluent given by Eq. (2.16). While the results found by Tolubinsky and Kostanchuk and incorporated into the RPI boiling model have been adequate for some numerical simulations, the limitations stemming from their working fluid and apparatus leave room for improving the bubble departure diameter correlation for fluids beyond water and other geometries.

2.3.2 Nucleation Site Density

Lemmert and Chawla also used a closed loop to experimentally determine surface boiling heat transfer characteristics for two geometries with R-11 as the working fluid. In

addition to boiling heat transfer coefficient data, Lemmert and Chawla presented the plot shown in Figure 2.4 for active nucleation site density as a function of wall superheat for both cylindrical and flat plate geometries.

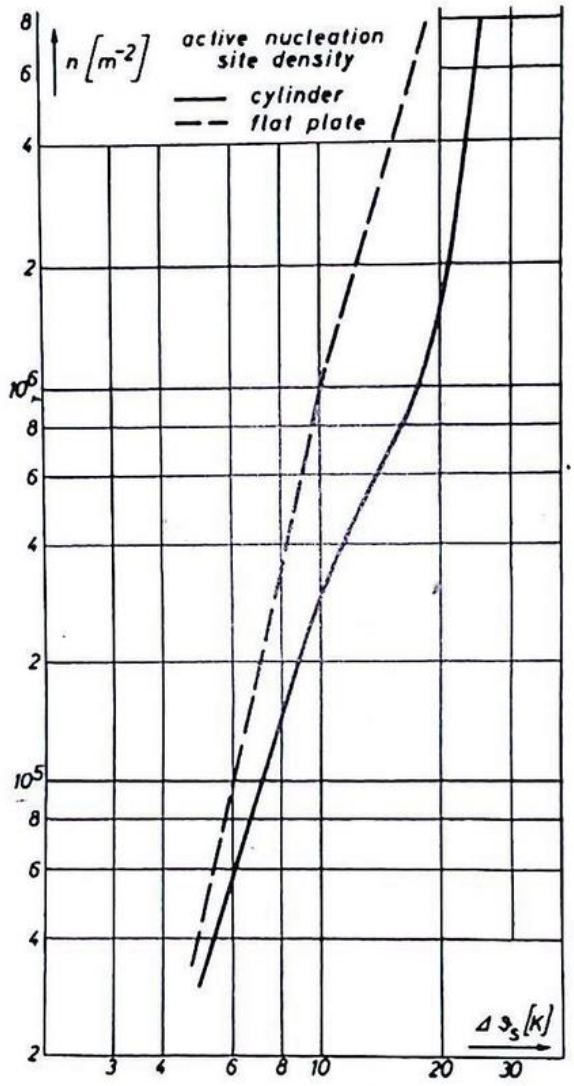

Figure 2.4: Active Nucleation Site Density $\boldsymbol{n}$ as a Function of Wall Superheat $\Delta\boldsymbol{\vartheta_s}$ [25]

The first geometry was a copper tube with a maximum outer diameter of 25.4 mm and length of 112 mm; the second geometry was a copper, flat plate with dimensions of 180 x 85 x 25 mm [25]. In both cases, the entire surface area was heated. Temperature data was acquired using thermocouples embedded in the test pieces. The work by

Lemmert and Chawla heavily influenced the default nucleation site density function in ANSYS Fluent as the closure relation given by Eq. (2.15) in the previous section resembles the form $N_a = [n(T_{sup})]^m$, where N_a is the number of active nucleation sites, T_{sup} is the wall superheat and n and m are empirical coefficients. Končar et al. have shown that setting m to 185 rather than the default 210 results in better agreement for some cases, particularly low pressure situations [27].

The RPI boiling model in ANSYS Fluent with default nucleation site density and default bubble departure diameter functions has resulted in adequate numerical simulations; these will be reviewed in the next section. As with bubble departure diameter, there is room for improving the nucleation site density correlation by using UDFs to more precisely tailor the fluid or geometric properties to different situations.

2.4 Numerical Simulations of Multiphase Flow using the RPI Boiling Model

In this section, numerical simulations using the RPI boiling model by Kurul and Podowski will be presented. The first segment will detail simulations in which the basic RPI model is used with default boiling parameters; these will typically have water as the working fluid. The next set of simulations to be reviewed will include dielectric fluids and other refrigerants. To adapt the RPI boiling model for use with other fluids, the nucleation site density and bubble departure diameter functions were modified. Alternative built-in boiling parameters that yielded good simulation results when compared to experimental data will also be discussed.

2.4.1 Simulations involving Water

Many of the boiling parameters used in the RPI boiling model are based on empirical results in which water was the working fluid. Therefore, simulations of boiling

water should result in better correlation with experimental data relative to simulations where water is not the working fluid. This section reviews the basic multiphase model proposed by Kurul and Podowski in such situations.

In 2012, In et al. [14] performed CFD simulations on the subcooled flow boiling of water in fuel bundles for a Pressurized Water Reactor (PWR) and Boiling Water Reactor (BWR) using ANSYS CFX 10.0. Among their objectives was to simulate the void distribution in a single subchannel of a fuel rod assembly and compare with computed tomography (CT) images along with measured, benchmark data. Figure 2.5 shows the test assembly and void fraction results.

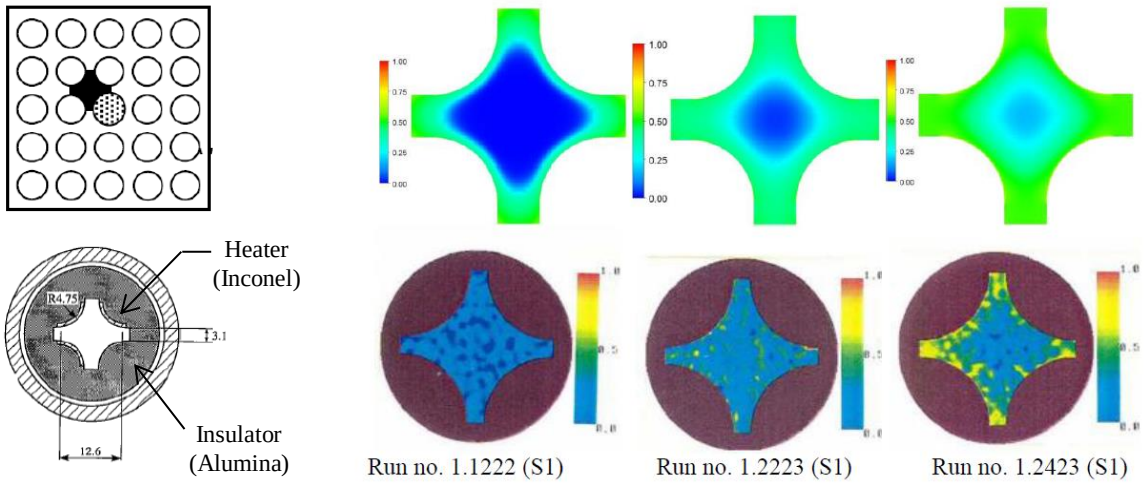

Figure 2.5: (a) Cross Sectional View of the Subchannel Test Assembly; (b) Void Fraction Contour in the Subchannel: CFD (upper), CT (lower) [14]

In et al. [14] used symmetry and generated a hexahedral mesh with 4.72 million nodes. Their boundary conditions consisted of uniform flow and constant temperature at the inlet, constant pressure at the outlet and uniform heat flux and no slip on the wall surfaces. Simulation convergence was determined when the momentum and volume fraction residuals fell below 10^{-6} and energy and turbulence conservation fell below 10^{-4}.

In Figure 2.5, the set of images on the left correspond to the fuel bundle assembly and a cross section view of the symmetry used in the CFD simulations. In the set of images on the right, the void fraction simulation results are compared with the CT scan results. According to In et al. [14], the void fraction contours from CFX 10.0 agree well with the CT scans as less vapor is seen in the core region while higher vapor fractions occur in the gap and near-wall region. One source of discrepancy is the high void simulation, Run 1.2423 (S1), in the figure above; vapor accumulates in the gap region between rods according to the CT scan while this trend is not reproducible by the CFD simulations. For the PWR cases, experimental data and simulation results agreed within 10% for void fraction at inlet subcooling that was 30^{o}C or less while CFD results tended to over-predict void fraction as the subcooling increased. For the BWR cases, simulation results agreed within 1% or 10% of measured data for low and high quality conditions at the exit, respectively [14].

In 2014, Wang et al. [15] used ANSYS CFX 12.0 to simulate the multiphase heat transfer between a nuclear reactor core on the primary side and the secondary side tube bundles of a steam generator (SG). The RPI boiling model of Kurul and Podowski with default boiling parameters was used not only to solve the subcooled flow boiling around the SG tube bundles but also to determine the effect that a tube support plate (TSP) and various inlet subcooling conditions would have on the SG. Wang et al. [15] used a nonconformal, hexahedral mesh; the grid was evaluated for independence by increasing the number of nodes from 1.12 million to 1.67 million. The resulting outlet void fraction and temperature changed by 0.81% and 0.1%, respectively. Before simulating the TSP, Wang et al. [15] validated their model against experimental results for void fraction,

average outlet temperature and wall temperature; the good agreement between experimental and simulation results can be seen in Figure 2.6.

Once validated, the TSP was introduced along with various degrees of inlet subcooling. According to Wang et al. [15], the vapor fractions and velocity streamlines correlated well with the expected results. Of note from the simulation results was introducing the TSP caused a new region where the void fraction became the highest, which potentially leads to poor heat transfer and CHF. Also noted was the effect of inlet subcooling—decreasing the inlet subcooling led to an increase in liquid and vapor velocity as well as significant increases in vapor fraction.

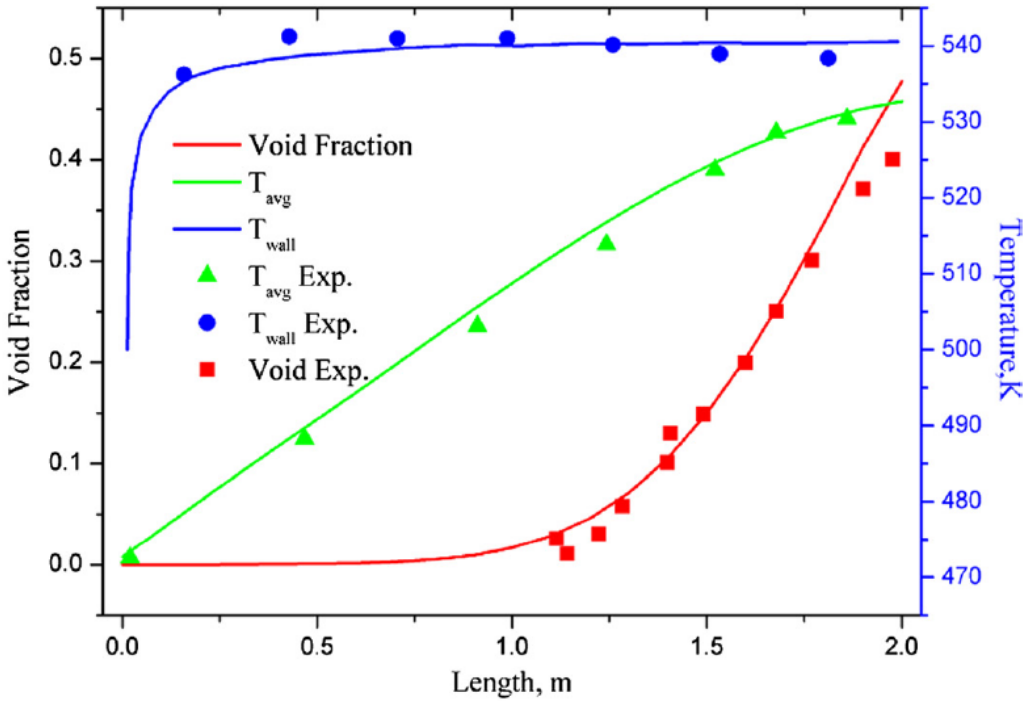

Figure 2.6: Benchmark Case with Comparison of Measured and Calculated Averaged Void Fraction, Averaged Temperature and Wall Temperature [15]

Also in 2014, Kim et al. [16] performed experimental and numerical simulations for an inclined channel with a downward-facing, heated upper wall. This geometry is

relevant in Advanced Light Water Reactors (ALWRs) as a safety feature should the core melt or the reactor pressure vessel fail. The boiling physics of a heated surface vary drastically depending on the orientation; for example, downward-facing surfaces or those less than 15^o to the horizontal cause vapor stratification on the heated surface resulting in diminished CHF [16].

Initially, Kim et al. [16] performed an experiment using high-speed video and thermocouples to capture bubble behavior and wall temperature, respectively, for a 0.1 x 0.1 x 1.2m channel, inclined 10^o from the horizontal. They observed that bubbles would grow larger for the downward-facing channel compared to the vertical orientation. In addition, once detached from the surface, the bubbles would slide along the wall and coalesce with smaller, downstream bubbles until slugs eventually formed.

Kim et al. [16] recreated their experimental geometry in ANSYS CFX 12.1 and used the RPI boiling model with default parameters; however, this resulted in poor agreement with experimental data as the RPI model over-predicted the wall superheat. Three of the boiling parameters—bubble departure diameter, nucleation site density and bubble departure frequency—were modified. For the bubble departure diameter, Kim et al. [16] used their experimental observations and set it to a constant value of 9.5 mm. For the nucleation site density, Kim et al. [16] modified the default Lemmert-Chawla correlation by applying a correction factor to account for the over-prediction of the RPI model; the modified form is given below.

$$N_w = 0.03[185(T_w - T_{sat})]^{1.805} \tag{2.17}$$

Lastly, for the bubble departure frequency, Kim et al. [16] proposed a “liquid film

evaporation frequency" given by Eq. (2.18) and summed it with the default bubble departure frequency given by Eq. (2.14).

$$f_{sb} = \frac{q''_{e,LF}}{N_w \left(\frac{\pi}{6} D_w^3\right) \rho_v h_{lv}} \tag{2.18}$$

where, the subscripts *sb*, *e*, and *LF* denote slug bubble, evaporation and liquid film, respectively, N_a is the active nucleation site density, D_b is the bubble departure diameter, ρ_g is the vapor density and h_{fg} is the latent heat of evaporation. Figure 2.7 compares both the unmodified and modified RPI models with experimental data.

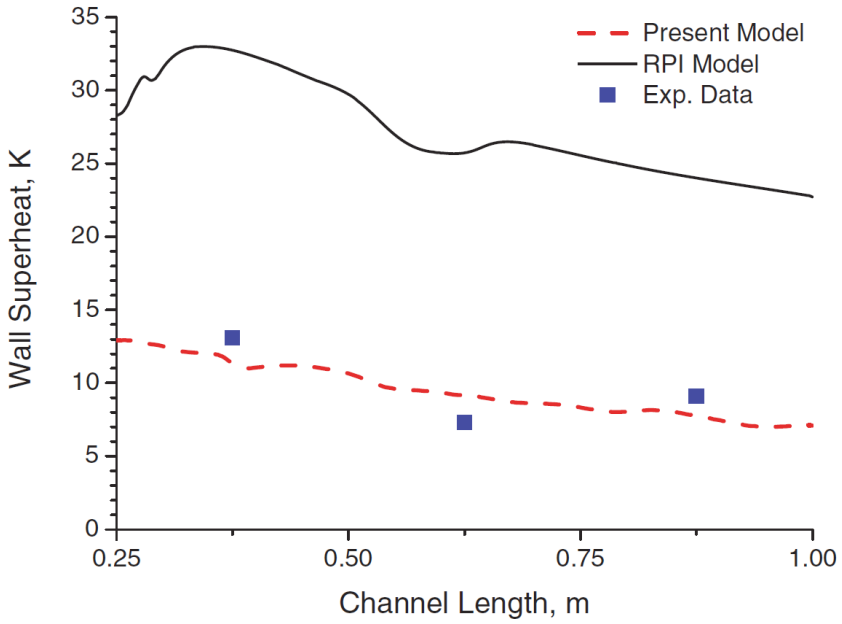

Figure 2.7: Wall Superheat along the Channel Length as found by a Modified RPI Model, the Default RPI Boiling Model and Experimental Data by Kim et al. [16]

From Figure 2.7, it can be seen that the RPI boiling model proposed by Kurul and Podowski can result in poor agreement even in simulations that use water as the working fluid, especially in models with low pressure or non-vertical, heated surfaces. However, as shown by Kim et al. [16], tailoring the boiling parameters to specific cases can

improve the simulation results. This concludes the review of water-based simulations using the RPI boiling model. The next section discusses alternative, built-in functions supplied by ANSYS Fluent 14.0 that were not mentioned in Section 2.2, followed by a review of simulations where water was not the working fluid.

2.4.2 Alternative Boiling Functions

The basic RPI boiling model proposed by Kurul and Podowski as implemented in numerous CFD programs has been discussed in Section 2.2 along with the default boiling parameters. In this section, other readily available functions in ANSYS Fluent 14.0 for the various boiling parameters are discussed. It should be noted that a UDF may be supplied for any of these parameters; however, this section focuses on built-in options and UDFs will be explored in a later section.

2.4.2.1 Frequency of Bubble Departure and Area of Influence

For the frequency of bubble departure, the only built-in model available is the Cole [24] formulation given by Eq. (2.14). For the area of influence, a constant value may be set in addition to the Del Valle-Kenning [23] formulation given by Eq. (2.11). The subsequent sections will present alternative nucleation site density and bubble departure diameter functions included in ANSYS Fluent 14.0

2.4.2.2 Nucleation Site Density

In addition to the Lemmert-Chawla formulation given by Eq. (2.15), the nucleation site density can be modeled using the following empirical relationship, proposed by Kocamustafaogullari and Ishii (K-I) [28]:

$$N_w = \frac{N_w^*}{(D_w)^2} \tag{2.19}$$

where N_w^* is a nondimensional grouping given by Eq. (2.20) below and D_w is the bubble departure diameter. ρ^* and r_c^* are nondimensional groupings for the fluid density and bubble radius, respectively, which are also defined below:

$$N_w^* = f(\rho^*)(r_c^*)^{-4.4} \tag{2.20}$$

$$\rho^* = \frac{\rho_l - \rho_v}{\rho_v} \tag{2.21}$$

$$r_c^* = \frac{2(r_c)}{D_w};\ r_c = \frac{2\sigma T_{sat}}{\rho_v h_{lv}(T_w - T_{sat})} \tag{2.22}$$

where, σ is the surface tension and $f(\rho^*)$ is a density function defined by the following:

$$f(\rho^*) = (2.157 \times 10^{-7})(\rho^*)^{-3.2}(1 + 0.0049\rho^*)^{4.13} \tag{2.23}$$

By including fluid properties, the K-I model for nucleation site density could result in better agreement for a wider range of situations compared to the default Lemmert-Chawla function.

2.4.2.3 Bubble Departure Diameter

Of all the boiling parameters, the bubble departure diameter has the most options built into Fluent, including the ability to set a constant value. Two alternative functions are available in addition to the default formulation by Tolubinsk and Kostanchuk given by Eq. (2.16). First, the bubble departure diameter can be modeled using the following expression based on work by Kocamustafaogullari and Ishii [29]:

$$D_w = 0.0012(\rho^*)^{0.9} \times (0.0208 \deg^{-1}) \emptyset \sqrt{\frac{\sigma}{g(\rho_l - \rho_v)}} \tag{2.24}$$

where D_w is in meters, ρ^* is the same nondimensional grouping given by Eq. (2.21) and $\emptyset$ is the contact angle in degrees. The second alternative, built-in function is based on relationships derived by Unal [30] and is given by the following:

$$D_w = 2.42 \times 10^{-5} (P)^{0.709} \left(\frac{a}{b\sqrt{\varphi}} \right) \tag{2.25}$$

where D_w is in millimeters, P is the flow pressure in Pascal (Pa), and a, b and φ are empirical expressions given by the following:

$$a = \frac{T_w - T_{sat}}{2\rho_v h_{lv}} \sqrt{\frac{\rho_s C_{ps} k_s}{\pi}} \tag{2.26}$$

$$b = \begin{cases} \dfrac{\Delta T_{sub}}{2\left(1 - \dfrac{\rho_v}{\rho_l}\right)} e^{\left(\frac{\Delta T_{sub}}{3} - 1\right)} & \Delta T_{sub} \leq 3 \\ \dfrac{\Delta T_{sub}}{2\left(1 - \dfrac{\rho_v}{\rho_l}\right)} & \Delta T_{sub} > 3 \end{cases} \tag{2.27}$$

$$\varphi = \max\left[\left(\frac{U_b}{U_0} \right)^{0.47}, 1 \right] \tag{2.28}$$

where ΔT_{sub} is the difference between the saturation and pool temperatures, the subscripts s, l, and v denote the solid, liquid and vapor phases, respectively, U_b is the near wall bulk velocity and U_0 is an empirical constant equal to 0.61 m/s.

This concludes the ANSYS Fluent 14.0 alternative built-in functions for the various boiling parameters. As will be seen in the next section, several of these functions,

in particular the K-I formulation for nucleation site density, have resulted in better agreement than their default counterparts. On the other hand, Fincher reported unsuccessful attempts to utilize the Unal expression for bubble departure diameter due to its highly empirical nature [13].

2.4.3 Simulations involving Other Fluids

This section reviews numerical simulations in which water was not the working fluid. There will be two subsections; in the first, simulations using the RPI Model by Kurul and Podowski with default boiling functions are reviewed while the second subsection includes simulations with alternative, built-in boiling parameters, such as those discussed in the previous section.

2.4.3.1 Other Fluids with Default Boiling Parameters

In 2008, Vyskocil and Macek [31] used two CFD programs—NEPTUNE_CFD and Fluent 6.1—to simulate subcooled boiling of R-12 in a vertical pipe. The boiling model by Kurul and Podowski was implemented in both CFD programs. Experimental data was available from previous studies by the French Alternative Energies and Atomic Energy Commission (CEA). The experimental and simulated geometry was a 19.2 mm diameter pipe, which was divided into three sections—an inlet adiabatic section (1 m), the heated section (3.5 m) and the outlet adiabatic section (0.5 m). A comparison of both CFD programs with experimental data for void fraction and bubble diameter is shown in Figure 2.8, where the x-axis is the distance from the pipe center. From Figure 2.8a, Fluent resulted in better agreement for the void fraction. However, Fluent over-predicted the bubble diameter compared to NEPTUNE_CFD. By modifying the turbulent dissipation

coefficient in Fluent's realizable k-ε turbulence model, Vyskocil and Macek were able to achieve better agreement.

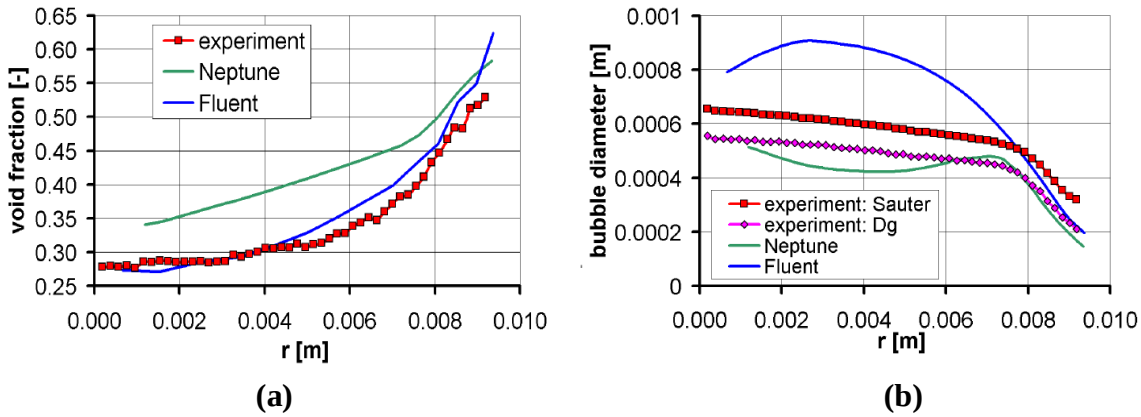

Figure 2.8: Case 4 – Experimental Results Compared with NEPTUNE_CFD and Fluent Simulations for (a) Void Fraction and (b) Bubble Diameter [31]

The vapor velocity and liquid temperatures were also plotted and found to be comparable between the two CFD programs and showed reasonable agreement with experimental data.

In 2009, Chen et al. [32] used the RPI boiling model by Kurul and Podowski with default boiling parameters implemented in ANSYS CFX-10 to simulate subcooled flow boiling of R-113 in a vertical, concentric annulus. Experimental data was available for model validation from a previous study by Arizona State University. The primary objective was to determine the effect of temperature-dependent properties and variable saturation temperature. Over a 40^{o}C subcooling range, the density, thermal conductivity, viscosity and specific heat of R-113 vary by +6.7%, +13.5%, +57.1% and -4.7%, respectively [32]. The experimental and simulated geometry consisted of a Pyrex outer tube and a stainless steel inner tube, which had an unheated, inlet section (0.91m) and a

heated section (2.75m). The void fraction simulation results are compared with experimental data in Figure 2.9, where the x-axis is a nondimensional radius.

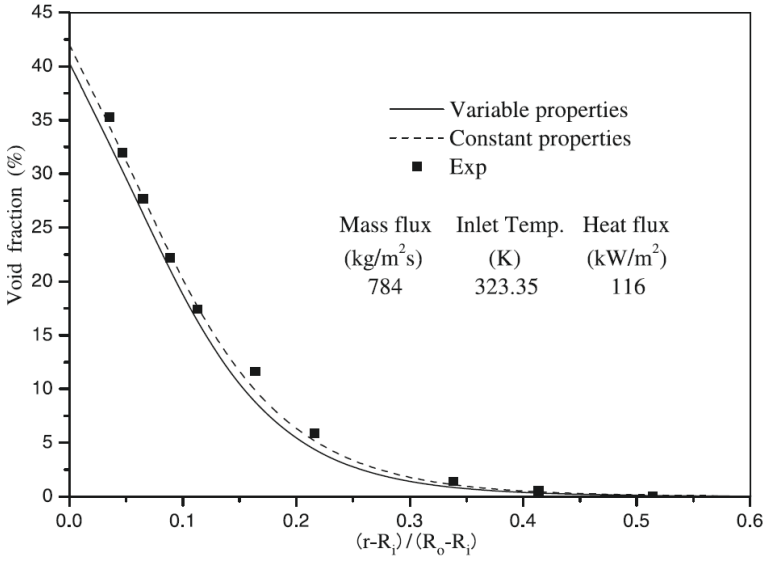

(a)

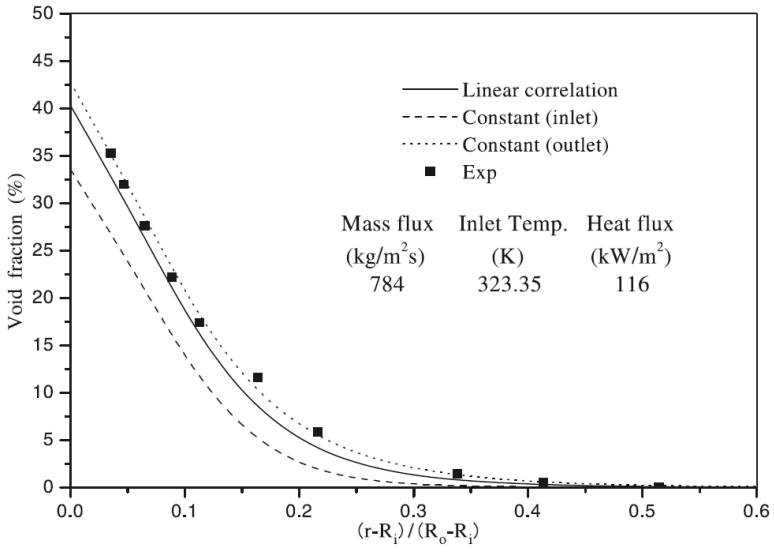

(b)

Figure 2.9: Effect of (a) Variable Liquid Properties of R-113 and (b) Variable Saturation Temperature on the Void Fraction, Measured 0.5m Downstream from the Entrance to the Heated Segment [32]

Figure 2.9a shows the effect of variable fluid properties (density, thermal conductivity, viscosity and specific heat) while Figure 2.9b shows the effect of variable saturation temperature. Three saturation temperatures were simulated—a constant value based on inlet pressure, a constant value based on outlet pressure and a linear function between the two. Varying the property values had a relatively negligible effect while using a linear correlation for the saturation temperature improved the agreement with experimental data.

In 2012, Končar and Matkovič [18] simulated subcooled flow boiling of HFE-301 in a rectangular, vertical channel using ANSYS CFX-12.1 to determine the effect of Reynolds number and heat flux on the velocity field and turbulence intensity distribution in the near wall region. This was part of a study for the Nuclear Reactor Integrated Simulation Project (NURISP) and experimental data for model verification was available from Texas A&M University. Figure 2.10 shows the numerical results compared with experimental data for the axial velocity as a function of channel width.

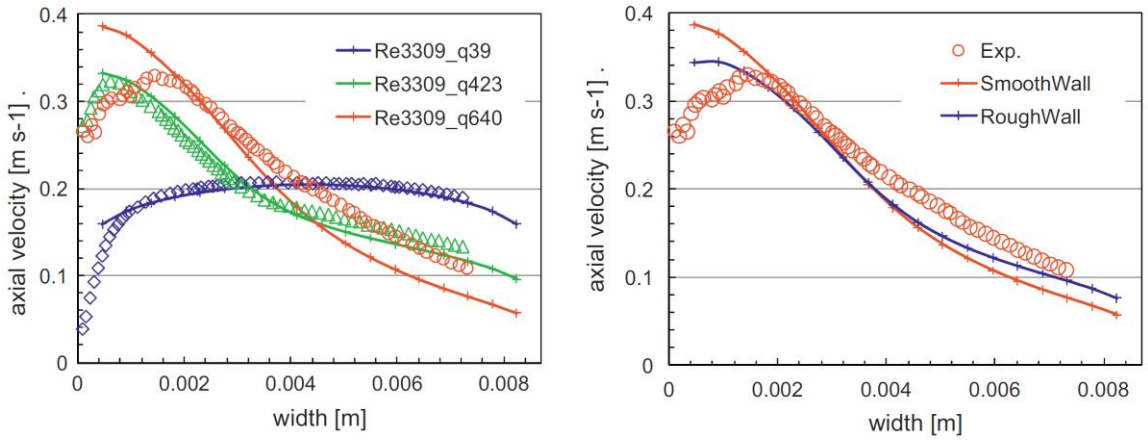

(a) **(b)**

Figure 2.10: Effect of (a) Heat Flux Variation and (b) Wall Roughness on the Axial Velocity for a Reynolds Number of 3,309; Note: Heat Flux in (b) is 64 kW/m^2 [18]

The experimental and simulated geometry consisted of a polycarbonate, rectangular channel 530 mm in length with a hydraulic diameter of 8.2mm. A heater was placed on one of the channel walls 320 mm from the inlet while measurements were taken 455 mm from the inlet. Numerical simulations used the RPI boiling model of Kurul and Podowski with default boiling parameters. The simulated variables were Reynolds number and heat flux, which varied from 3,309 to 16,549 and 39 to 64 kW/m^2, respectively. Končar and Matkovič noted that trends due to Reynolds number and heat flux variations were reasonably predicted; an example of the good agreement over a range of heat fluxes is shown in the previous figure on the left. However, at low Reynolds numbers, such as the one shown in the previous figure, axial velocity tended to be under-predicted at higher heat fluxes. To improve agreement, a wall roughness model using an equivalent roughness based on the bubble diameter was proposed and the improved agreement can be seen in Figure 2.10b.

This concludes the review of numerical simulations in which the working fluid was not water and the RPI model of Kurul and Podowski with default boiling parameters was used. Despite simulating more complex fluids, there has been success with the RPI boiling model, which typically can be improved further by modifying the boiling parameters or some other function, such as wall roughness or fluid properties, to suit specific scenarios. The next section continues reviewing non-water based simulations; however, the RPI boiling model is no longer restricted to default boiling parameters.

2.4.3.2 Other Fluids with Alternative, Built-in Boiling Parameters

In 2010, Prabhudharwadkar et al. [33] used ANSYS CFX-11 to simulate subcooled flow boiling of R-12 and R-113 with two primary objectives. The first was to

evaluate bubble departure frequency and nucleation site density functions against experimental data sets with measured bubble departure diameter. The second objective was to use the validated boiling functions and explore the near wall turbulent kinetic energy (TKE) and Reynolds stress for single phase and two-phase turbulent wall functions. It was determined that the default bubble departure frequency model by Cole, described by Eq. (2.14) resulted in good agreement for several cases; therefore, Prabhudharwadkar et al. focused on two nucleation site density functions—that of Lemmert-Chawla (L-C) and that of Kocamustaffaogullari and Ishii (K-I) as described by Eq. (2.15) and (2.19), respectively.

The first simulated geometry consisted of R-12 flowing through a 19.2mm diameter vertical pipe with three sections—an adiabatic inlet (1m), a heated section (3.5m) and an adiabatic outlet (0.5m). Simulation results for void fraction, interfacial area concentration and liquid temperature were validated against four experimental data sets for this geometry to determine which nucleation site density function resulted in better agreement. For void fraction, L-C under-predicted the experimental value while K-I resulted in good agreement for all cases, but demonstrated worse agreement as the pressure decreased. For the interfacial area concentration, K-I also resulted in better agreement for all cases. Lastly, for the radial liquid temperature profile and wall superheat, L-C over-predicted both while K-I predicted the temperature well, but under-predicted the wall superheat. Overall, the K-I model for nucleation site density resulted in better agreement for more situations and variables compared to the default L-C model.

To further validate the boiling parameters, Prabhudharwadkar et al. used the Cole model for bubble departure frequency and the K-I model for nucleation site density and

simulated a second geometry, which consisted of R-113 flowing through a vertical annulus with an inner and outer radius of 15.78 and 38.02 mm, respectively. Comparison of simulation results with six experimental data showed good agreement again.

With the bubble departure frequency and nucleation site density functions validated against two experimental data sets, Prabhudharwadkar et al. focused on their second objective—exploration of single and two-phase turbulent wall models. The built-in, single phase turbulent wall function resulted in fair agreement with experimental data for near wall TKE and Reynolds stress; however, by implementing an empirical set of two-phase log law coefficients into CFX-11, better agreement was found.

In 2014, Fincher [13] laid much of the foundation for the work done in this study by using ANSYS Fluent 14 to simulate pool and flow boiling of Novec 649 in multiple geometries. Before using Novec 649, Fincher validated the RPI boiling model with default boiling parameters by simulating pool boiling on the surface of a 0.15 x 0.75 x 0.001 m nickel plate that was vertically orientated in a 10°C subcooled pool of water. Good agreement was seen between simulation results for temperature rise and the Rohsenow correlation [34] given by Eq. (2.29).

$$\frac{\dot{q}}{\mu_l h_{lv}}\left[\frac{\sigma}{g(\rho_l-\rho_v)}\right]^{1/2}=\left(\frac{1}{C_{sf}}\right)^{1/r}(Pr_l)^{-s/r}\left[\frac{C_{pl}(T_w-T_{sat})}{h_{lv}}\right]^{1/r} \tag{2.29}$$

The second geometry consisted of a square-patterned, multi-chip module in which four 24 x 24 x 6 mm silicon die, mounted on a 150 x 150 x 1.4 mm printed circuit board (PCB), was submerged vertically in a 15°C subcooled pool of Novec 649. The numerical simulations were performed with a single die active—the top left. Simulation results were generated for three combinations of built-in boiling functions for nucleation site density

and bubble departure diameter. The worst and best agreement with experimental data are shown in Figure 2.11.

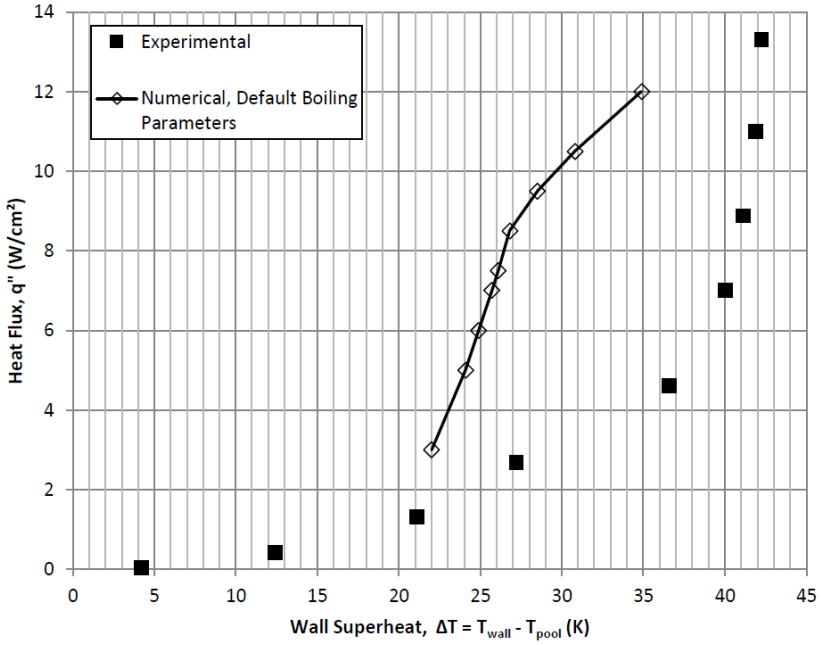

(a)

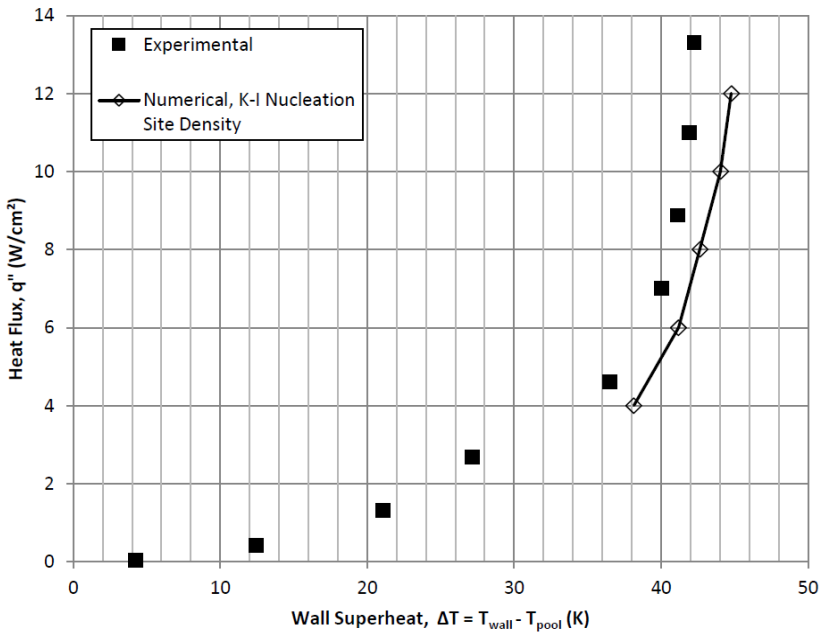

(b)

Figure 2.11: Comparison of Experimental Data to Numerical Simulations of the Single Heated Die for Novec 649, 15°C Subcool for (a) Case A and (b) Case C [13]

Case A (Figure 2.11a) used default functions for bubble departure diameter (T-K, given by Eq. 2.16) and nucleation site density (L-C, given by Eq. 2.15) while Case C (Figure 2.11b) used the default function for bubble departure diameter and the K-I model, given by Eq. (2.19), for nucleation site density. From Figure 2.11, Case A (top) had the worst agreement while Case C (bottom) had the best agreement with experimental data. Simulation results were also generated for Case B, which used the default nucleation site density function (L-C) with the K-I bubble departure diameter function; these results were reasonable but deviated further from experimental data as the heat flux increased. In addition to temperature, vapor fraction and velocity vectors were the most reasonable for Case C.

The third simulated geometry was the flow boiling of 15°C subcooled Novec 649 in a unique, modular liquid immersion cooled server in the form of a cartridge with dimensions of 300 x 150 x 38 mm as described in [13, 35]. An image of this geometry can be seen in the insert of Figure 2.12, where the green, light gray and dark gray objects are the PCB, silicon die and flow distributor, respectively.

Simulation results compared to experimental data are also shown in Figure 2.12. For this simulation, the RPI boiling model was used with all default boiling parameters, i.e. the Del Valle and Kenning model for fractional area of influence (Eq. 2.11), the Cole model for bubble departure frequency (Eq. 2.14), the Lemmert-Chawla model for nucleation site density (Eq. 2.15) and the Tolubinski-Kostanchuk model for bubble departure diameter (Eq. 2.16). The heat fluxes simulated varied from 4 to 12 W/cm^2 while the inlet flow rate varied from 800 to 1200 mL/min. In general, good agreement

between simulation results and experimental data was seen for the silicon die temperature as shown in Figure 2.12.

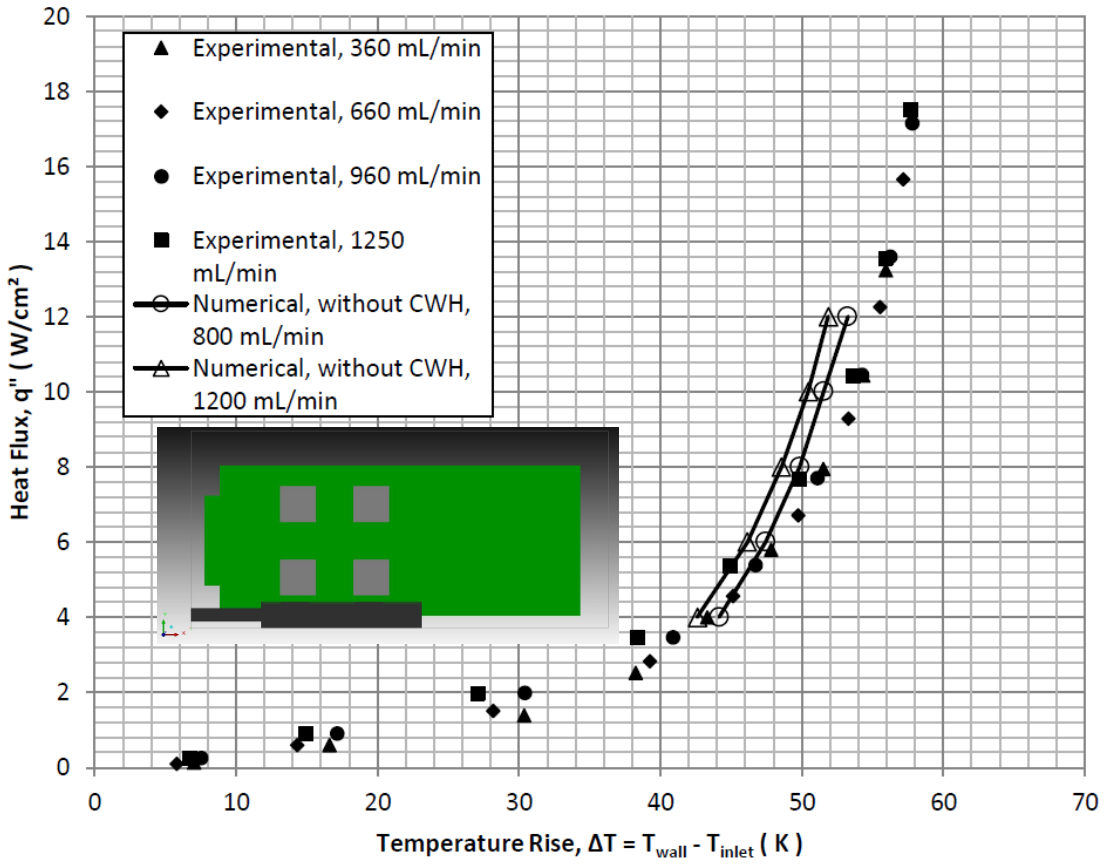

Figure 2.12: Insert: Simulation Model of the Liquid Immersion Cooled Server Design [35]; Plot: Cartridge Model with Chilled Water Header, 800 mL/min and 1200 mL/min, Novec 649, 15^{o}C Subcool [13]

However, for increased flow rate, the numerical model predicted a decrease in the maximum die temperature over the entire range of heat fluxes, but such a trend was not seen in the experimental data at higher heat fluxes. Fincher noted that the boiling model under-predicted the vapor fraction and the system was still dominated by convective heat transfer due to the increased flow velocity rather than boiling heat transfer [13].

This concludes the review of the RPI boiling model with various built-in boiling functions used in simulations where the working fluid was not water. The next section

begins the discussion of user-defined functions (UDFs) to modify the boiling parameters and how they are implemented in ANSYS Fluent 14.0.

2.5 Implementation of User-Defined Functions (UDFs) in ANSYS Fluent

In this section, a brief overview of UDFs will be given along with the data structure nomenclature and general UDF structure. The primary reason for using UDFs in this study is to explore nucleation site density and bubble departure diameter functions beyond those built into Fluent and to use experimental data for bubble departure diameter to achieve better agreement.

A Fluent UDF is a set of commands and calculations written in the C programming language that can be linked or "interpreted" into Fluent and the numerical model. Once "interpreted," the UDF can then be "hooked" or set to override existing built-in functions. Standard C commands are included in addition to pre-defined macros that allow access to field variables, material properties and cell geometry data [36].

Next, an overview of the data structure in Fluent will be discussed. Figure 2.13 is an example numerical model with the mesh outlined. Several of the data structure types and related nomenclature are marked.

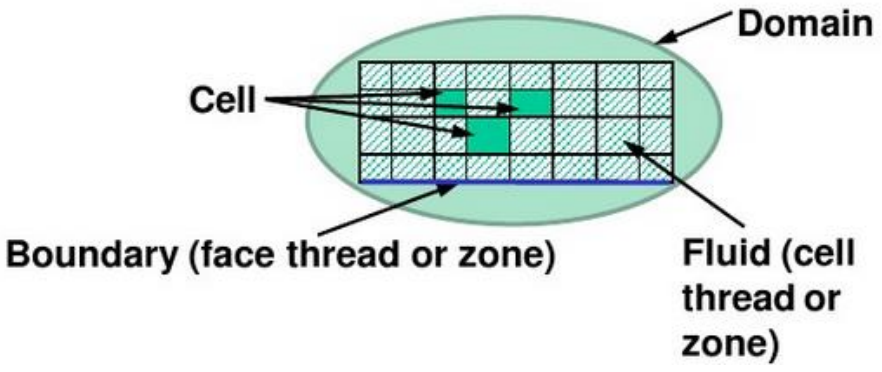

Figure 2.13: Numerical Domain with the Data Type Nomenclature Included [36]

The domain is the entire region over which the numerical solution takes place. For single phase simulations, there is only one domain structure; however, for multiphase models, there is a domain structure for each phase, the interaction between phases and the mixture [37]. Within the domain are two types of threads for cells and faces. Individual cells and faces are grouped and contained within a thread of the corresponding type.

Table 2.1 includes a further description of the mesh components and data types; the table is arranged in ascending order of relative size, i.e. the smallest element, a node, is the first item listed while the largest group of elements, the domain, is listed last.

Table 2.1: Mesh Components and their Corresponding Description [37]

node	a mesh point
node thread	a grouping of nodes
edge	a boundary of a face (3D)
face	a boundary of a cell (2D or 3D)
face thread	a grouping of faces
cell	a control volume into which a domain is broken up
cell center	the location where cell data is stored
cell thread	a grouping of cells
domain	a grouping of node, face and cell threads

Lastly, the general UDF structure will be discussed. Each UDF typically begins with the command — #include "udf.h" – that will allow access to a library of pre-defined macros, termed "DEFINE macros." There are hundreds of DEFINE macros organized into general purpose, model-specific, multiphase only and other categories. Within the multiphase subset of DEFINE macros are ways to manipulate the boiling property, cavitation rate, phase interaction, etc.

For this study, the DEFINE_BOILING_PROPERTY macro is used significantly as it will pass eight variables from Fluent into the UDF and allow custom nucleation site

density and bubble departure diameter functions to be used in place of the built-in functions. DEFINE macros, even the same one, can be chained together in the same UDF file to allow the replacement of multiple built-in functions at the same time, i.e. a custom calculation for nucleation site density can be run concurrently with a custom calculation for the bubble departure diameter.

This concludes the overview of user-defined functions in Fluent; a more detailed discussion not only on UDFs in general but also UDFs specific to this study can be found in Appendix C. The following section will review multiphase numerical simulations that used UDFs to extend the built-in capabilities.

2.6 Numerical Simulations involving Multiphase Flow and UDFs

In 2008, Narumanchi et al. [17] used ANSYS Fluent to simulate turbulent jet impingement with nucleate boiling for several fluids. Experimental data was available to validate the water and R-113 simulations; however, R-134a was not validated. The RPI boiling model by Kurul and Podowski was used with three of the four boiling parameters (nucleation site density, frequency of bubble departure and fractional area of influence) kept as the default functions. A UDF was used to calculate the bubble departure diameter based on the following empirical correlation:

$$D_w = 3f_1f_2\left[\frac{\rho_l}{2(\rho_l-\rho_v)g}\left(\frac{\rho_l C_{pl}(T_w-T_{sat})\alpha^{1/2}}{\rho_v h_{lv}}\right)^4\right]^{1/3} \tag{2.30}$$

where h_{lv} is the latent heat in J/kg, α is the thermal diffusivity in m^2/s, f_1 is a pressure correction multiplier and f_2 is another correction multiplier that accounts for the liquid

shear near the wall creating additional drag forces that reduce the bubble departure diameter. These correction factors are given by Eq. (2.31) and (2.32),

$$f_1 = 1 + 0.1503 \cdot [(P \times 10^{-5}) - 1.01352] \tag{2.31}$$

$$f_2 = \exp(-6.3512 \cdot |\vec{v}_l|) \tag{2.32}$$

where P is the pressure in Pascal and $\vec{v}_l$ is the velocity near the wall in m/s.

In the first set of simulations, Narumanchi et al. modeled 3^{o}C subcooled water impinging on a heated disk with a diameter of 10 mm; the inlet velocity was 2 m/s. The predicted wall superheat was within 20% of experimental data. Once validated against experiments using water as the working fluid, Narumanchi et al. modeled 18.5^{o}C subcooled R-113 impinging on a heated disk with a diameter of 5.6 mm. For this case, two inlet velocities were simulated: 0.41 and 11.36 m/s. When compared with experimental data, better agreement was seen as the predicted wall superheat was within 10% for both velocities. A third set of simulations involving insulated-gate bipolar transistors (IGBTs) with boiling jets was modeled using R-134a as the working fluid; however, the results were not discussed in detail as there was not experimental data to validate the simulation results.

Also in 2008, Vyskocil and Macek [31] simulated subcooled boiling of R-12 in a vertical pipe using NEPTUNE_CFD and Fluent 6.1. Their results and comparisons to experimental data have already been discussed in Section 2.4.3.1; however, those results were limited to default boiling functions and default turbulence settings. Vyskocil and Macek determined that the default turbulence model in Fluent under-predicted the turbulent dissipation, ε, in the core of the flow; this caused bubble coalescence to be

exaggerated, the break-up in the core region to be under-predicted and the bubble diameter to be over-predicted [31]. A UDF was used to modify the turbulence settings, in particular, a floor was placed on the turbulence dissipation, ε. The plots in Figure 2.14 compare experimental data for void fraction and bubble diameter with simulations using default turbulence models and the UDF modification. From Figure 2.14b, bubble diameter was significantly improved by applying a UDF to limit the turbulent dissipation values. Although the void fraction was improved in the core region, it was still over-predicted towards the pipe wall.

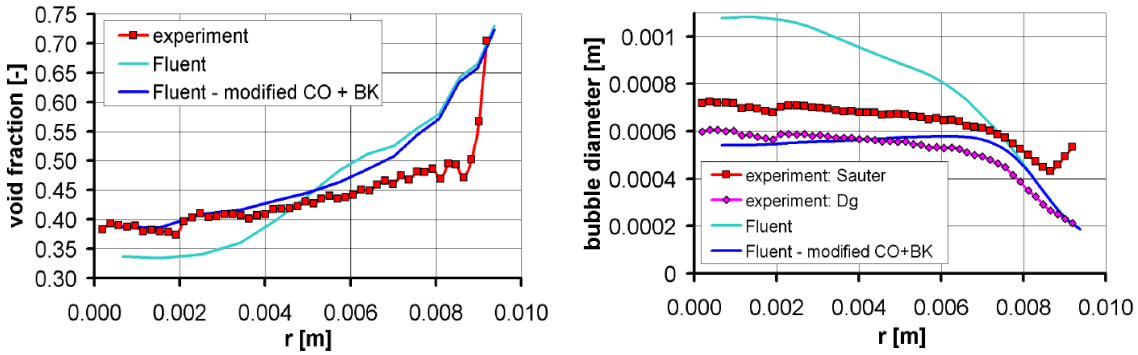

(a) **(b)**

Figure 2.14: Case 7 – Experimental Results Compared with NEPTUNE_CFD and Fluent Simulations for (a) Void Fraction and (b) Bubble Diameter [31]

Lastly, in 2014, Kim et al. [16] simulated an inclined channel with a downward-facing heated upper wall using ANSYS CFX 12.1. Their results and comparisons to experimental data have already been discussed in detail in Section 2.4.1 with the other water-based simulations. Initially, their results showed very poor agreement in part due to the nucleation site density being drastically over-predicted by the default Lemmert-Chawla (L-C) correlation. Figure 2.15 shows nucleation site density as a function of wall

superheat for multiple empirical correlations, including the default L-C model, compared with experimental data. In Figure 2.15, Eq. (15) refers to a modified form of the L-C nucleation site density function given by Eq. (2.33), where N_w is in m^{-2} when the wall and saturation temperatures are in °C or K. This modified L-C function was implemented into a UDF and improved the agreement with experimental data.

$$N_w = 0.03[185(T_w - T_{sat})]^{1.805} \tag{2.33}$$

Figure 2.15 highlights how the empirical nature of the built-in functions can result in significantly under predicted or over predicted values for nucleation site density, bubble departure diameter, etc.

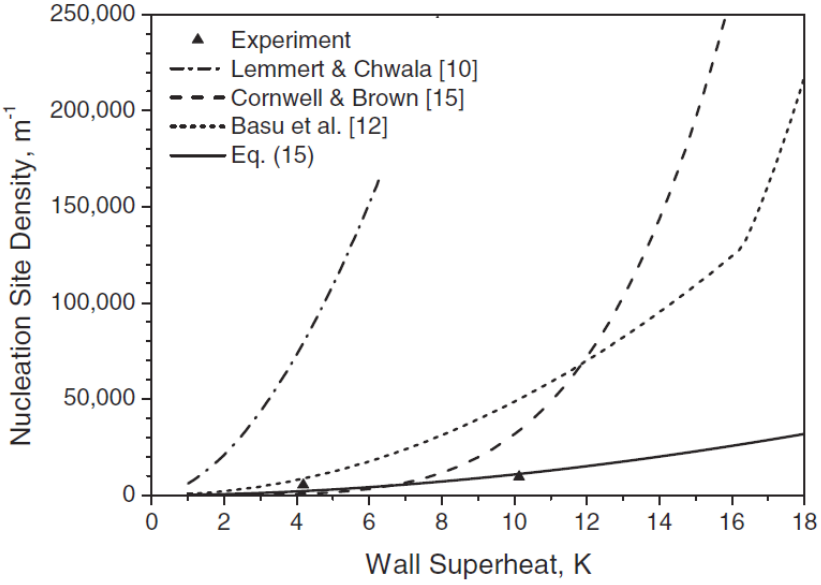

Figure 2.15: Modified Active Nucleation Site Density Function based on Experimental Observation; Eq. (15) in the figure legend refers to equation (15) of reference [16]

This concludes the review of simulations involving UDFs to modify various built-in functions, such as boiling parameters or turbulence models. While this study relies heavily on the RPI boiling model for the nucleate boiling regime, other multiphase

techniques exist and the next section will explore these alternatives with an emphasis on models for other boiling regimes, such as film boiling, and other scales of boiling, such as the dynamics of a single bubble.

2.7 Other Multiphase Numerical Models and Methods

The nucleate boiling model developed by Kurul and Podowski is not the only multiphase model available in CFD packages and other individuals have used alternative models based on the boiling regime or geometry scale of interest. For example, ANSYS Fluent 14.0 provides a Volume-of-Fluid (VOF) model that is recommended over the RPI boiling model when fluids are immiscible [20]. The numerical methods for large scale boiling simulations are presented first followed by those used when modeling the dynamics associated with a single vapor bubble.

2.7.1 Large Scale Boiling

This study focuses on large scale boiling (several active nucleation sites) in the nucleate boiling regime using the RPI boiling model or its derivatives as opposed to simulations involving only a single active site. Other numerical models, such as volume-of-fluid (VOF) or a numerical adaptation of the Rohsenow model, have been used by others and will be discussed in this section.

In 2012, Domalapally, et al. [38] simulated flow boiling inside the first wall of the International Thermonuclear Experimental Reactor (ITER) by using two CFD approaches and compared the results with experimental data. The first numerical approach utilized the STAR-CCM+ software package and combined the Rohsenow model for the nucleate boiling regime with a Volume-of-Fluid (VOF) method for the film boiling regime. The

Rohsenow model was given by Eq. (2.29) and VOF was used to track the liquid-vapor interface with the transition from the nucleate to film boiling regime controlled by an empirically determined critical value for the vapor fraction. The second numerical approach utilized ANSYS Fluent 13.0 and user-defined functions to implement the Bergles-Rohsenow model (B-R), which is given by Eq. (2.34), (2.35) and (2.36),

$$\dot{q}''_{total} = [(\dot{q}''_C)^2 + (\dot{q}''_{FDB} - \dot{q}''_{ONB})^2]^{1/2} \tag{2.34}$$

$$\dot{q}''_{FDB} = \left(\frac{T_w - T_{sat}}{C_s}\right)^3 \tag{2.35}$$

$$\dot{q}''_{ONB} = \left(\frac{k_l h_{lv} \rho_v}{8\sigma T_{sat}}\right)\left(T_{w,ONB} - T_{sat}\right)^2 \tag{2.36}$$

where the total wall heat flux is composed of three components: $\dot{q}''_C$ is the convective heat flux (same as RPI boiling model), $\dot{q}''_{FDB}$ is the fully developed boiling heat flux and $\dot{q}''_{ONB}$ is the heat flux at the onset of nucleate boiling [39]. C_s is an empirical constant, $T_{w,ONB}$ is the surface temperature at the onset of nucleate boiling and the other parameters have been previously defined. The simulated geometry was a flat channel with various power and inlet velocity combinations. For the Rohsenow model, the predicted results were within 5% of experimental data over the range of simulated heat fluxes. For the B-R model, agreement with experimental data was dependent on the heat flux simulated and its location relative to CHF; for low to moderate heat fluxes, agreement with within 8%; however, agreement worsened to 14% near CHF. The better agreement with the Rohsenow model was attributed to the inclusion of a VOF model that better accounted for the vapor phase [38].

In 2014, Ningegowda and Premachandran [40] numerically modeled 2D film boiling using a Coupled Level Set and Volume of Fluid (CLSVOF) method. The VOF portion of the method and its advantages in models with a large percentage of vapor have been previously discussed; the level set portion of the method enhances the numerical capability when modelling topological changes, such as the numerous peaks and valleys associated with film boiling. Ningegowda and Premachandran simulated a heated horizontal flat plate under film boiling conditions with water and R-134a and various wall superheats and Reynolds numbers. They validated their numerical results with analytical results for the same geometry and found good agreement for the heat transfer coefficient and shear stress [40]. A CLSVOF method has also been used with 3D geometries and incompressible two-phase flows as with the work by Sussman and Puckett [41]. This section briefly acknowledges some of the other numerical techniques available for simulating multiphase flow where many nucleation sites are active; the next section briefly discusses qualitative modeling of single bubble dynamics.

2.7.2 Single Bubble Dynamics

In 2005, Mukherjee and Kandlikar [42] simulated the growth of a single vapor bubble in a 200 μm microchannel. Their numerical technique was a combination of the semi-implicit method for pressure-linked equations revised (SIMPLER) for solving the Navier-Stokes, continuity and energy equations and a level-set method for capturing the liquid-vapor interface. Mukherjee and Kandlikar compared the numerical results with qualitative observations from experiments and found consistent behavior. The bubble growth rate was initially constant until the bubble filled the channel and began to rapidly expand in the axial direction. The dependence of the growth rate on superheat, Reynolds

number and gravity was also explored by Mukherjee and Kandlikar; they found that the growth rate increased as the liquid temperature increased or the Reynolds number decreased and was not affected by gravity in their case.

In 2013, Gong and Cheng [43] used another technique for simulating the dynamics of a single bubble based on the lattice Boltzmann method (LBM), which uses the thermodynamic relationships defined by equations of state to perform direct numerical simulation of liquid-vapor phase change. The simulated geometry was a 2D horizontal microheater (compared to the bubble size) under constant wall temperature and constant heat flux conditions with water as the working fluid. Gong and Cheng found that as the contact angle increased, the bubble release period would also increase, but there was minimal effect on the bubble departure diameter. They also found that as the superheat increased, the bubble departure diameter would increase while the release period would decrease. In addition to these trends, Gong and Cheng stated that the lattice Boltzmann method allowed them to obtain other information, in particular the nucleation temperature under constant heat flux conditions and the nucleation waiting time, which they claimed were not able to be found using other numerical techniques [43].

In 2013, Sun and Li [44] also used the lattice Boltzmann method to simulate the 3D growth and departure of a single bubble from a horizontal heated wall. They demonstrated that the bubble departure diameter was proportional to gravity and linearly related to the Jacob number and produced velocity and temperature fields that supported the transient micro-convection model. Lastly, Sun and Li expanded the lattice Boltzmann model to include the interaction between two nucleating bubbles. The next section will complete this chapter with conclusions drawn from the literature.

2.8 Conclusions from Literature

The RPI boiling model by Kurul and Podowski has been detailed and examined extensively from its implementation in ANSYS Fluent 14.0 to the numerous times it was used to model boiling in the literature. The RPI boiling model with default and built-in functions has simulated a range of not only geometries but also working fluids and has resulted in good agreement with experimental data. When built-in functions have proven to be insufficient, UDFs were able to improve simulation results. Throughout the literature review, two boiling parameters – nucleation site density and bubble departure diameter – have remained somewhat mysterious. Therefore, this study will focus on using UDFs to explore these boiling parameters and use experimental data in place of built-in functions where possible to achieve better agreement when modeling multiphase flow of dielectrics in pool and flow boiling scenarios.

Chapter 3

MULTIPHASE SIMULATION SETUP IN ANSYS FLUENT 14.0

In this chapter, the multiphase and viscous models used to simulate boiling will be detailed first followed by the typical simulation setup including phase interaction, solution methods, solution controls, solution initialization and convergence criteria. Unless stated otherwise, the models and methods described in this chapter were used when generating the simulation results in the subsequent chapters.

3.1 Multiphase and Viscous Models

In this section, the multiphase and viscous models will be described. In addition to these, radiation models are available in Fluent; however, radiation was ignored in all simulations and those models will not be discussed. For the multiphase model, a modified form of the RPI boiling model, the Non-Equilibrium boiling model, which was introduced in the previous chapter, was used exclusively unless specified otherwise. Both the Non-Equilibrium and RPI boiling models are based on separating the wall heat flux into several components, which include convective, quenching and evaporative heat fluxes as described previously. The difference between the models is how the vapor temperature is handled. In the basic RPI boiling model, the vapor temperature is held at the saturation temperature and is never calculated. This approach is acceptable for relatively low heat fluxes; however, as critical heat flux or the departure from nucleate boiling regime is approached, the Non-Equilibrium boiling model is recommended [20].

Simulation results for relatively low heat fluxes comparing the use of both multiphase models will be shown in the next chapter.

The Non-Equilibrium boiling model allows variable vapor temperature and as a result, the original partitioning of the wall heat flux into three components given by Eq. (2.6) is modified to include two additional terms. The modified equation is given below:

$$\dot{q}''_W = \left(\dot{q}''_C + \dot{q}''_Q + \dot{q}''_E\right) f\left(v_{f,l}\right) + \left(1 - f\left(v_{f,l}\right)\right) \dot{q}''_V + \dot{q}''_G \tag{3.1}$$

where $\dot{q}''_C$, $\dot{q}''_Q$ and $\dot{q}''_E$ are the same three components of the wall heat flux used by the RPI boiling model for convective, quenching and evaporative heat flux described by Eq. (2.7), (2.8) and (2.9), respectively. The two additional heat flux terms, $\dot{q}''_V$ and $\dot{q}''_G$, denote the convective heat flux of the vapor phase and the heat flux to any other gas phases in the model for situations with additional fluids. For the boiling situations in this study, there is only one gas phase due to the vapor phase of Novec 649; therefore, $\dot{q}''_G$ is zero for this study. In Eq. (3.1), $f\left(v_{f,l}\right)$ is a functional term that depends on the liquid volume fraction, $v_{f,l}$, and numerically smoothes the transition from the nucleate boiling regime to the critical heat flux regime [21]. $f\left(v_{f,l}\right)$, is an empirical relationship proposed by Lavieville, et al. [20, 21], given by Eq. (3.2),

$$f\left(v_{f,l}\right) = \begin{cases} 1 - \dfrac{1}{2} e^{-20\left(v_{f,l} - v_{f,crit}\right)} & v_{f,l} \geq v_{f,crit} \\ \dfrac{1}{2}\left(\dfrac{v_{f,l}}{v_{f,crit}}\right)^{20\left(v_{f,crit}\right)} & v_{f,l} < v_{f,crit} \end{cases} \tag{3.2}$$

where $v_{f,crit}$ is a dimensionless, empirical constant equal to 0.2 determined by Lavieville,

et al. [21] to represent the critical value for the void fraction. The next model that will be discussed is the viscous model and associated turbulence models used in this study.

For the viscous model, the two flow regimes are laminar and turbulent with various models associated with the latter. Due to the chaotic nature of vapor bubbles and the boundary layer disruption due to bubble formation and departure, multiphase flow is inherently turbulent in nature; therefore, all numerical simulations were performed using one of the turbulent solvers, in particular a form of the two-equation k-ε model, where k is the turbulent kinetic energy and ε is the turbulent dissipation rate. In ANSYS Fluent 14.0, there are three k-ε models—standard, realizable and renormalization group (RNG)—in addition to other turbulence models.

In terms of capability, both the RNG and realizable k-ε models provide enhancements over the standard k-ε model. These models are recommended when flow patterns are dominated by smaller scales of motion, such as the vapor bubble dynamics in the boundary layer near the wall [20]. In terms of computational cost, the standard k-ε model is the least expensive while the realizable k-ε model is the most computationally expensive. In addition, Fincher [13] determined that the k-ε RNG model was the most stable in these multiphase simulations; therefore, this turbulence model was used for most of the simulations performed in this study. In the next chapter, the k-ε RNG model is briefly compared with other turbulence models, such as k-ε standard and k-ω standard, to determine the effect of the turbulence model on the results. It will be shown that the surface temperature predicted varied minimally based on the selected turbulence model. For more information on the various turbulence models and the related transport equations, see [20]. With all multiphase models, the interaction between phases including

drag and lift forces among other parameters must be defined. The next section will detail the phase interaction models along with mathematical expressions where necessary.

3.2 Phase Interaction

The number of phases available will affect how the phase interaction is defined with increasing complexity as the number of phases increases. In this study, there are only two phases of interest—liquid and vapor Novec 649. A phase interaction model, typically an empirical relationship, is needed for the following parameters: drag, lift, heat and mass. All of the selected phase interaction models were chosen due to recommendations from [20] based on the flow or due to prior work from Fincher [13].

3.2.1. Drag Coefficient

For the drag force between phases in boiling situations, an empirical relationship developed by Ishii [45] is used in which the drag coefficient, C_D, is the minimum of two values. The Ishii drag model is defined as follows:

$$\mathrm{C_D} = \min\left(\mathrm{C_D^{vis}}, \mathrm{C_D^{dis}}\right) \tag{3.3}$$

$$\mathrm{C_D^{vis}} = \frac{24}{\mathrm{Re}}\left(1 + 0.15\mathrm{Re}^{0.75}\right) \tag{3.4}$$

$$\mathrm{C_D^{dis}} = \frac{2}{3}\frac{\mathrm{d_p}}{\sqrt{\frac{\sigma}{\mathrm{g}|\rho_\mathrm{q} - \rho_\mathrm{p}|}}} \tag{3.5}$$

where Re is the Reynolds number based on the relative velocity between phases and the bubble diameter, σ is the surface tension, ρ is the density based on phase p or q, g is the gravitational acceleration constant and d_p is the bubble diameter, not to be confused with

the bubble departure diameter. The superscripts “vis” and “dis” denote the viscous regime and the distorted or inertial regime, respectively. In the viscous regime, vapor bubble and fluid particles are approximated as small, spherical objects and the drag coefficient is related to the Reynolds number; however, in the distorted or inertial regime, surface tension effects are more significant and the drag coefficient for vapor bubbles or fluid particles is no longer dependent on the Reynolds number and instead depends on the size of the bubble and the relative magnitudes of the gravitational and surface tension forces [20, 45]. There are five other drag models available in ANSYS Fluent 14.0 that will not be discussed in detail; however, the Schiller-Naumann model is the most generic drag coefficient model while the Tomiyama et al. model is recommended for liquid-vapor flows where the shape and size of the bubbles can vary significantly [20]. The Ishii model is recommended for boiling flows [20] and was used exclusively by Fincher [13] in his pool and flow boiling simulations.

3.2.2 Lift Coefficient

In ANSYS Fluent 14.0, there are a total of four models for the lift coefficient and similar to the drag coefficient, for boiling flows one model is recommended more highly than the others. The lift model is based on work by Moraga et al. [46] in which two phenomena, classical aerodynamic lift and vorticity-induced lift, are combined to determine the lift coefficient, C_l [20, 46]. The Moraga et al. model for lift is given by the following set of equations, where Eq. (3.6) is a particle Reynolds number and Eq. (3.7) is a vorticity Reynolds number.

$$\mathrm{Re}_{\mathrm{par}} = \frac{\rho_q |\vec{V}_q - \vec{V}_p| d_p}{\mu_q} \tag{3.6}$$

$$\mathrm{Re}_{\omega} = \frac{\rho_q |\nabla \times \vec{V}_p| d_p^2}{\mu_q} \tag{3.7}$$

$$C_l = \begin{cases} 0.0767 & \varphi \leq 6000 \\ -\left(0.12 - 0.2e^{-\frac{\varphi}{3.6}\times 10^{-5}}\right) e^{\frac{\varphi}{3}\times 10^{-7}} & 6000 < \varphi < 5 \times 10^7 \\ -0.6353 & \varphi \geq 5 \times 10^7 \end{cases} \tag{3.8}$$

In the previous set of equations, Re is the Reynolds number, ρ is the density, $\vec{V}$ is the velocity vector, d_p is the bubble diameter and μ is the dynamic viscosity. The subscripts p and q on the fluid property and velocity terms denote the primary and secondary phases, respectively, while the subscripts *par* and ω on the Reynolds numbers denote the particle or vorticity Reynolds number, respectively. In Eq. (3.8), φ is a dimensionless combination of Reynolds numbers given by the following:

$$\varphi = \mathrm{Re}_{\mathrm{par}} \times \mathrm{Re}_{\omega} \tag{3.9}$$

where the particle and vorticity Reynolds numbers are found from Eq. (3.6) and (3.7). The Moraga et al. model for lift is recommended for general boiling flow and is one of four available models in ANSYS Fluent 14.0. Depending on the scale of the vapor bubbles, one of the other models may be more applicable. For example, the Legendre-Magnaudet model is recommended for very small diameter fluid particles while the Tomiyama model is recommended for larger-scale vapor bubbles in which deformation of the bubbles is also of interest [20].

3.2.3 Heat Transfer

For the heat transfer between phases, there are five models for the Nusselt number

correlation along with the ability to provide either a constant value or a user-defined function. For all numerical simulations, the Ranz-Marshall [47] expression as given by the following equation is used:

$$\mathrm{Nu_p} = 2.0 + 0.6\mathrm{Re_p^{1/2}Pr_q^{1/3}} \tag{3.10}$$

where Re_p the Reynolds number based on the properties of phase p and a relative velocity between the phases, $|\vec{V}_p - \vec{V}_q|$, and Pr_q is the Prandtl number of phase q [20, 47]. The Ranz-Marshall expression for heat transfer is the default correlation with other models ranging in complexity from simple modifications of the coefficients and exponents in Eq. (3.10) to more detailed expressions involving additional terms or a piecewise function for the Nusselt number based on the range of the Prandtl number [20].

3.2.4 Mass Transfer

When defining mass transfer in ANSYS Fluent 14.0, the number of mass transfer mechanisms and the mechanism itself need to be specified. For the two-phase simulations in this study, there is only one available mass transfer path and that is from the liquid phase to the vapor phase; a condenser is not included in the numerical model and mass transfer does not occur from the vapor phase to the liquid phase. The mechanism for mass transfer used in this study is the previously described Non-Equilibrium boiling model that requires four boiling parameters to be specified. These boiling parameters are the area of influence, frequency of bubble departure, bubble departure diameter and nucleation site density. Each of these boiling parameters includes at least one built-in empirical correlation along with the ability to set user-defined functions. The majority of this study involves the exploration of various functions for bubble departure diameter and

nucleation site density including combinations of functions provided by ANSYS Fluent as well as user-defined functions.

The Non-Equilibrium boiling model and the four boiling parameters are the most significant portion of this study; therefore, the various correlations will not be discussed in this section, but rather in the following chapter where the simulation results using those correlations will also be discussed. This concludes the section on phase interactions for boiling models. There are several other phase interaction parameters, such as wall lubrication, collision and slip, that are not relevant for the boiling simulations in this study and thus no models were selected or discussed. For more information on phase interaction parameters, see [20] or Appendix A of this study.

3.3 Solution Methods

In this section, the solution method used in all numerical simulations will be discussed; this consists of the pressure-velocity scheme as well as the spatial discretization for the gradient, momentum, volume fraction and energy quantities among other terms. The default algorithm for multiphase simulations is an adaptation of the semi-implicit method for pressure-linked equations (SIMPLE) known as the phase-coupled SIMPLE (PC-SIMPLE) method [20]. In addition to phase coupling, in which the velocity components are solved coupled based on the liquid or vapor phase, the pressure and velocity terms are also coupled with volume fractions [20].

The numerical scheme for spatial discretization of gradient, momentum, volume fraction and energy will be briefly discussed. A least squares cell based scheme is used for the gradient and a first order upwind scheme is used for momentum, volume fraction, turbulent kinetic energy, turbulent dissipation rate and energy [20]. Higher order schemes

are available; however, to minimize computational costs, the discretization scheme was limited to first order only.

3.4 Solution Controls

In the previous section, the solution methods or solvers for the conservation equations were discussed. In this section, the precision, stabilization and relaxation factors are discussed. Double precision was used and a bi-conjugate gradient stabilizer (BCGSTAB) was used in all numerical simulations.

The next set of solution control variables includes the dimensionless flow Courant number and relaxation factors for momentum and pressure. While the simulations in this study were all steady state, the Courant number was relevant due to some of the conservation laws being solved using a pseudo transient approach in ANSYS Fluent. The default value is 200 for the Courant number and 0.75 for both the momentum and pressure relaxation factors [20]. While the values for these solution control variables can vary based on the type of simulation—pool or flow boiling—or the magnitude of the wall heat flux, the default values are much too high based on observations by Fincher [13]. Due to the complex 3D geometry, the flow Courant number was typically reduced to 10 while the relaxation factors for momentum and pressure were reduced to 0.55 and 0.25, respectively. When instability occurs, the relaxation factors may be reduced further.

The next group of solution controls is another set of relaxation factors for density, body forces, volume fraction, turbulent kinetic energy, turbulent dissipation rate, turbulent viscosity and energy. The default values are 0.5 for the turbulent terms and 1.0 for the other terms; however, per recommendations by Fincher [13], these relaxation factors were reduced for multiphase simulations. The typical starting values were

approximately half of the default values or 0.3 for the turbulent terms and 0.6 for the other terms. As with the flow Courant number and relaxation factors for pressure and momentum, these values can be model and case dependent and may be reduced further.

3.5 Solution Initialization

The numerical simulations involved an iterative procedure and as such, values for several variables, such as temperature or turbulent kinetic energy, were initialized to provide a starting point for the calculations. In both pool and flow boiling simulations, the liquid temperature was initialized to the subcooled pool temperature of Novec 649, typically 15°C below the saturation temperature or 34°C. Other levels of subcooling were also simulated and in those situations, the initialized liquid temperature was adjusted accordingly. As Novec 649 was the only fluid simulated, the vapor temperature was initialized to the saturation temperature of Novec 649, or 49°C, in all simulations.

In Section 3.1, the viscous model used was discussed and the turbulent nature of boiling flow necessitated the use of a turbulent solver, in particular the two-equation, k-ε RNG model. These two-equation models introduce, turbulent kinetic energy (TKE) and turbulent dissipation rate (TDR), which have default initialized values of 1 m^2/s^2 and 1 m^2/s^3, respectively. The initialized value for TKE was determined to be much too high for the velocity scale of interest and resulted in instabilities. In pool and flow boiling, the maximum velocity was relatively small (on the order of magnitude of 10^{-1} to 10^{-2} m/s). TKE is of the order of magnitude of the turbulent velocity fluctuations squared. The fluctuations are smaller than the mean velocities, so the default initial TKE was too high for the flows studied here. By reducing it to 0.0001 m^2/s^2 and leaving the initialized value for TDR at 1 m^2/s^3, solution convergence was achieved.

3.6 Convergence Criteria

Lastly, the convergence criteria will be discussed in this section. Several numerical residuals were monitored; these values were determined by ANSYS Fluent 14.0 from the conservation equations for mass, momentum and energy applied to both the liquid and vapor phases. In addition to the residuals for continuity, TKE, TDR and vapor fraction, there were pairs of residuals for the x, y and z-direction velocities and energy for the liquid and vapor phases. For multiphase simulations with the k-ε RNG turbulent model, there were 12 total residuals being monitored for convergence. Convergence was determined to be achieved when all residuals were less than 10^{-5} with liquid phase velocity residuals typically less than 10^{-6} and energy residuals typically less than 10^{-7}. In addition to tracking the residuals, the average die temperature was monitored and in all cases, the change in temperature from one iteration to the next was less than 0.01°C for over 250 iterations upon completion of the simulation.

This concludes the general discussion of the multiphase simulation setup using ANSYS Fluent 14.0. The boiling models, viscous models, solution controls, etc., described in this chapter were used in all numerical simulations unless stated otherwise. In the next chapter, simulation results will be presented for pool boiling of Novec 649 using various functions for bubble departure diameter and nucleation site density, including built-in and user-defined functions. After the pool boiling results are presented, flow boiling of Novec 649 using a select few combinations of functions for bubble departure diameter and nucleation site density will be presented for a cartridge model based on work by Gess [35].

Chapter 4

MULTIPHASE SIMULATIONS

In this chapter, numerical results for multiphase simulations including pool boiling and flow boiling will be presented along with comparisons to experimental data when available. ANSYS Icepak 14.0 was used to build the models while ANSYS Fluent 14.0 was used to perform the simulations due to limited or non-existent multiphase capability in Icepak. Previous work involving multiphase simulation of dielectrics by Fincher [13] used the RPI boiling model, which does not calculate the vapor phase temperature. A modified version of the RPI boiling model, known as the Non-Equilibrium boiling model, was used to include the vapor temperature. This chapter begins by briefly summarizing these two models along with the four boiling parameters required to close the model equations; these boiling parameters are area of influence, frequency of bubble departure, bubble departure diameter and nucleation site density.

After reintroducing the boiling models, pool boiling simulation results using the Non-Equilibrium boiling model are presented along with comparisons with experimental data from Ramakrishnan, et al. [48] and previous numerical results from Fincher [13] in which the RPI boiling model was used. The first set of pool boiling results included four combinations of the built-in bubble departure diameter (BDD) and nucleation site density (NSD) functions. Attention was then turned to user-defined functions for BDD and NSD; six functions for BDD based on experimental data from Sridhar, et al. [19] and twelve

functions for NSD were simulated while the other function was kept constant. After modifying BDD and NSD individually, combinations of these user-defined functions were used together, all while using BDD functions most representative of experimental data. Other functional forms for NSD, such as piecewise or nonlinear, were also explored. The last set of pool boiling simulations involved various levels of subcooling and various turbulence models.

After the pooling boiling results are discussed, flow boiling simulation results are presented based on the experimental setup and results from Gess [35, 50] using a small form-factor immersion cooled cartridge module. These simulations attempt to extend the BDD and NSD functions used with dielectric fluids in pool boiling to flow boiling situations.

4.1 Reintroduction of the Multiphase Boiling Models

In this section, the most applicable multiphase boiling models available in ANSYS Fluent 14.0 are briefly reintroduced. The two boiling models include the RPI boiling model and the Non-Equilibrium boiling model, both of which are based on separation of the wall heat flux into several components. The RPI boiling model used extensively by Fincher [13] is presented first followed by the Non-Equilibrium boiling model used in this study. To close either of the boiling models, functions for area of influence, frequency of bubble departure, bubble departure diameter and nucleation site density need to be specified. The built-in functions for these boiling parameters will also be reintroduced in this section.

4.1.1 RPI Boiling Model

The unmodified RPI nucleate wall boiling model separates the wall heat flux into three quantities: a convective, a quenching and an evaporative heat flux and is given by Eq. (4.1).

$$\dot{q}''_W = \dot{q}''_C + \dot{q}''_Q + \dot{q}''_E \tag{4.1}$$

The convective heat flux, $\dot{q}''_C$, is a measure of the energy transfer due to the bulk fluid motion and is given by Eq. (4.2),

$$\dot{q}''_C = h_C\left(T_w - T_{pool}\right)\left(1 - A_b\right) \tag{4.2}$$

where h_C is the single phase heat transfer coefficient and T_w and T_{pool} are the wall and bulk fluid temperatures, respectively. The fraction of the surface area not covered by nucleating bubbles is accounted for by $(1 - A_b)$.

The quenching heat flux, $\dot{q}''_Q$, is given by Eq. (4.3).

$$\dot{q}''_Q = \frac{2k_l}{\sqrt{\pi\alpha_l t}}\left(T_w - T_{pool}\right) \tag{4.3}$$

This heat flux is a measure of the energy transfer due to liquid filling the empty regions near the wall after a vapor bubble departs the surface. Quenching heat flux is a cyclic averaged, time-dependent term, where each cycle includes bubble formation and departure. In Eq. (4.3), k_l is the liquid thermal conductivity, α_l is the liquid thermal diffusivity and t is the periodic time, in seconds, for a vapor bubble to form and detach from the surface.

The evaporative heat flux, $\dot{q}''_E$, accounts for phase change heat transfer and is given by Eq. (4.4),

$$\dot{q}''_E = V_d N_w \rho_v h_{lv} f \tag{4.4}$$

where V_d is the volume of the vapor bubble, N_w is the nucleation site density, ρ_v is the vapor density, h_{lv} is the latent heat of vaporization, f is the frequency of bubble departure and is the inverse of the periodic time, t, given in Eq. (4.3).

This concludes the reintroduction of the basic RPI boiling model. The primary difference between this multiphase model and the Non-Equilibrium boiling model, reintroduced next, is how the vapor phase temperature is handled. In the RPI boiling model, the vapor temperature remains fixed at the saturation temperature, whereas the Non-Equilibrium boiling model accounts for the temperature of all phases. For relatively low heat fluxes, the RPI and Non-Equilibrium boiling models predict similar die surface temperatures as will be shown when numerical results from this study are compared with those of Fincher [13]. However, at heat fluxes approaching critical heat flux and the departure from nucleate boiling regime, the Non-Equilibrium boiling model is recommended [20].

4.1.2 Non-Equilibrium Boiling Model

As discussed previously, the Non-Equilibrium boiling model is based on the RPI boiling model in that both separate the wall flux into several components; however, the Non-Equilibrium boiling model introduces two additional heat fluxes to account for temperatures beyond the primary phase. In two-phase simulations, the primary phase is

the liquid phase while the secondary phase is the vapor phase. The modified heat flux partition equation is given by Eq. (4.5),

$$\dot{q}''_W = \left(\dot{q}''_C + \dot{q}''_Q + \dot{q}''_E\right) f\left(v_{f,l}\right) + \left(1 - f\left(v_{f,l}\right)\right) \dot{q}''_V + \dot{q}''_G \tag{4.5}$$

where $\dot{q}''_C$, $\dot{q}''_Q$ and $\dot{q}''_E$ are the convective, quenching and evaporative heat fluxes described by Eq. (4.2), (4.3) and (4.4), respectively. $\dot{q}''_V$ is the vapor phase convective heat flux whose functional form is similar to the liquid phase convective heat flux, given by Eq. (4.2). $\dot{q}''_G$ is another convective heat flux used to represent heat transfer to additional gas phases. For two-phase simulations in this study, $\dot{q}''_G$ is zero. $f\left(v_{f,l}\right)$ is a dimensionless empirical expression meant to smooth the transition from the nucleate boiling regime to the critical heat flux regime and was developed by Lavieville, et al. [20, 21] based on the dimensionless liquid volume fraction, $v_{f,l}$, local to the heat generating wall; it is defined by the following,

$$f\left(v_{f,l}\right) = \begin{cases} 1 - \frac{1}{2} e^{-20\left(v_{f,l} - v_{f,crit}\right)} & v_{f,l} \geq v_{f,crit} \\ \frac{1}{2}\left(\frac{v_{f,l}}{v_{f,crit}}\right)^{20\left(v_{f,crit}\right)} & v_{f,l} < v_{f,crit} \end{cases} \tag{4.6}$$

where $v_{f,crit}$ is the critical value for the void fraction and is a dimensionless, empirically determined constant by Lavieville, et al. [20, 21] equal to 0.2. This concludes the reintroduction of the Non-Equilibrium boiling model. Regardless of the boiling model used, four boiling parameters need to be specified to fully close the heat flux expressions and capture the boiling physics. The built-in, default functions for these boiling parameters are presented in the next section.

4.1.3 Boiling Parameters

In order to fully close the previous heat flux expressions for the multiphase models, four boiling parameters need to be specified; these are the area of influence, frequency of bubble departure, bubble departure diameter and nucleation site density. In ANSYS Fluent, each of these boiling parameters has at least one built-in relationship, typically derived from empirical results where water was the working fluid, along with the option of supplying alternative expressions via user-defined functions (UDFs). Because of the unbounded nature of the area of influence expression, it has been limited using a floor to prevent numerical instabilities [20]. It is given by the following set of equations, in dimensionless units,

$$A_b = \min\left(1, K\frac{N_w \pi (D_w)^2}{4}\right) \tag{4.7}$$

$$K = 4.8\exp\left(-\frac{Ja_{sub}}{80}\right) \tag{4.8}$$

$$Ja_{sub} = \frac{\rho_l C_{pl}\left(T_{sat} - T_{pool}\right)}{\rho_v h_{lv}} \tag{4.9}$$

where K is a dimensionless empirical constant based on work by Del Valle and Kenning [23] and Ja_{sub} is the subcooled Jacob number. In the preceding set of equations, D_w is the bubble departure diameter, ρ_l is the liquid density, C_{pl} is the liquid specific heat, T_{sat} is the saturation temperature and the other terms have been previously defined.

The frequency of bubble departure, f, in units of s^{-1} is inversely related to the periodic time for bubble formation and departure used in Eq. (4.3) for the quenching heat flux. It is based on empirical results from Cole [24] and is given by Eq. (4.10),

$$f = \frac{1}{t} = \sqrt{\frac{4g(\rho_l - \rho_v)}{3\rho_l D_w}} \tag{4.10}$$

where each term has been previously defined except g, which is gravitational acceleration. The third boiling parameter is the active nucleation site density based on wall superheat, N_w, and is given by Eq. (4.11),

$$N_w = C^n(T_w - T_{sat})^n \tag{4.11}$$

where C and n are empirical constants based on work by Lemmert and Chawla [25] whose values are 210 and 1.805, respectively. Nucleation site density is in units of m^{-2} when the wall and saturation temperatures are in units of °C or K. This study explored various values of C and n to expand application of this nucleation site density expression to better represent dielectric fluids, particularly Novec 649. The final boiling parameter is the bubble departure diameter, D_w, given by Eq. (4.12),

$$D_w = \min\left[0.0014\text{m}, (0.0006\text{m})e^{\left(-\frac{T_{sat}-T_{pool}}{45.0\text{K}}\right)}\right] \tag{4.12}$$

which has units of meters when the saturation and pool temperatures are in units of °C or K Like the area of influence, a floor is imposed on the empirical relationship developed by Tolubinski and Kostanchuk [26] to prevent numerical instabilities [20]. This study also explored alternative expressions for bubble departure diameter similar to Eq. (4.12).

All of the expressions for the four boiling parameters presented previously are modified forms of empirical correlations determined from experiments in which water was the working fluid. The expressions presented in this section are the default models

provided by ANSYS Fluent; however, additional models are available along with the ability to input alternative, user-defined functions.

4.2 Pool Boiling Simulations

In this section, the numerical results for pool boiling of a simplified multichip module submerged in a quiescent pool of Novec 649 will be presented and discussed. The model is described first following by the results, which are compared with experimental data from Ramakrishnan, et al. [48] and similar numerical results from Fincher [13] when available. The numerical results presented first explore combinations of the boiling parameter models presented in the previous section as well as other built-in options to determine their suitability in modeling multiphase pool boiling of dielectric fluids. For all simulations, area of influence and frequency of bubble departure were modeled using Eq. (4.7) and (4.10), respectively, while nucleation site density and bubble departure diameter varied by case.

After parametric exploration of the built-in functions, various expressions were used in place of the built-in nucleation site density function while the other three boiling parameters were kept as default. Then, bubble departure diameter was varied while the other three boiling parameters were unchanged. Experimental data for bubble departure diameter at the appropriate degree of subcooling from Sridhar, et al. [19] was also included. The last set of numerical results includes variations of the level of subcooling and the turbulence model used.

4.2.1 Numerical Simulation of a Single Die in Novec 649

All pool boiling simulations were performed using a numerical model for a single die attached to a printed circuit board vertically suspended in a quiescent pool of

subcooled Novec 649. With the exception of results towards the end of this chapter in which the level of subcooling varied, the pool of Novec 649 was subcooled 15°C. Additional information on the numerical model including geometry and meshing is given in the next section.

4.2.1.1 Model Description

The numerical modeling was performed using two commercially available software packages for electronics thermal management and computational fluid dynamics. ANSYS Icepak was used to create the model, including defining the geometric features and generating the mesh, while ANSYS Fluent was used to set boiling parameters, define fluid properties and perform the simulations. The numerical model in this study was a simplified form of an experimental board shown in Figure 4.1.

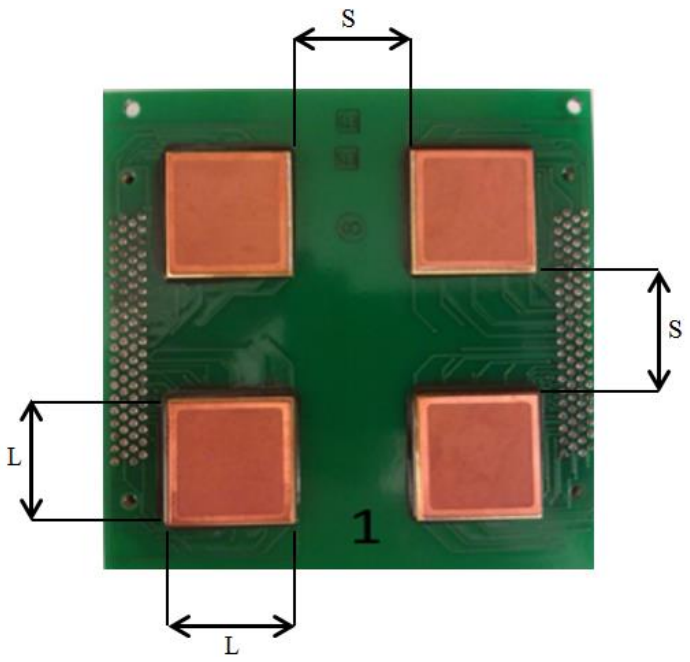

Figure 4.1: Layout of the Four Die, Experimental Model [48]

The original setup consisted of four, equally spaced 24 mm x 24 mm x 0.6 mm die, arranged in a square pattern and centered on a printed circuit board (PCB). The PCB and die were vertically suspended in a large quiescent pool of 15°C subcooled Novec 649. For more information on the experimental setup, see the study by Ramakrishnan, et al. [48]. As determined by Fincher [13], the die are sufficiently spaced that they do not thermally interact with one another allowing the use of a reduced numerical model to decrease computational costs. Heat dissipation from one die was modeled as uniform and ranged from 3 W/cm^2 to 12 W/cm^2 in this study. The model used in all pool boiling simulations is shown in Figure 4.2.

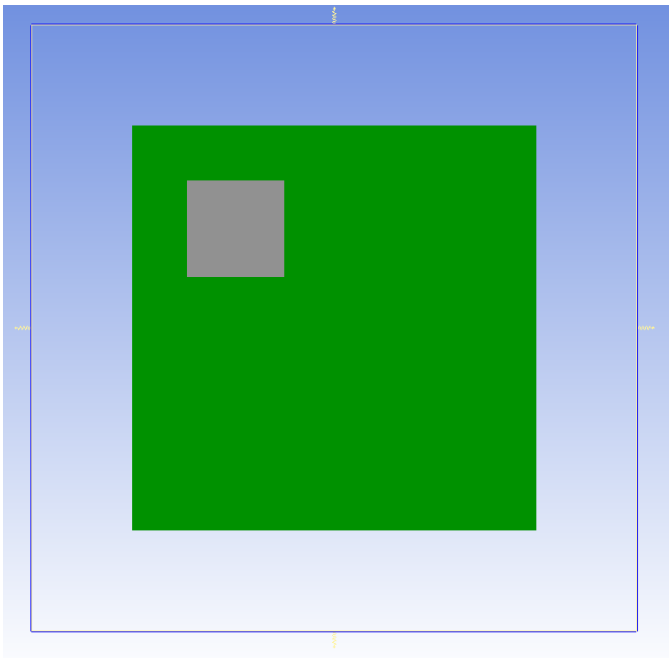

Figure 4.2: Numerical Model Used in Pool Boiling Simulations

Models contained approximately 1.4 million nodes using a conformal mesh. A study of grid size was performed to ensure grid independence. A coarser grid with approximately 1.2 million nodes resulted in a maximum temperature difference of 4°C from the 1.4

million node model. Similarly, a finer grid with approximately 1.7 million nodes resulted in a maximum temperature difference of 1°C. Figure 4.3 shows a vertical cut plane through the model highlighting the mesh that was used.

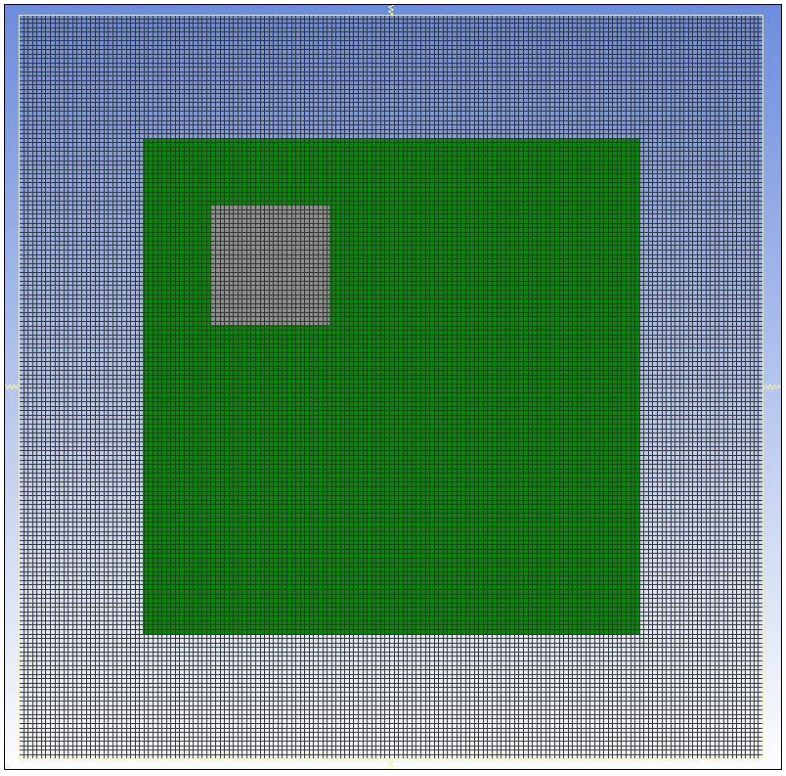

Figure 4.3: Conformal Mesh Used with the Models for Pool Boiling Simulations

This completes the description of the numerical model used in pool boiling simulations; the next section briefly summarizes the ANSYS Fluent solver settings and convergence criteria.

4.2.1.2 Fluent Solver Settings and Convergence Criteria

For pool boiling simulations, the Non-Equilibrium boiling model was used along with the k-ε RNG turbulent model. Radiation was ignored in all cases. For the interaction models between the liquid and vapor phases, the Ishii, Moraga and Ranz-Marshall

models were used for the drag coefficient, lift coefficient and heat transfer, respectively. These correlations were given by Eq. (3.3) to (3.10) in the previous chapter. Pressure and velocity were solved using a coupled with volume fractions scheme and other quantities, such as momentum, turbulent kinetic energy (TKE), turbulent dissipation rate (TDR), etc., were discretized using first order upwind. The relaxation factors for momentum and pressure were set to 0.55 and 0.25, respectively, while relaxation factors were set to 0.3 for turbulent terms (TKE, TDR, turbulent viscosity) and 0.6 for other terms (density, body forces, etc). The nondimensional flow Courant number was set to 10.

For the solution initialization, the liquid phase and vapor phase temperatures were initialized to 307.15K (15°C subcooled) and 322.15K (saturation temperature of Novec 649), respectively. To account for the smaller geometry scale, the initial TKE was reduced from 1 m^2/s^2 to 0.0001 m^2/s^2 while the initial TDR was left as the default value of 1 m^2/s^3. Parallel processing was used in which three to eleven computer cores, depending on the number of simultaneous simulations, were used to reduce computational time. BCGSTAB and double precision were also used. Lastly, full convergence was obtained in all cases with flow terms converging to a minimum of 10^{-5} and energy terms typically converging to a minimum of 10^{-7}.

The majority of the remainder of this chapter is dedicated to presenting and discussing pool boiling results. The first set of results includes four combinations of built-in boiling parameters labeled Case A through Case D.

4.2.1.3 Default NSD and Default BDD (Case A)

ANSYS Fluent provides one additional model for nucleation site density and two additional models for bubble departure diameter beyond the default relationships given

by Eq. (4.11) and (4.12), respectively. Table 4.1 lists the four combinations of built-in boiling parameters that were simulated and compared with experimental data. In the table, "Fluent Default" refers to the models presented in the previous section. Area of influence and frequency of bubble departure are not listed as they were both kept as default, Eq. (4.7) through (4.10), for all cases.

Table 4.1: Summary of Cases for Built-In Parametric Study

Case	Nucleation Site Density	Bubble Departure Diameter
A	Fluent Default, Eq. (4.11)	Fluent Default, Eq. (4.12)
B	Fluent Default, Eq. (4.11)	Kocamustafaogullari-Ishii (K-I) [29]
C	Kocamustafaogullari-Ishii (K-I) [28]	Fluent Default, Eq. (4.12)
D	Kocamustafaogullari-Ishii (K-I) [28]	Kocamustafaogullari-Ishii (K-I) [29]

Fincher [13] numerically simulated Cases A, B and C using the same geometry (Figure 4.2) and fluid (Novec 649) and those results are also presented as a point of comparison in addition to comparisons with experimental data. It should be noted that there are two differences between this numerical model and that of Fincher. While the mesh scheme and overall number of elements were similar, the element dimensions were different potentially resulting in minor discrepancies. More significant, especially at high heat fluxes, was the handling of the vapor temperature. Fincher employed the basic RPI boiling model that does not calculate the vapor temperature and instead maintains it at the saturation temperature while this study employs the Non-Equilibrium boiling model.

Numerical results for Case A, which used the default functions for area of influence, frequency of bubble departure, nucleation site density and bubble departure diameter, are compared to experimental data and Fincher's numerical results in Figure 4.4. The heat fluxes used for the parametric simulations typically ranged from 3 to 9 W/cm^2, which was sufficient to establish general trends and behavior.

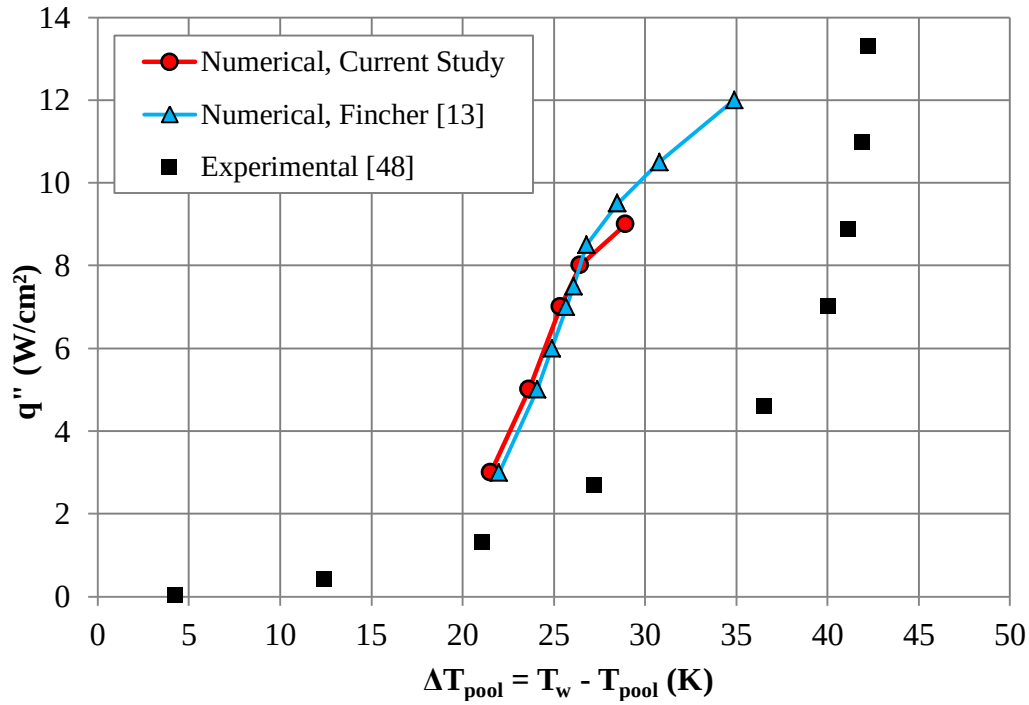

Figure 4.4: Single Die Heat Flux as a Function of Subcooled Temperature Difference with Respect to Maximum Die Temperature, Case A

The two sets of numerical results were similar with the relatively minor differences attributed to mesh variation. The simulated heat fluxes were sufficiently low that critical heat flux was not a concern and the RPI and Non-Equilibrium boiling models resulted in similar die surface temperatures. When compared to experimental results, poor agreement was seen with numerical models under predicting experimental wall temperature rise by up to 15°C. In addition, the increasing slope of heat flux versus wall temperature that is typical of boiling curves was not reproduced by either of the numerical models. Predicted vapor fractions near the die surface were also under predicted by an order of magnitude.

4.2.1.4 Default NSD and K-I BDD (Case B)

For Case B, the bubble departure diameter model was modified to another built-in function while all the other boiling parameters were kept as the default functions. This

alternative model is based on empirical results by Kocamustafaogullari and Ishii [29], abbreviated K-I, and is given by the following,

$$D_w = 0.0012(\rho^*)^{0.9} \times (0.0208 \deg^{-1})\emptyset \sqrt{\frac{\sigma}{g(\rho_l - \rho_v)}} \tag{4.13}$$

$$\rho^* = \frac{\rho_l - \rho_v}{\rho_v} \tag{4.14}$$

where $\emptyset$ is the contact angle between the vapor bubble and surface in degrees and σ is the surface tension in N/m. ρ^* is a nondimensional density defined by Eq. (4.14). Numerical results for Case B are shown in Figure 4.5 along with experimental data and Fincher's numerical results.

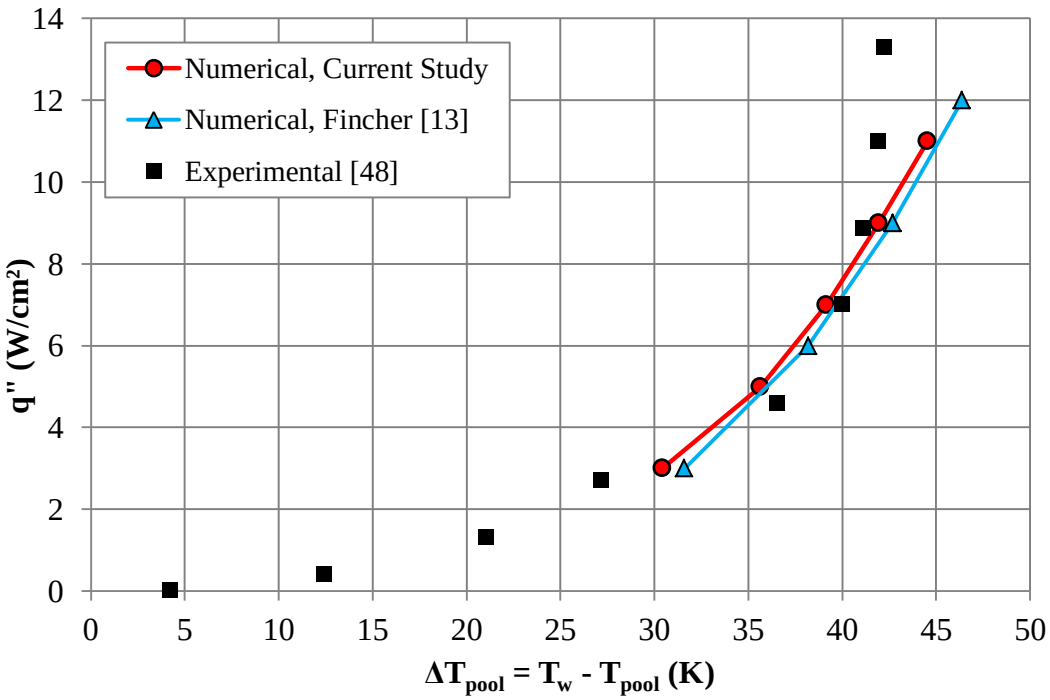

Figure 4.5: Single Die Heat Flux as a Function of Subcooled Temperature Difference with Respect to Maximum Die Temperature, Case B

As with Case A, both sets of numerical results for Case B were similar with the relatively

minor differences in predicted surface temperature being attributed to variations in the mesh. When compared to the experimental results, agreement was significantly improved by applying the K-I model for bubble departure diameter with numerical results over predicting the surface temperature by approximately 4°C at the highest heat fluxes simulated. The numerical models improved as more fluid properties were incorporated into the bubble departure diameter model and less emphasis was placed on empirical relationships. The increasing slope of heat flux as a function of wall temperature typical of boiling curves was replicated to an extent with Case B; however, as heat flux continues to increase beyond 12 W/cm^2, the numerical model will continue to over predict the wall temperature by an ever-increasing amount rendering this model insufficient as CHF is approached.

4.2.1.5 K-I NSD and Default BDD (Case C)

For Case C, the nucleation site density model was modified to another built-in function while all other boiling parameters were kept as the default functions. Like the alternative model for bubble departure diameter, this alternative model for nucleation site density is also based on empirical results by Kocamustafaogullari and Ishii [28]. The set of equations defining this model is given by Eq. (4.15) to (4.18), where ρ^* is the same nondimensional density previously defined by Eq. (4.14).

$$N_w = \frac{N_w^*}{(D_w)^2} \tag{4.15}$$

$$N_w^* = \frac{(2.157 \times 10^{-7})(\rho^*)^{-3.2}(1 + 0.0049\rho^*)^{4.13}}{(r_c^*)^{4.4}} \tag{4.16}$$

$$r_c^* = \frac{2(r_c)}{D_w} \tag{4.17}$$

$$r_c = \frac{2\sigma T_{sat}}{\rho_v h_{lv}(T_w - T_{sat})} \tag{4.18}$$

By introducing several nondimensional variables — radius of the departing vapor bubble, r_c, and fluid density, ρ — the K-I model attempts to incorporate more fluid properties as was done with bubble departure diameter in the Case B model. Numerical results for Case C are shown in Figure 4.6 along with experimental data and Fincher's numerical results.

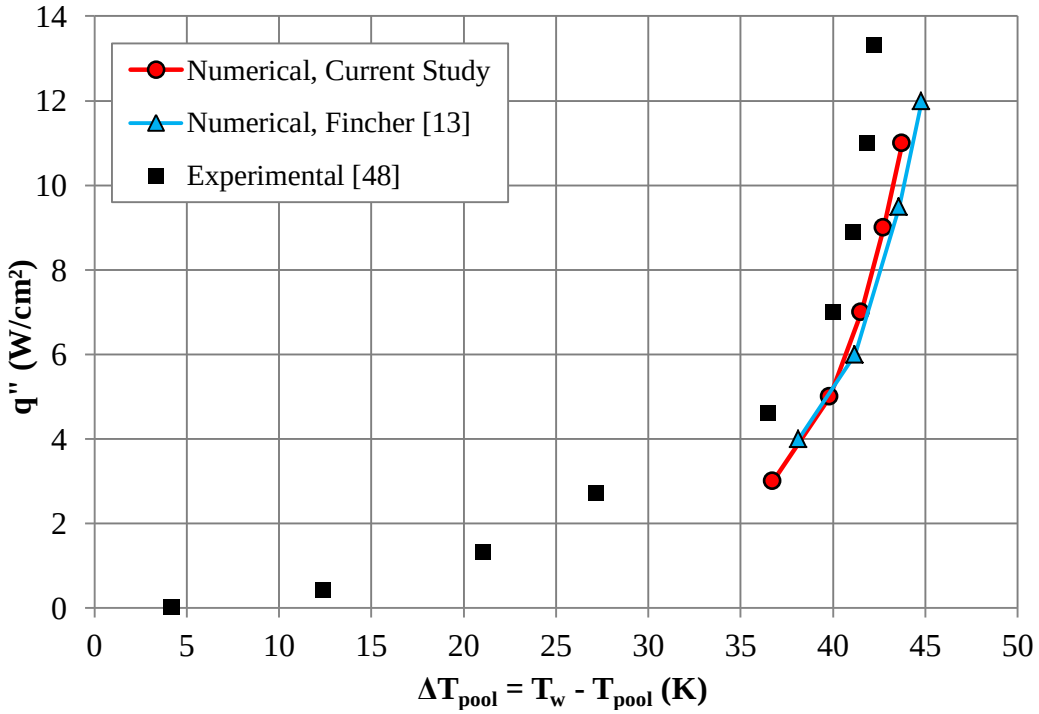

Figure 4.6: Single Die Heat Flux as a Function of Subcooled Temperature Difference with Respect to Maximum Die Temperature, Case C

Again, both sets of numerical results were within fractional degrees of one another. When

compared to experimental results, agreement was not universally better than in the previous case. At the higher heat fluxes, agreement with experimental data was improved as Case C over predicted the die surface temperature by less than 3°C. Also, the increasing slope was more rapid compared to Case B eliminating or reducing the increased over prediction as heat flux increases that was apparent in Case B. However, at lower heat fluxes, particularly those immediately after the transition from single phase to multiphase, agreement with experimental data was worse than Case B. Using the K-I model for nucleation site density resulted in die surface temperatures being over predicted by a maximum of approximately 8°C at 3 W/cm^2 compared to the 2°C over prediction when using the K-I model for bubble departure diameter. The temperature contour for Case C at 9 W/cm^2 is shown in Figure 4.7 to illustrate the essentially uniform die surface temperature.

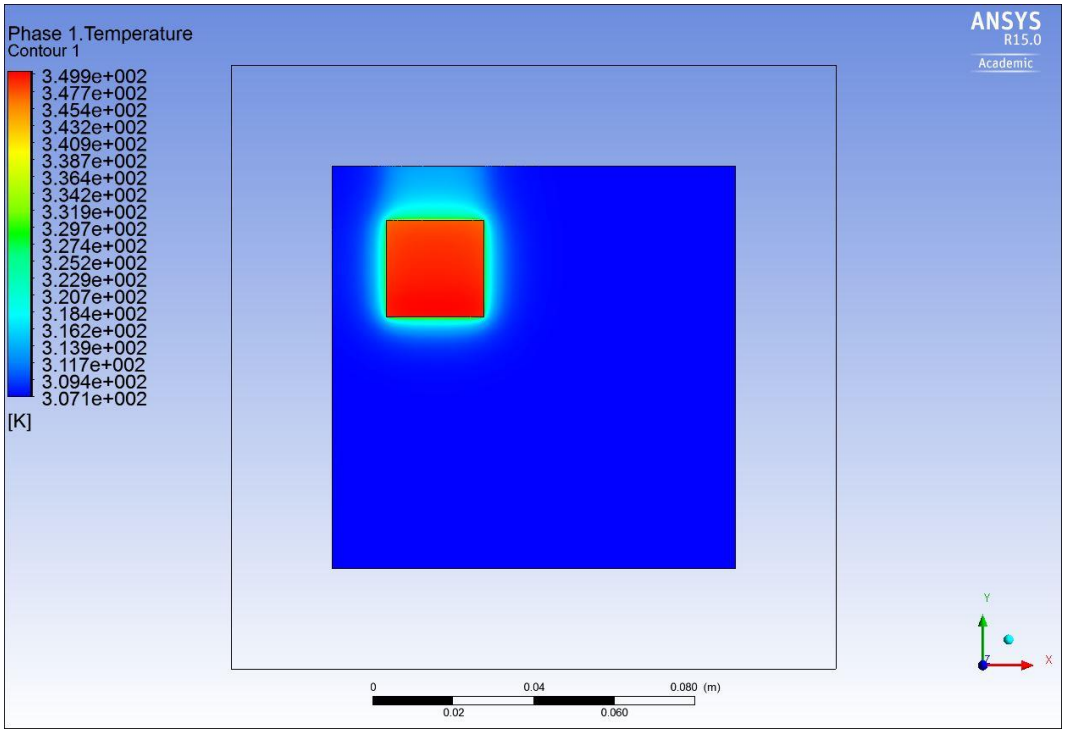

Figure 4.7: Temperature Contour for Case C at 9 W/cm^2

Figure 4.7 is representative of the uniform surface temperature contour seen in all numerical simulations at all the heat fluxes simulated. The combination of nucleation site density and bubble departure diameter functions used with Case C predicted the most reasonable vapor fractions while Case B tended to under predict the vapor generation. In the range of heat fluxes from 5 W/cm^2 to 11 W/cm^2, the vapor fractions varied from 2.3% to 23.9% for Case C. Figure 4.8a shows the vapor fraction contour on the die surface at 9 W/cm^2, the same heat flux as the previous figure.

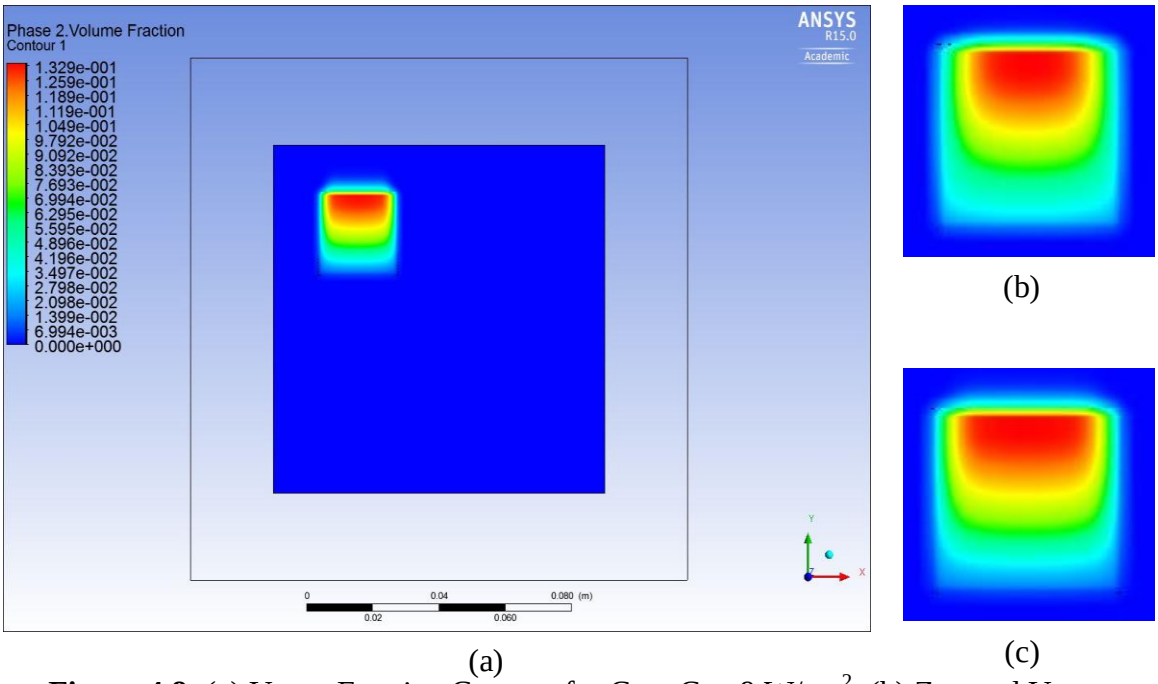

Figure 4.8: (a) Vapor Fraction Contour for Case C at 9 W/cm^2, (b) Zoomed Vapor Fraction Contour for 5 W/cm^2, (c) Zoomed Vapor Fraction Contour for 7 W/cm^2

When compared to lower heat fluxes, the region of maximum vapor fraction can be seen expanding as the heat flux increases. Also, the non-uniform nature of vapor generation in these simulations can be seen in Figure 4.8. At the minimum vertical die position, the vapor fraction is the lowest while at the maximum vertical die position, the vapor fraction is generally at the highest value. This is due to the fluid local to the die surface being

heated as it travels vertically across the die. Figure 4.9 shows the velocity vectors at a cut plane perpendicular to the die surface and in the middle of the heated die; Figure 4.9 is also for Case C at 9 W/cm^2.

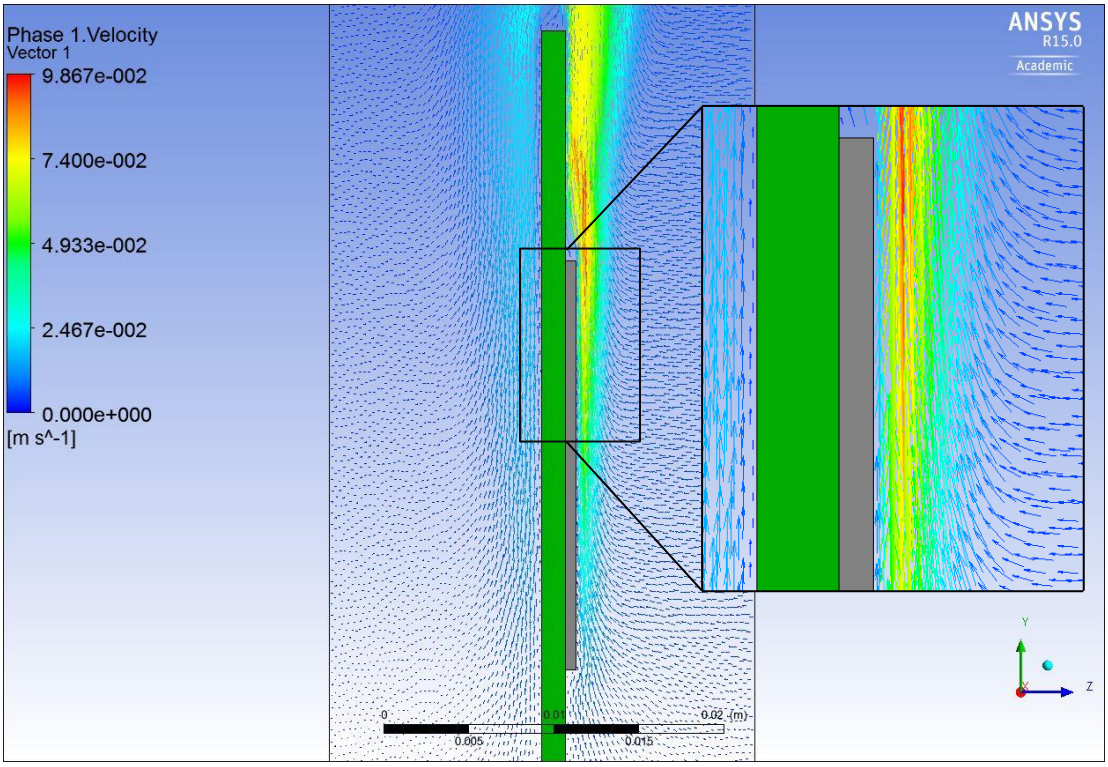

Figure 4.9: Velocity Vectors at a Perpendicular Cut Plane for Case C at 9 W/cm^2

In general, the majority of the fluid for pool boiling is stagnant with the exception of fluid near the heated surfaces as shown in Figure 4.9. Due to natural convection, the fluid approaches the lower edge of the die surface at relatively low velocities and is then heated by the die causing the fluid to accelerate. This energy transfer occurs across the surface of the die causing the fluid to continue accelerating as it travels vertically in the computational domain. The no slip condition can also be seen on the die and PCB surfaces, represented by velocity vectors with a magnitude of 0 m/s.

4.2.1.6 K-I NSD and K-I BDD (Case D)

For Case D, both bubble departure diameter and nucleation site density were modeled using the built-in K-I relationships from the previous cases while area of influence and frequency of bubble departure remained set to default. Numerical results for Case D are shown in Figure 4.10 along with experimental data; no numerical results for this combination of boiling parameters are available from Fincher.

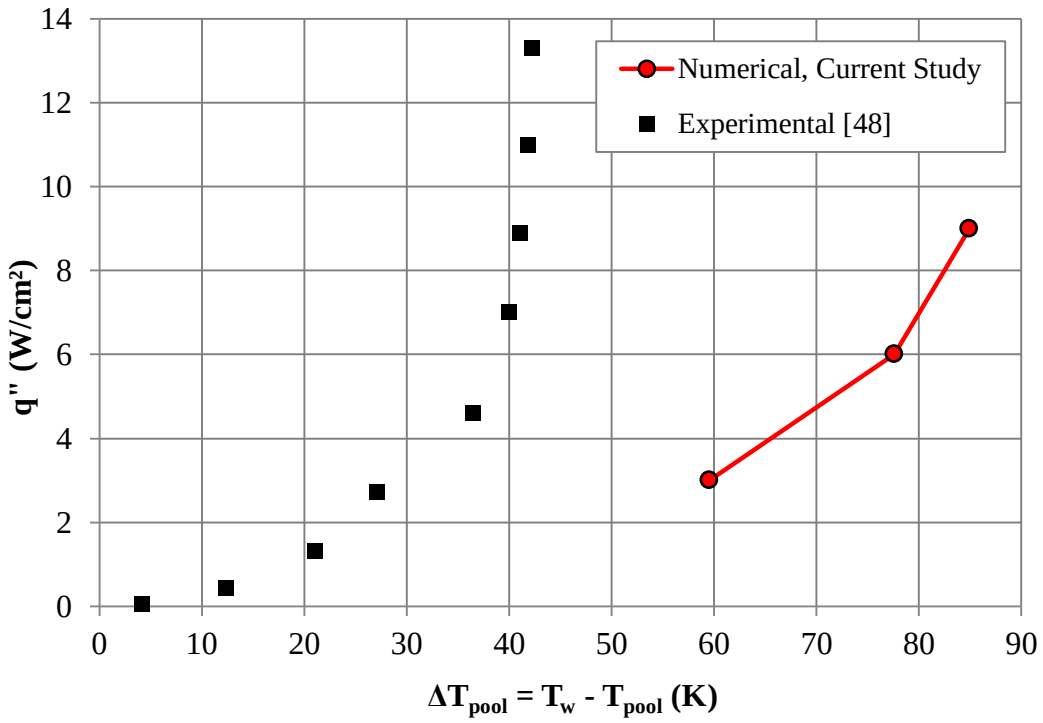

Figure 4.10: Single Die Heat Flux as a Function of Subcooled Temperature Difference with Respect to Maximum Die Temperature, Case D

Despite incorporating several fluid properties into nucleation site density and bubble departure diameter, Case D resulted in the worst agreement when compared to experimental data. The die surface temperature was over predicted by 40°C; more than double any of the previous cases. Also, vapor fraction was severely under predicted; at 6 W/cm^2, the maximum vapor fraction was less than 1%. The empirical functions used

were both developed by Kocamustafaogullari and Ishii, which performed adequately when used separately with other default empirical relationships; however, used together, they proved unsuitable for Novec 649.

There is another built-in bubble departure diameter function based on empirical data from Unal [30]; however, results using any combination of the Unal functions demonstrated poor agreement with experimental data similar to Case A. This inconsistency and lack of ability to predict which set of built-in functions will be suitable for dielectric fluids necessitate moving away from built-in functions and instead defining new relationships in the form of user-defined functions.

4.2.1.7 Variation of Nucleation Site Density Functions

Parametric studies on two of the boiling parameters, nucleation site density and bubble departure diameter, were performed by altering those functions while all other boiling parameters were kept as default. First, 12 different nucleation site density functions, split into two groups of six, were simulated; then, six bubble departure diameter functions were simulated. Each of the functions was based on the empirical relationships given by Eq. (4.11) or (4.12). For nucleation site density, the generic functional form is given by Eq. (4.19),

$$N_w = C_1(T_w - T_{sat})^{C_2} \tag{4.19}$$

where C_1 and C_2 are constants. A table summarizing all of the C_1 and C_2 values to recreate the nucleation site density functions used in this study is given in Appendix B.

In the case of nucleation site density, the functions were translated vertically to predict a higher or lower nucleation site density for a given temperature difference or the

slope was modified. Figures 4.11 and 4.12 show six nucleation site density functions, split into two groups where the "a" group maintains a constant leading coefficient while the "b" group maintains a constant exponent per Eq. (4.11) or (4.19).

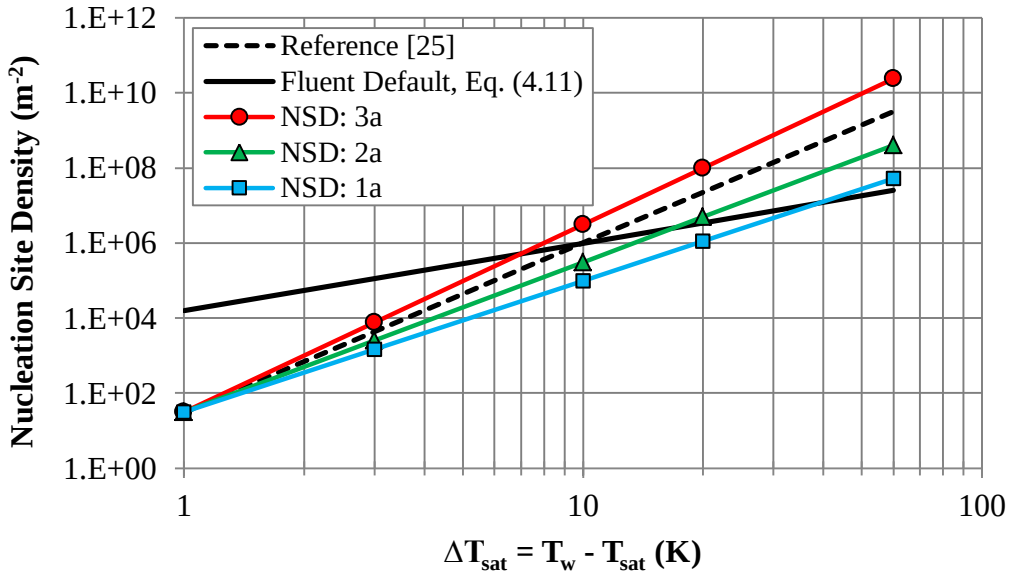

Figure 4.11: "a" Set of Nucleation Site Density Functions for Parametric Simulations

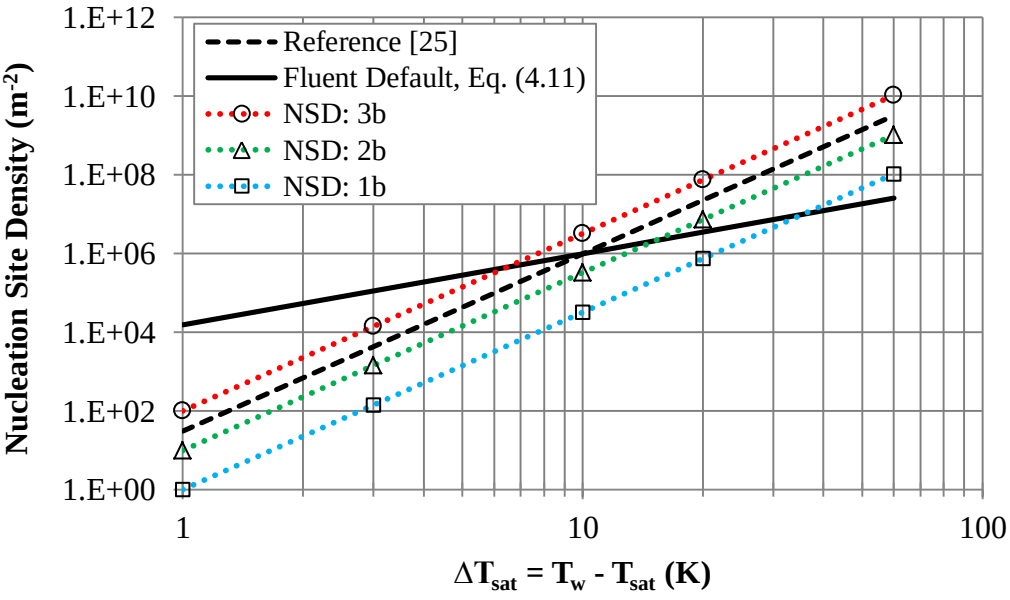

Figure 4.12: "b" Set of Nucleation Site Density Functions for Parametric Simulations

In addition to plotting the various user-defined functions, Figures 4.11 and 4.12 also plot two additional empirical functions. The curve denoted “Fluent Default” in the figures is the nucleation site density formulation implemented in ANSYS Fluent based on empirical data from Lemmert and Chawla [25] and given by Eq. (4.11); however, the built-in formulations do not match the function in the original reference. The curve denoted “Reference” is the unmodified nucleation site density as a function of wall superheat originally presented in [25]. The nucleation site density functions developed for this study have the same function form as Eq. (4.19).

Numerical results for heat flux versus temperature rise for the first six nucleation site density functions are plotted in Figure 4.13 and compared with the same set of experimental data used in the previous comparisons.

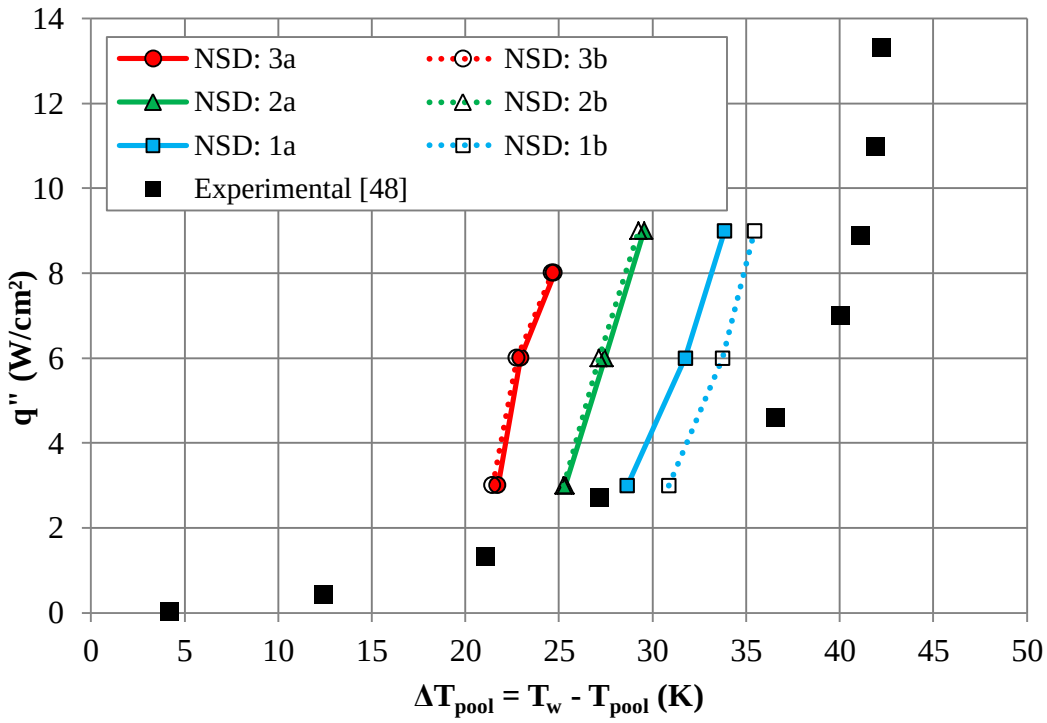

Figure 4.13: Single Die Heat Flux as a Function of Subcooled Temperature Difference; Numerical Results for Parametric Nucleation Site Density Functions, Set #1

Results were grouped based on the relative nucleation site densities predicted with a range of curves from concave to convex appearing. The six nucleation site density functions from Figures 4.11 and 4.12 are re-plotted together in Figure 4.14 to better illustrate the similarity between the "a" and "b" group of functions in the region of interest, i.e. wall superheat from 5°C to 25°C or ΔT_{pool} from 25°C to 40°C.

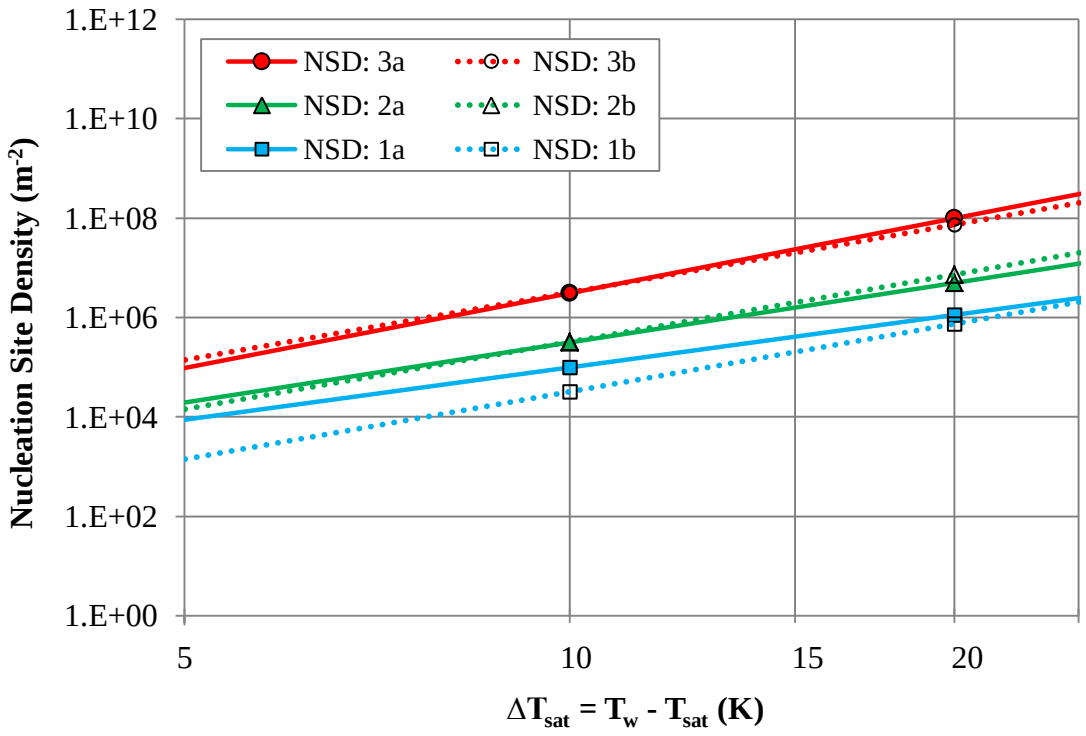

Figure 4.14: "a" and "b" Set of Nucleation Site Density Functions from Figures 4.11 and 4.12 for the Region of Interest: Wall Superheat from 5°C to 25°C

All the parametric functions along with the default, built-in functions seem to over predict the nucleation site density leading to an under predicted die surface temperature. A larger quantity of nucleation sites is indicative of more boiling heat transfer removing heat from the die surface thereby decreasing the surface temperature. The increasing slope of heat flux versus wall temperature was apparent in both the NSD: 1a and NSD: 1b

functions, which were the functions that predicted the lowest nucleation site densities in general and resulted in the best agreement with experimental data. The next set of nucleation site density functions is shown in Figures 4.15 and 4.16.

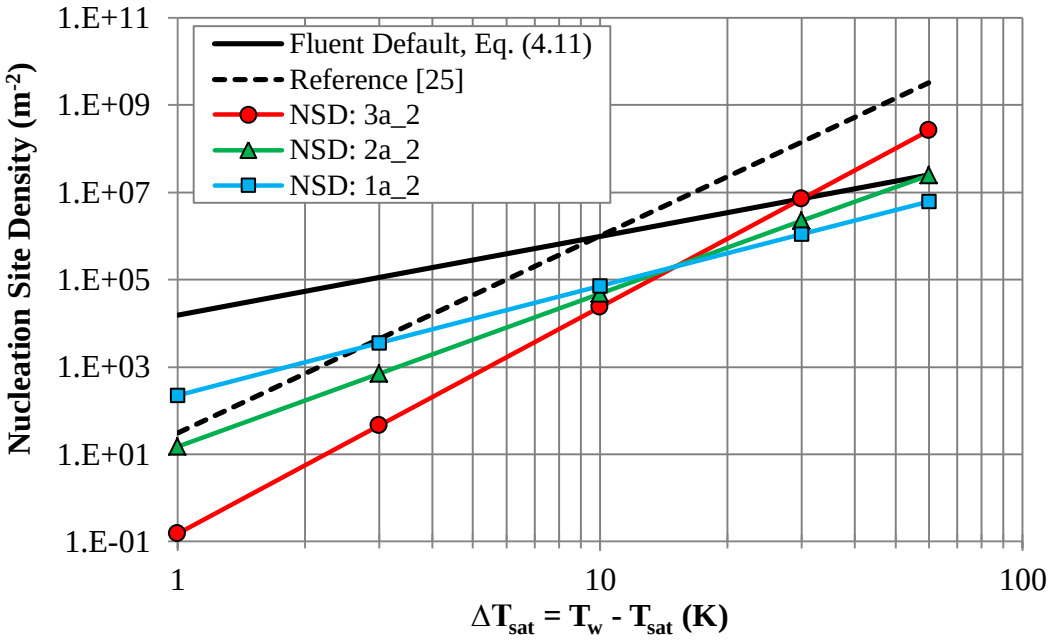

Figure 4.15: "a_2" Set of Nucleation Site Density Functions for Parametric Simulations

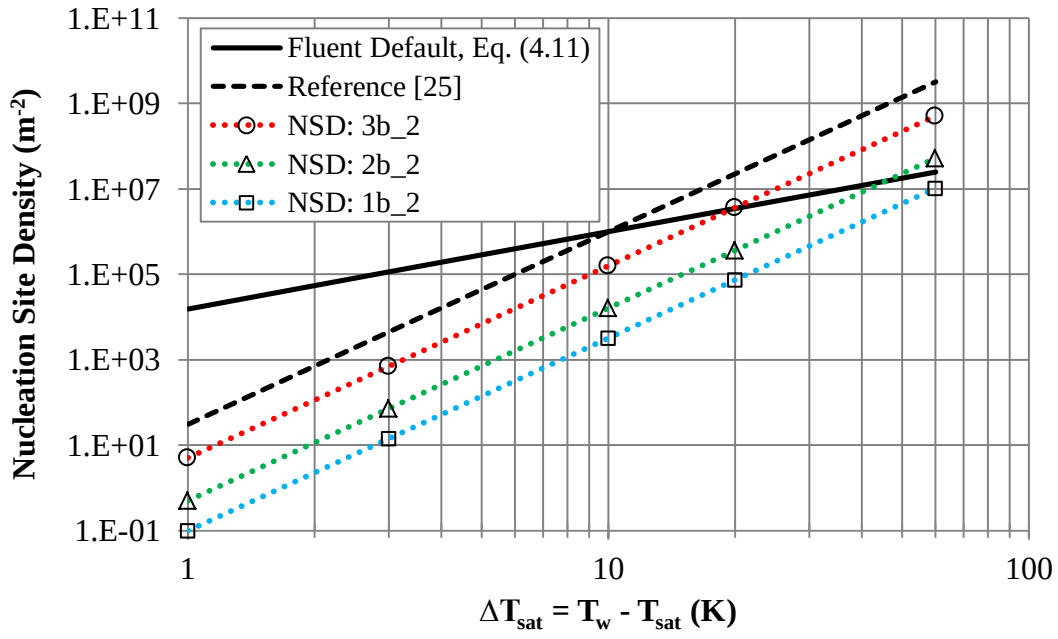

Figure 4.16: "b_2" Set of Nucleation Site Density Functions for Parametric Simulations

In the previous set, the functions were somewhat arbitrarily selected to establish general behavior and trends; however, the second set of nucleation site density functions applied knowledge learned from the previous set. One of the primary reasons the numerical results from the previous set did not demonstrate better agreement with experimental data is that many of those functions seemed to over predict the nucleation site density as the built-in function did. In addition to focusing more on the temperature difference region of interest, the second set of functions universally predicted fewer active nucleation sites.

Numerical results for the second set of nucleation site density functions are plotted in Figure 4.17 along with experimental data. The other three boiling parameters were set to default.

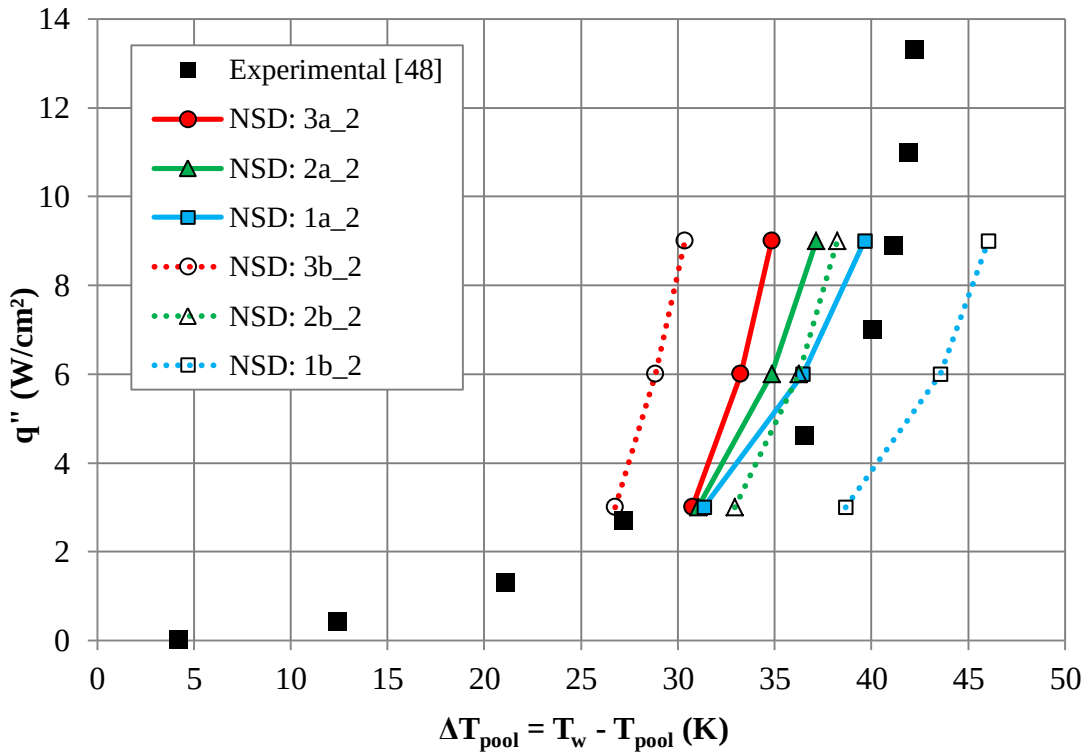

Figure 4.17: Single Die Heat Flux as a Function of Subcooled Temperature Difference; Numerical Results for Parametric Nucleation Site Density Functions, Set #2

All six functions demonstrated the increasing slope of heat flux versus wall temperature. A broader range of nucleation site densities were predicted as NSD: 3b_2 under predicted the die temperature while NSD: 1b_2 over predicted the die temperature suggesting too many nucleation sites were predicted for the former and too few sites were predicted for the latter. The best agreement with experimental data was seen with NSD: 1a_2 that predicted die surface temperatures within 2°C.

Nucleation site density is only one of the four available boiling parameters that can be modified and experimental measurements of active nucleation sites can be challenging to obtain. On the other hand, a similar parametric study was performed on bubble departure diameter and experimental data for 0°C and 15°C subcooled FC-72 is available from Sridhar, et al. [19].

4.2.1.8 Variation of Bubble Departure Diameter Functions

The default bubble departure diameter function in ANSYS Fluent is based on empirical work by Tolubinski and Kostanchuk [26]; however, as with nucleation site density, the implemented function in ANSYS Fluent does not match the original reference. The six functions for bubble departure diameter are plotted in Figures 4.18 and 4.19 as a function of degree of subcooling or the temperature difference between the saturation and the bulk pool temperatures. The generic functional form for the bubble departure diameter is given by Eq. (4.20),

$$D_W = (C_3)e^{-C_4(T_{sat}-T_{pool})} \tag{4.20}$$

where C_3 and C_4 are constants. A table summarizing the C_3 and C_4 values to recreate the bubble departure diameter functions used in this study is available in Appendix B.

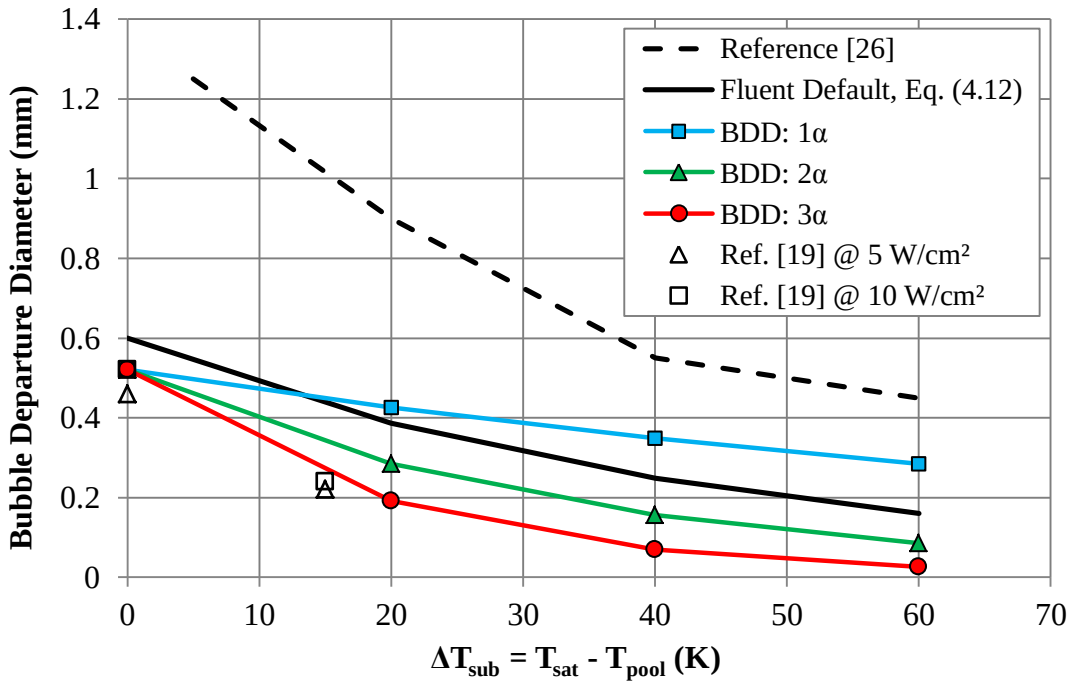

Figure 4.18: "α" Set of Bubble Departure Diameter Functions for Parametric Simulations

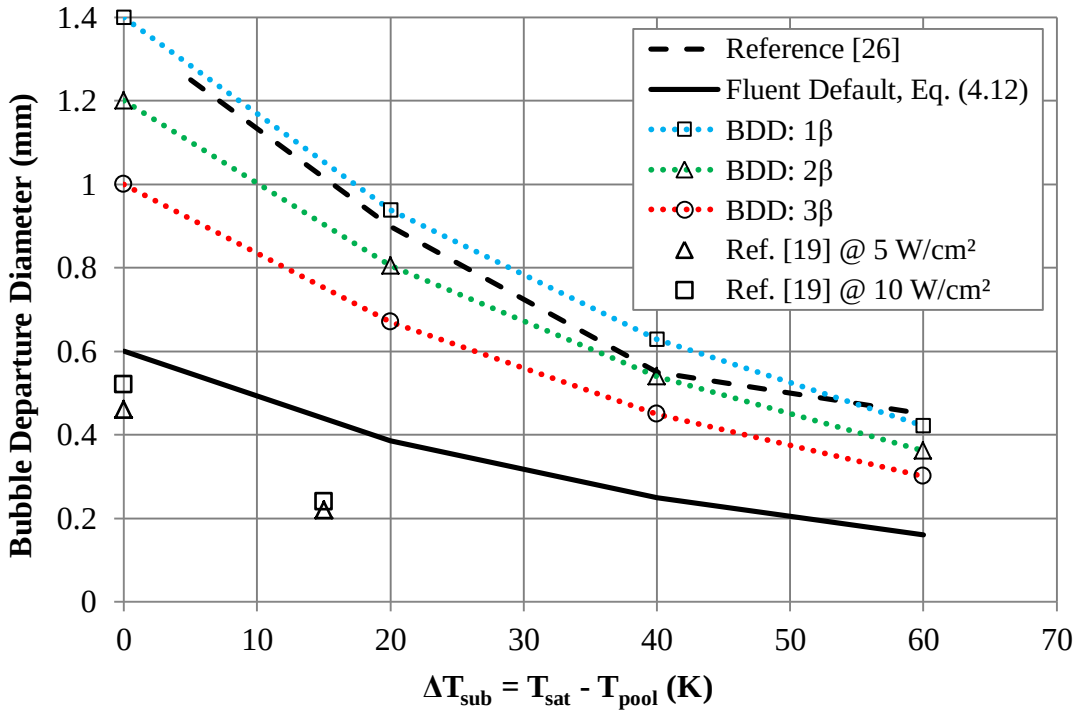

Figure 4.19: "β" Set of Bubble Departure Diameter Functions for Parametric Simulations

The parametric functions for bubble departure diameter were separated into two groups, α and β, where each group of functions was centered about the unmodified empirical relationship or the default implementation in ANSYS Fluent, resulting in the β-functions predicting larger bubble departure diameters compared to the α-functions. Also included in the figures are the original empirical relationship, denoted "Reference," and the modified function implemented in ANSYS Fluent, denoted "Fluent Default" which was given previously by Eq. (4.12). Unlike the nucleation site density, experimental data for bubble departure diameter in a pool of FC-72 is available from Sridhar, et al. [19] for two levels of subcooling and two heat fluxes. These experimental results are also included in Figures 4.18 and 4.19.

The experimental model used by Sridhar, et al. [19] was a five die configuration arranged in a cross pattern with FC-72 as the working fluid. Despite having different chemical compositions, FC-72 and Novec 649 have demonstrated similar behavior in immersion cooling scenarios with a similar geometry and range of heat fluxes used in this study [13, 49]. The thermophysical properties of FC-72 are sufficiently similar to Novec 649 that bubble departure diameters are expected to be similar as well, especially compared to water. Sridhar, et al. collected experimental data for bubble departure diameter at 15°C subcooled for heat fluxes up to 10 W/cm^2; for more information on the experimental setup or results, see the study by Sridhar, et al. [19].

Numerical results for heat flux as a function of temperature rise for the six bubble departure diameter functions are plotted in Figure 4.20 along with experimental data. It should be noted that the area of influence and frequency of bubble departure were set to their respective default functions while nucleation site density was set to NSD: 1b from

the previous section. The numerical results were separated into two groups based on α and β. All of the α-functions predicted smaller bubble departure diameters that are more representative of experimental data [19] compared to the β-functions that tended to predict bubble departure diameters up to four times larger than experimental data at 15°C subcooling.

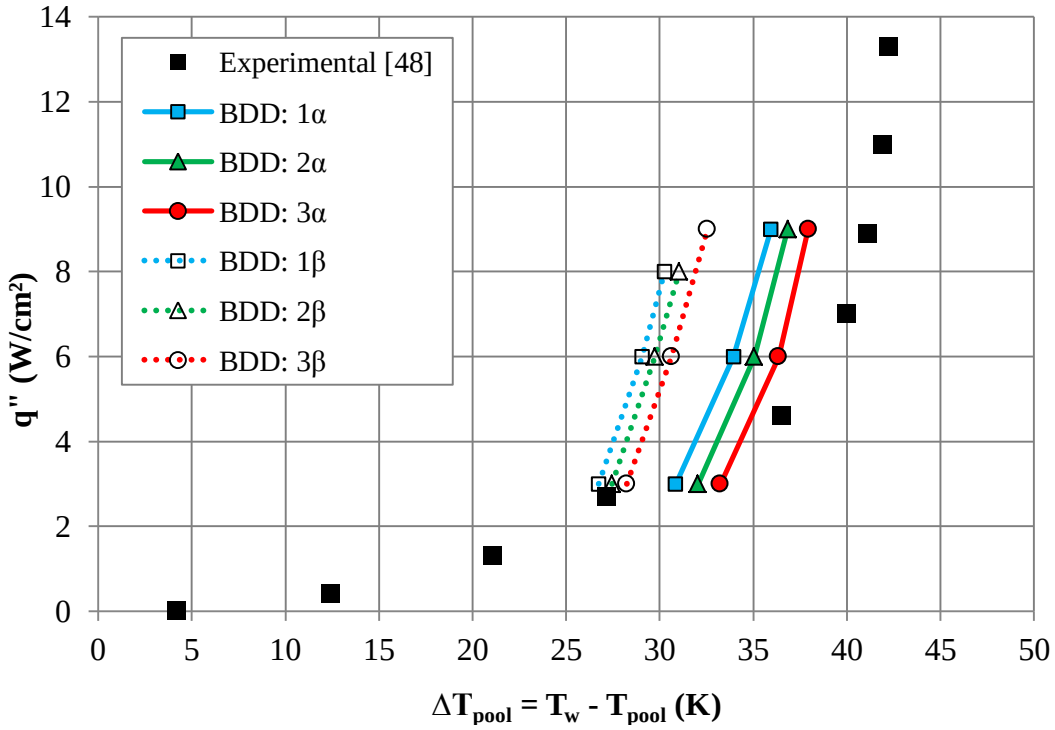

Figure 4.20: Single Die Heat Flux as a Function of Subcooled Temperature Difference; Numerical Results for Parametric Bubble Departure Diameter Functions, NSD: 1b

Decreasing the bubble departure diameter led to a positive, or rightward shift, in the boiling curve as higher die surface temperatures were predicted. In the RPI and Non-Equilibrium boiling models, the total surface heat flux is divided into three or five terms, one of which is a quenching heat flux. With smaller vapor bubbles departing the surface, there is less volume near the surface for subcooled liquid at a lower temperature to enter the volume left by the departing bubble. This results in less boiling heat transfer and

higher surface temperatures. In general, different values for bubble departure diameter result in a positive or negative translation to the boiling curve. The best agreement with experimental data from this set of parametric trials was seen with BDD: 3α (most representative of Sridhar, et al [19]), NSD: 1b and area of influence and frequency of bubble departure set to the default functions given by Eq. (4.7) and (4.10), respectively; die surface temperatures were within 3°C of experimental data.

A table summarizing the constants C_3 and C_4 to recreate the bubble departure diameter functions using Eq. (4.20) can be found in Appendix B. With general trends established for nucleation site density and bubble departure diameter using various functions, the next set of numerical simulations applied combinations of the previous functions to achieve the best agreement with experimental data. Functions most representative of experimental data for boiling parameters were used when possible.

4.2.1.9 Combination of NSD and BDD Functions

Experimental data for bubble departure diameter was available and functions, in particular BDD: 3α, have shown adequate capability in replicating the increasing slope of heat flux versus wall temperature as well as reasonably predicting the die surface temperature. Two of the previous parametric nucleation site density functions, NSD: 1a_2 and NSD: 2a_2, were used in combination with this bubble departure diameter function. These nucleation site density functions were chosen because on their own, with all other boiling parameters set to default, they also demonstrated reasonable agreement with experimental data and appropriate boiling curve slopes. Numerical results for these two combinations of nucleation site density and bubble departure diameter functions are shown in Figure 4.21 along with experimental data. Also included in the figure is Case C,

which was the best agreement with experimental data when using only the built-in relationships provided by ANSYS Fluent. Case C used the default formulation for bubble departure diameter and the K-I model for nucleation site density, given by Eq. (4.12) and (4.15), respectively.

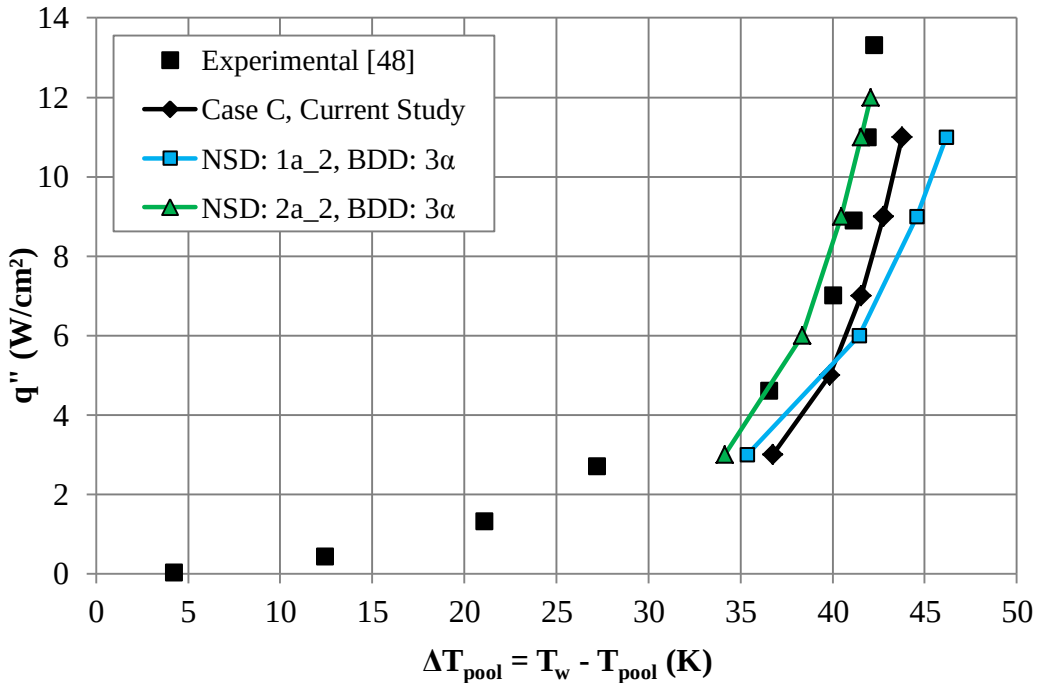

Figure 4.21: Single Die Heat Flux as a Function of Subcooled Temperature Difference; Numerical Results for Combinations of Nucleation Site Density and Bubble Departure Diameter

From the previous parametric trials, it was determined that modifying the bubble departure diameter only resulted in a positive or negative shift to the die surface temperature with no effect on the slope of the boiling curve. This is again seen with the numerical results in Figure 4.21; applying a function that predicts a smaller bubble departure diameter results in a higher surface temperature due to less quenching heat transfer as mentioned previously. From the nucleation site density parametric trials, NSD: 1a_2 demonstrated better agreement with experimental data compared to NSD: 2a_2

when the bubble departure diameter function was set to default. However, applying the experimental data from Sridhar, et al. [19] in the form of BDD: 3α resulted in NSD: 1a_2 over predicting the die surface temperature by a maximum of 4°C while NSD: 2a_2 was within 1°C for heat fluxes in the region where nucleate boiling was well established. The user-defined functions demonstrated better agreement than Case C, the best combination of built-in functions.

With parametric trials for nucleation site density and bubble departure diameter completed, the three major heat fluxes comprising the RPI and Non-Equilibrium boiling models (convective, quenching and evaporative) were examined in more detail. The equations for convective, quenching and evaporative heat flux were given by Eqn. (4.2), (4.3) and (4.4), respectively. To close the heat flux equations, four boiling parameters (area of influence, frequency of bubble departure, nucleation site density and bubble departure diameter), given by Eq. (4.7) through (4.12), needed to be specified. To determine the dependence of the heat fluxes on the degree of subcooling and bubble departure diameter, every other term in the heat flux and boiling parameter equations was kept constant. Liquid and vapor properties for Novec 649 from Appendix A were used when possible. The nucleation site density, N_w, was set to 1×10^6 m^{-2} while the single phase heat transfer coefficient, h, was set to 1000 W/m^{2}K; the former was within the nucleation site density region of interest and the latter was approximated by taking the results of a converged solution at 3 W/cm^2 and dividing the predicted temperature difference between the die surface and pool by the imposed heat flux.

The relative contribution of each heat flux to the total wall heat flux as a function of the fractional change to the degree of subcooling and bubble departure diameter are

plotted in Figures 4.22 and 4.23. The y-axis is a nondimensionalized heat flux found by dividing the component heat flux by the total heat flux at baseline, where the total heat flux was a constant equal to the sum of the convective, quenching and evaporative heat fluxes evaluated at a baseline bubble departure diameter.

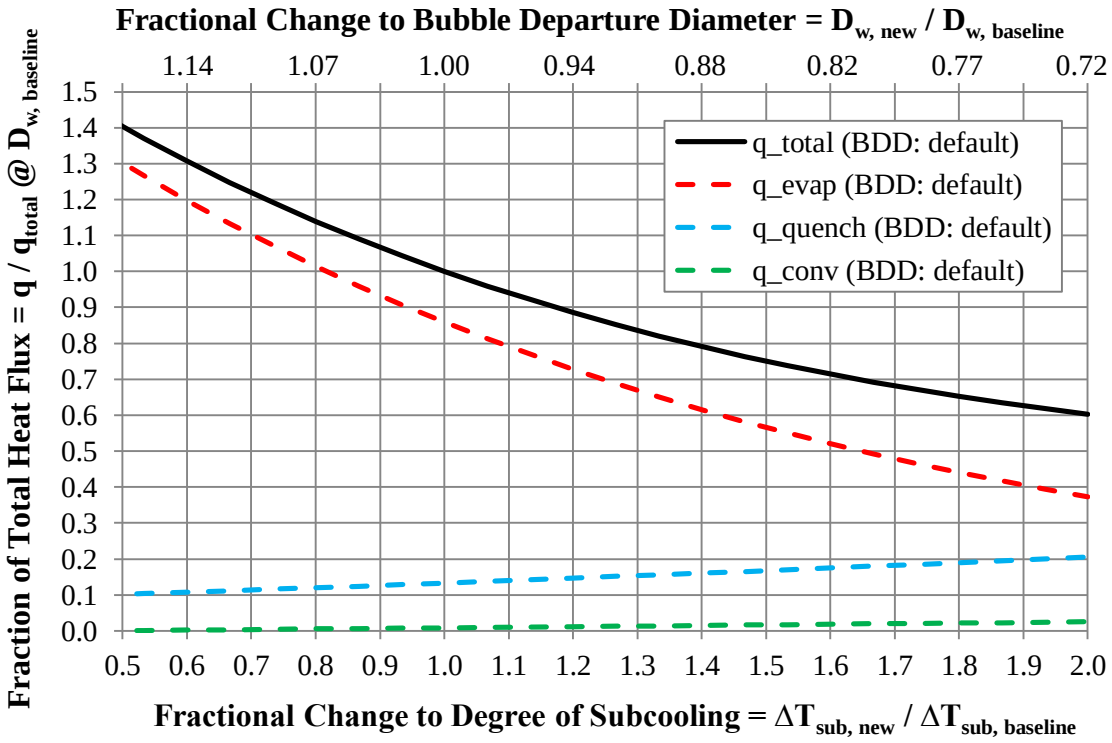

Figure 4.22: Fraction of Total Heat Flux as a Function of Fractional Change to Degree of Subcooling and BDD using BDD: Default

In both Figure 4.22 and 4.23, the baseline bubble departure diameter, $D_{w,baseline}$, is 0.00025 m and the baseline degree of subcooling, $\Delta T_{sub,baseline}$, is 15°C. When the BDD: 3α function is evaluated at 15°C subcooling, the resulting bubble departure diameter is approximately 0.00025 meters, which is why it was chosen as the baseline value. Each plot contains two nondimensionalized x-axes for the fractional change to

bubble departure diameter (top) and the fractional change to the degree of subcooling (bottom) based on the respective baseline values. An x-axis value of 0.5 on either axis is indicative of halving the bubble departure diameter or the degree of subcooling. The difference between Figure 4.22 and 4.23 was the bubble departure diameter function used; in Figure 4.22, the default function provided by ANSYS Fluent given by Eq. (4.12) was used while in Figure 4.23, the BDD: 3α function based on experimental data from Sridhar, et al. [19] was used.

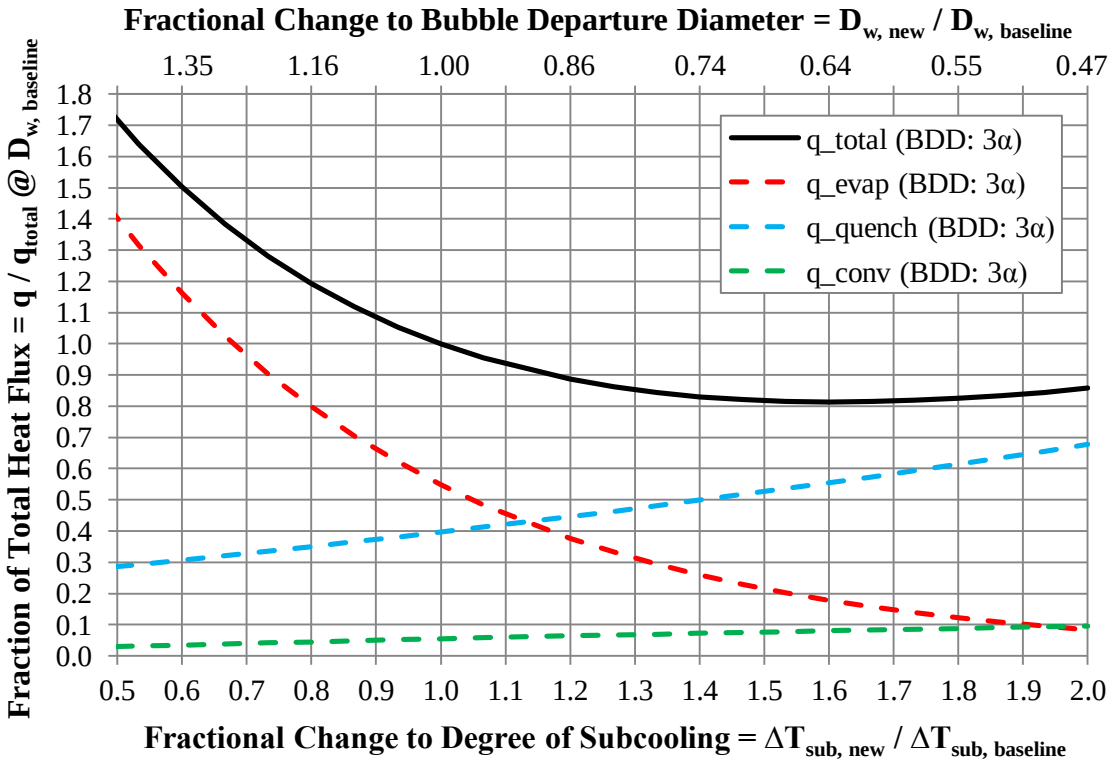

Figure 4.23: Fraction of Total Heat Flux as a Function of Fractional Change to Degree of Subcooling and BDD using BDD: 3α

Bubble departure diameter and degree of subcooling have an inverse relationship; as the degree of subcooling increases, the liquid pool is at a lower temperature, which can

reduce the bubble departure diameter. The heat flux trends were similar in both Figure 4.22 and 4.23; the quenching and convective heat fluxes increased as the degree of subcooling increased (or the bubble departure diameter decreased). For the convective heat flux, the lower pool temperature from increased subcooling results in a larger temperature gradient and more single phase heat transfer. Similarly for the quenching heat flux, as the subcooling increases, the temperature of the liquid that fills the void left by departing bubbles is lower suggesting an increase in heat transfer.

Regardless whether the bubble departure diameter was evaluated using the default or BDD: 3α function, the convective heat flux was a relatively small fraction of the total baseline heat flux, typically less than 10%. The convective heat flux is dependent on the single phase heat transfer coefficient, which was set to 1000 W/m^2K; the exact function used by ANSYS Fluent for the single phase heat transfer coefficient has not been found in explicit detail. Experimental results for immersion-cooled heat sinks in FC-72 from Bhavnani, et al. [51] suggested that the latent (or evaporative) heat flux is a minor component of the total heat flux and is typically less than 16%. In a theoretical study involving several refrigerants, FC-72 and water, Tong, et al. [52] also found that the evaporative heat flux was a relatively minor heat transfer mechanism. The evaporative heat flux when using the default bubble departure diameter function (Fig. 4.22) is a significantly larger percentage of the total heat flux compared to the evaporative heat flux when using the BDD: 3α function (Fig. 4.23). The user-defined function BDD: 3α not only captures experimental data for bubble departure diameter from Sridhar, et al. [19] more representatively but also predicts an evaporative heat flux more in line with those seen by Bhavnani, et al. [51] and Tong, et al. [52].

The agreement between numerical simulations and experimental data has been improved by relying less on the water-based empirical functions for boiling properties and using experimental data corresponding to dielectric fluids when available. While the user-defined functions for nucleation site density used heretofore deviated from the built-in functions provided by ANSYS Fluent, they were still confined to the same functional form as the built-in functions and that of the empirical results by Lemmert and Chawla [25]. However, the set of simulation results in the next section moved away from the functional form given by Eq. (4.19) and explored a piecewise or nonlinear functional form for nucleation site density. This change to the functional form was motivated by the slope of the boiling curve. Some user-defined functions resulted in good agreement with experimental data at lower heat fluxes when the boiling curve was less steep and poor agreement when the boiling curve was steeper at higher heat fluxes. The opposite can be said of other user-defined functions; therefore, using a piecewise definition for boiling parameters, in particular the nucleation site density, can better capture the boiling curve behavior.

4.2.1.10 Piecewise Nonlinear Nucleation Site Density Functions

User-defined functions for nucleation site density and bubble departure diameter have resulted in good agreement with experimental data. By moving away from built-in functions for the boiling parameters, multiphase simulations can be tailored more specifically to the experimental setup by relying less on empirical data that may or may not be related to the current study. For example, the user-defined functions for bubble departure diameter were based on experimental results directly related to the multiphase

simulations because the bubble departure diameters were found for a similar fluid and geometry.

While the nucleation site density functions used previously deviated from the built-in functions, they were still limited to the same equation form as the built-in functions, which resulted in a linear relationship between nucleation site density and wall superheat when plotted on a log-log plot. In this section, a piecewise nonlinear function is explored based on two nucleation site density functions that transition in the temperature region of interest. The piecewise nonlinear function is given by Eq. (4.21),

$$N_w = \begin{cases} (225)(T_w - T_{sat})^{2.5} & (T_w - T_{sat}) < 25°C \\ (6.7 \times 10^{-6})(T_w - T_{sat})^{7.885} & (T_w - T_{sat}) \geq 25°C \end{cases} \quad (4.21)$$

where both nucleation site density functions share the same form given by Eq. (4.19) and the resulting nucleation site density is in m^{-2} when the wall and saturation temperatures, T_w and T_{sat}, respectively are in units of °C or K. The first function given in Eq. (4.21) was previously used in the nucleation site density parametric trials and was denoted NSD: 1a_2 while the second function was chosen due to its more rapid slope change. Figure 4.24 plots the piecewise nonlinear nucleation site density function as its component functions (NSD: 1a_2 and NSD: 1c) along with the "Fluent Default" and "Reference" functions. For the piecewise nonlinear nucleation site density function, the transition from NSD: 1a_2 to NSD: 1c occurs at a wall superheat of 25°C, which is equivalent to a ΔT_{pool} of 40°C when the degree of subcooling is 15°C. This transition point was selected because it falls within the temperature region of interest for the experimental data.

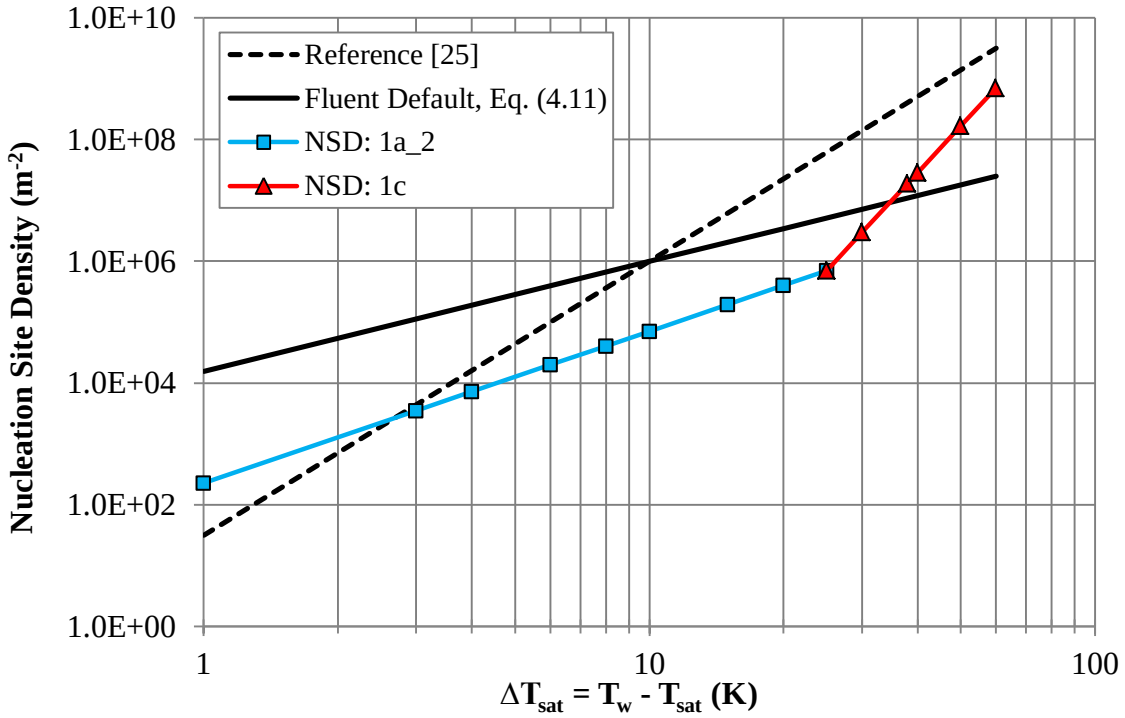

Figure 4.24: Piecewise Nonlinear Nucleation Site Density Function, NSD: Nonlinear_1c, with Component Functions Plotted as NSD: 1a_2 and NSD: 1c

In previous numerical simulations, the steeper slope of the boiling curve at higher heat fluxes was not always captured when using nucleation site density functions based on the same equation form as the built-in functions. Therefore, a more rapid increase to the nucleation site density as a function of wall superheat (NSD: 1c) was chosen and coupled with a previously used NSD function that demonstrated good agreement with experimental data. Numerical results for heat flux versus temperature rise for three combinations of nucleation site density (NSD) and bubble departure diameter (BDD) are plotted in Figure 4.25, where "NSD: nonlinear_1c" is Eq. (4.21). In Figure 4.25, a total of three boiling curves are plotted and compared with experimental data. Of the three numerical results, two utilize the piecewise nonlinear nucleation site density function given by Eq. (4.21) while the third set of numerical results is repeated from the previous

section and utilizes the NSD: 1a_2 function, which is one of the component functions for the piecewise nonlinear NSD equation. The bubble departure diameter was set to the default, built-in function or BDD: 3α, where the latter is the most representative of experimental data from Sridhar, et al. [19].

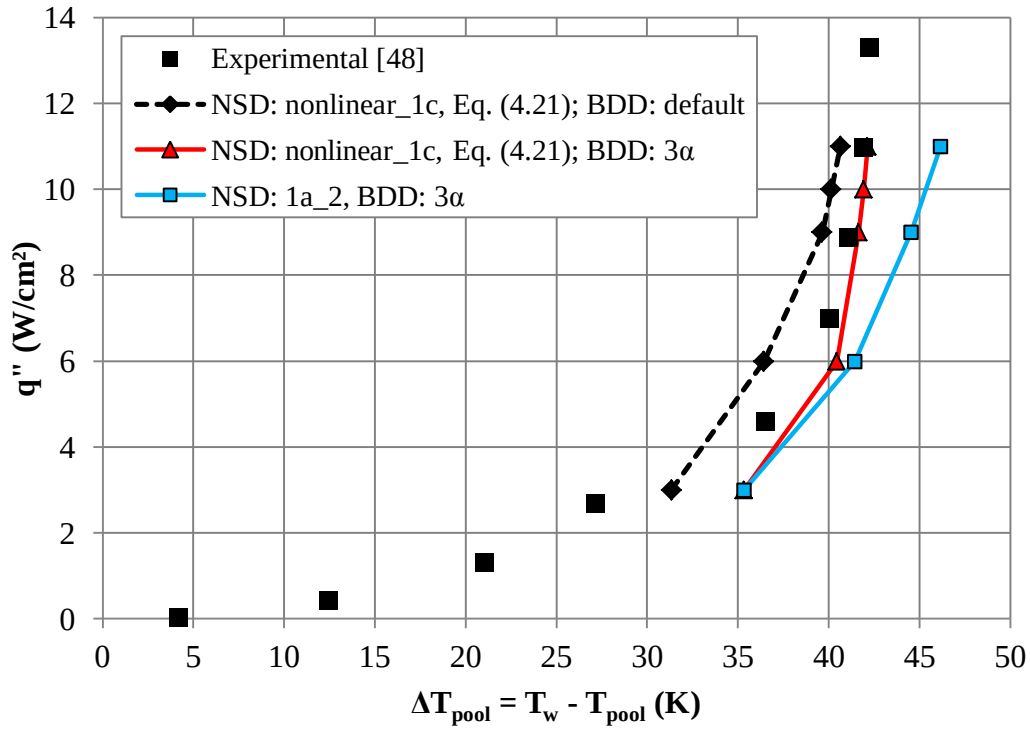

Figure 4.25: Single Die Heat Flux as a Function of Subcooled Temperature Difference; Numerical Results for Combinations of Nucleation Site Density and Bubble Departure Diameter using Piecewise Nonlinear NSD Function

Comparing the numerical results with the same bubble departure diameter function (BDD: 3α) and different nucleation site density functions (NSD: nonlinear_1c and NSD: 1a_2), the predicted die temperature should be the same prior to the transition point at a wall superheat of 15°C or ΔT_{pool} of 40°C because the NSD functions are the same prior to the transition point. For the heat fluxes simulated, 3 W/cm^2 resulted in the

same predicted die temperature while heat fluxes at 6 W/cm^2 and beyond resulted in different die temperatures due to the piecewise nonlinear NSD function applying the second equation, which predicts a more rapidly increasing nucleation site density versus wall superheat. Compared to the linear form, the nucleation site density function, NSD: nonlinear_1c, Eq. (4.21), is able to better capture the boiling curve from experimental data by predicting a steeper increase in die temperature as heat flux increases; these two curves are plotted with a dashed black and solid red line in Figure 4.25.

Comparing the numerical results with different bubble departure diameter functions (BDD: default and BDD: 3α) and the same nucleation site density function (NSD: nonlinear_1c), a positive shift in the die temperatures was seen when the bubble departure diameter function was modified from BDD: default to BDD: 3α and this was consistent with observations from the bubble departure diameter parametric trials. From Figure 4.18, the "Fluent Default" BDD function predicts a larger bubble departure diameter than BDD: 3α, which leads to a larger volume near the surface for lower temperature fluid to fill when the vapor bubble departs the surface allowing more quenching heat transfer and a lower die surface temperature.

This concludes the exploration of piecewise nonlinear nucleation site density functions in multiphase simulations. It is acknowledged that some previous combinations of user-defined functions, in particular NSD: 2a_2 and BDD: 3α shown in Figure 4.21, have demonstrated as good or better agreement with experimental data using a relatively simple equation form. However, the piecewise nonlinear function used in this section only consisted of two equations and by further increasing the number of equations, the boiling curve from experimental data could be matched to an ever-increasing degree of

agreement. The code used to implement these user-defined functions in ANSYS Fluent is given in Appendix C. For all numerical simulations performed up to and including this section, the degree of subcooling was fixed at 15°C. In the next section, numerical results for two other levels of subcooling will be discussed.

4.2.1.11 Variation of Degree of Subcooling

With general trends established for the behavior of nucleation site density and bubble departure diameter functions, the remaining pool boiling sections will explore other simulation parameters, such as the degree of subcooling or turbulence model, while continuing to apply user-defined functions in place of built-in functions. In this section, two additional levels of subcooling are simulated; these include 13°C and 18°C in addition to the previously simulated 15°C. For these numerical simulations, the setup and models used remained the same; however, the bulk liquid temperature was initialized to a different value based on the level of subcooling. For the boiling parameters, area of influence and frequency of bubble departure were set to the default models given by Eq. (4.7) and (4.10), respectively, while the nucleation site density was set to the nonlinear user-defined function, NSD: nonlinear_1c, given by Eq. (4.21), and the bubble departure diameter was set to BDD: 3α. Numerical results are plotted in Figure 4.26 along with experimental data, which was at 15°C. The multiphase numerical results (the die temperatures predicted at 3 W/cm^2 and above) demonstrate several odd characteristics and appear contrary to physical expectations. For example, a pool of Novec 649 subcooled 13°C below saturation is at a higher liquid temperature than a pool of Novec 649 subcooled 18°C below saturation; the bulk liquid temperatures are 36°C and 31°C, respectively. However, the multiphase numerical results in Figure 4.26 imply that a

higher bulk liquid pool temperature (13°C subcooled) would result in a lower die surface temperature than a lower bulk liquid pool temperature (18°C subcooled); this is contrary to physical expectations.

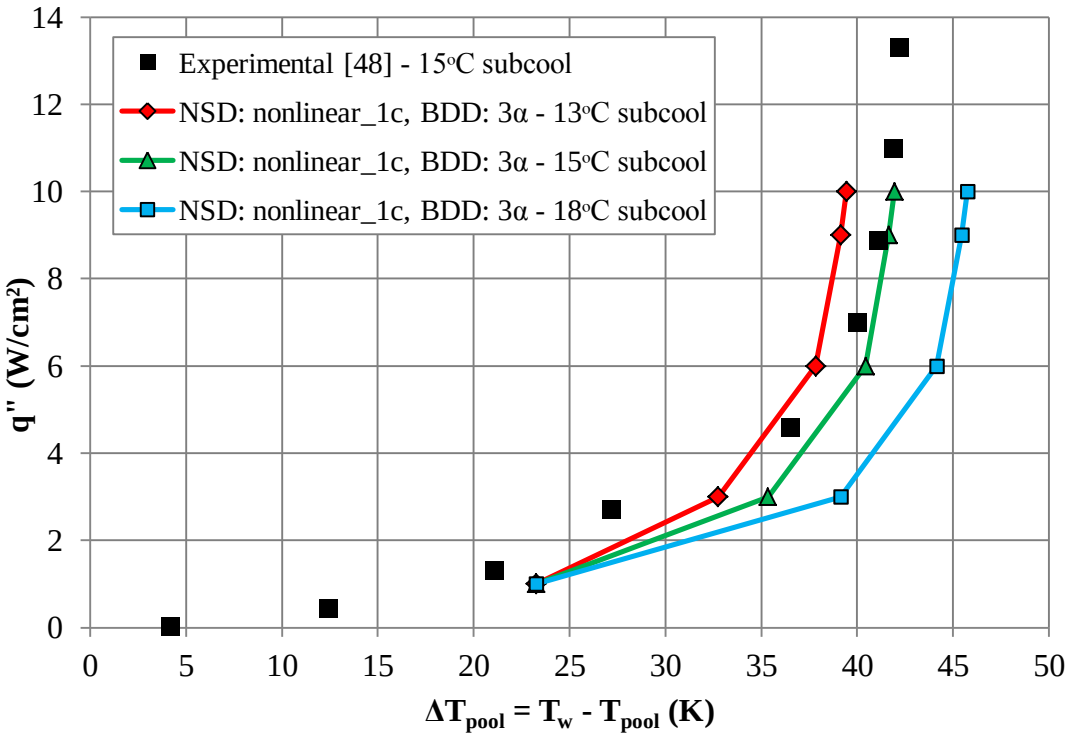

Figure 4.26: Single Die Heat Flux as a Function of Subcooled Temperature Difference; Numerical Results for Various Levels of Subcooling

In general, only heat fluxes sufficiently high enough to establish nucleate boiling were simulated; however, numerical results for 1 W/cm^2 were also included in Figure 4.26 for a single phase situation with no vapor generation to determine if the trends were due to boiling parameters or the numerical model. In the single phase regime, the level of subcooling had no impact on the die temperature as the predicted die temperatures converged to a single point at 1 W/cm^2. Although the bubble departure diameter function used (BDD: 3α) was based on experimental data from Sridhar, et al. [19], the bubble

departure diameter model implemented in ANSYS Fluent was a function of degree of subcooling only. In pool boiling experiments at 9 and 15 W/cm^2, Henry and Kim [53] found an increase in die temperatures as the subcooling level increased and attributed this to a decreased bubble departure frequency that reduced the overall heat transfer. In another experiment using silicon surfaces (bare and coated in carbon nanotubes), Sathyamurthi, et al. [54] saw an increase in die temperatures as the subcooling increased from 5°C to 30°C at 9 and 11 W/cm^2. While the behavior of the numerical results in Figure 4.26 may not be entirely implausible, the boiling parameters, their interactions and the Non-Equilibrium boiling model in ANSYS Fluent should be explored further. The next section presents the last set of numerical results for pool boiling.

4.2.1.12 Variation of Turbulence Model

In this section, the numerical results using other turbulence models are presented to determine if the viscous model chosen had any significant impact on the predicted die temperatures. For all previous simulations, the two-equation turbulent model k-ε RNG was employed. k-ε RNG is the recommended turbulent model to account for smaller scales of motion, such as the vapor bubble dynamics in the boundary layer near the wall [20]. There are two other k-ε turbulent models available in ANSYS Fluent along with other models, such as k-ω; however, per the study by Fincher [13], it was determined the k-ε RNG model provided a balance between complexity and computational costs. Numerical results using the standard k-ε and standard k-ω turbulent models are shown in Figure 4.27 with experimental data. All the turbulent models were applied to the same single die multiphase numerical model shown in Figure 4.2 with the same set of boiling parameters and simulated over the same range of heat fluxes.

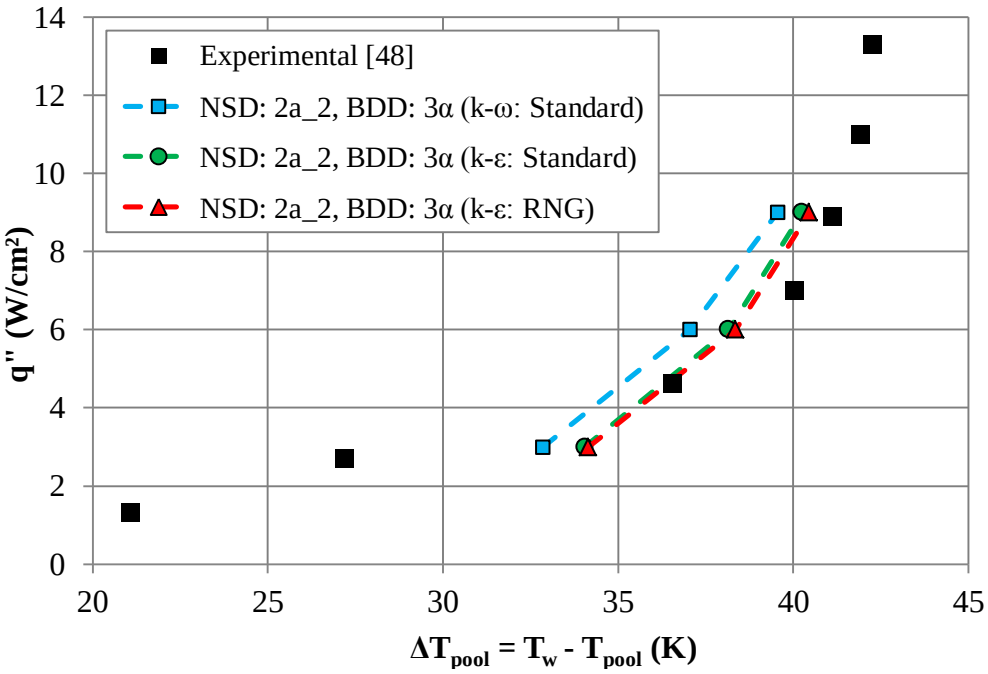

Figure 4.27: Single Die Heat Flux as a Function of Subcooled Temperature Difference; Numerical Results for Various Turbulence Models

The predicted die surface temperatures of the alternative models were within 1.2°C of those predicted by the k-ε RNG model. The largest temperature differences occurred between distant families of turbulent models, i.e. k-ε vs. k-ω, with negligible temperature differences being predicted by the standard and RNG k-ε turbulent models. This concludes the discussion of pool boiling simulations using a single die numerical model submerged in a pool of Novec 649. Flow boiling results using a four die cartridge model are presented in the next section.

4.3 Flow Boiling Simulations

In this section, the numerical results for flow boiling of four die in a small form factor, cartridge module designed by Gess [35, 50] will be presented and discussed. The model is described first followed by the results, which are compared with experimental

data and similar numerical results from Fincher [13] when available. The numerical results presented first explore the ability of built-in boiling parameters to adequately predict the wall superheat based on experimental data. A baseline for the numerical model used in this study was established by comparing with results from Fincher [13]. After simulating the built-in boiling functions, user-defined functions for nucleation site density and bubble departure diameter were implemented. While the geometry was significantly different from the pool boiling model, the functions that demonstrated the best agreement with experimental data in pool boiling scenarios were chosen for use in flow boiling.

4.3.1 Numerical Simulation of Four Die in a Cartridge Model

All flow boiling simulations were performed using a numerical model in which four die were attached to a printed circuit board and vertically suspended in a modular cartridge with subcooled Novec 649 circulating through the cartridge. Also included in both the experimental and numerical models was a flow distributor designed by Gess [35, 50] to direct the flow of incoming Novec 649 over the heated die to improve convective heat transfer. Additional information on the numerical model including geometry and meshing is given in the next section.

4.3.1.1 Model Description

As with pool boiling simulations, the numerical modeling for flow boiling was performed using ANSYS Icepak and ANSYS Fluent with the former used to create and mesh the model and the latter used to setup multiphase solvers and perform the simulations. The flow boiling numerical model used in this study, including the flow

distributor attached to the inlet, four die, PCB and outlet in the upper left, is shown in Figure 4.28. The model in this study was replicated from a CAD file supplied by Gess [35, 50] and was very similar to the experimental fabrication with the exception of the chilled water header (CWH). The CWH is a group of aluminum fins that extend from the top wall of the cartridge module and would be in the yellow dashed region of Figure 4.28; its purpose is to provide condensation sites and increase heat removal from the fluid by increasing the available surface area. Experimental results included a CWH and numerical simulations by Fincher [13] were performed with and without the CWH. Fincher [13] determined that including the CWH decreased the predicted temperature rises by approximately 0.5°C compared to numerical models without the CWH. More significantly, including the CWH increased the computational time six fold [13]; therefore, the numerical models in this study omitted the CWH.

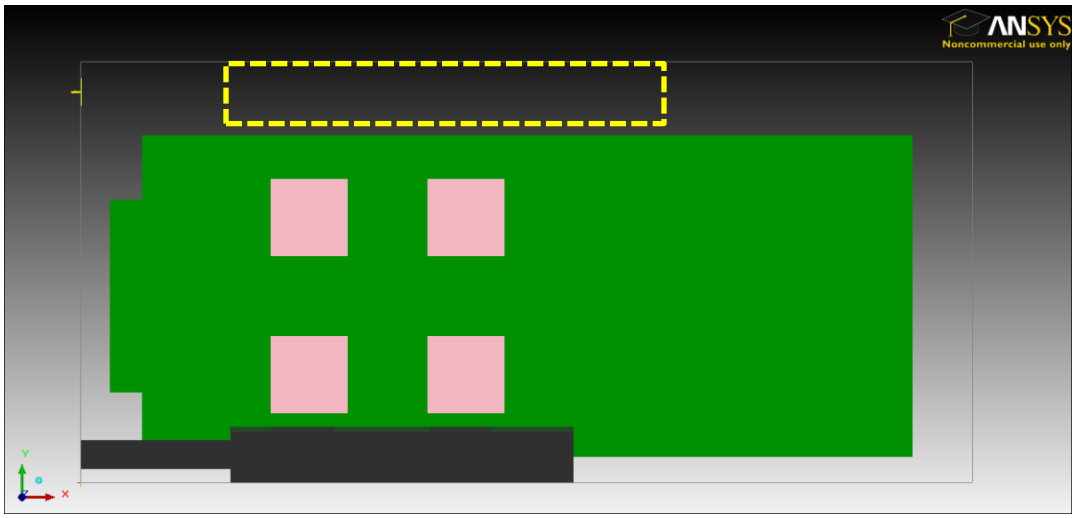

Figure 4.28: Numerical Model used in Flow Boiling Simulations

The printed circuit board (PCB) was modeled to replicate the one used in experiments including the step down on the edge nearest the inlet and outlet ports. The

four die were modeled using silicon blocks with uniform heat dissipation ranging from 3 to 12 W/cm^2. The flow rate of the incoming Novec 649 was typically 800 mL/min. To improve the flow path, Gess [35, 50] designed a flow distributor to direct the fluid over the heated surfaces; this was also included in the numerical model and was based on CAD files from Gess and the numerical model from Fincher [13]. For more information on the experimental setup, see the study by Gess [35, 50].

Models contained approximately 1 million nodes using a non-conformal mesh with the Mesher-HD scheme. Different grids were used around the flow distributor, each die and the outlet while a relatively coarser grid was used for the rest of the computational domain called the global mesh. The non-conformal mesh is shown in Figure 4.29 where the cut plane is parallel to the die and PCB and located 2.5 mm from the die surface to illustrate the refined grid around the die and flow distributor.

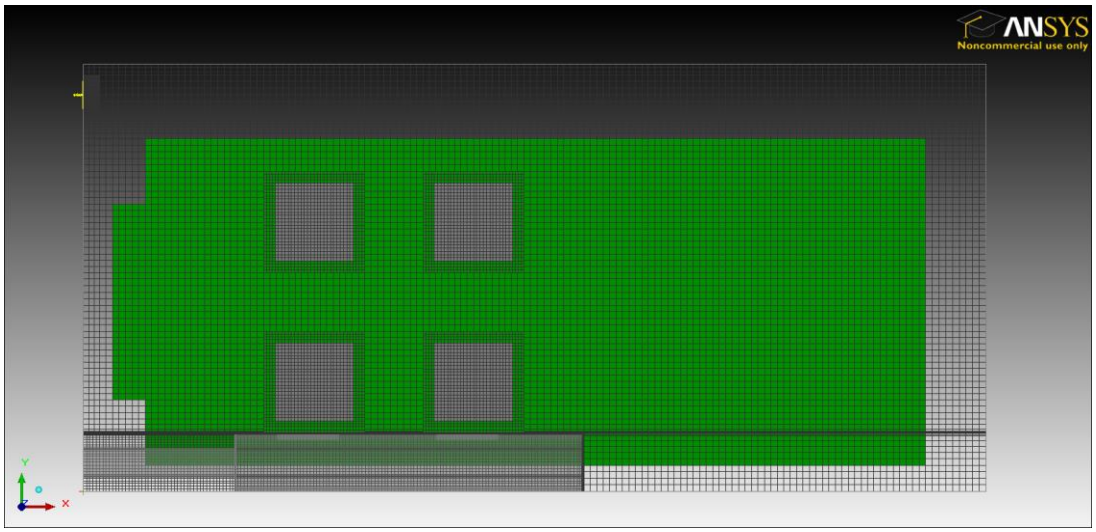

Figure 4.29: Non-Conformal Mesh Used with the Models for Flow Boiling Simulations

In addition to the non-conformal mesh, slack was included around the die and outlet. Slack is defined as the distance beyond the object boundaries to which the non-

conformal mesh is also applied. For example, the slack around each die was 3.5 mm, 3.5 mm and 1.5 mm in the x, y and z-directions, respectively. The element sizes for the die and duct mesh were 1.0 mm, 1.0 mm and 0.5 mm in the x, y and z-directions, respectively. The flow outlet element sizes were 0.25 mm in all directions while the global mesh had the largest element sizes at 2.0 mm, 2.0 mm and 1.0 mm in the x, y and z-directions, respectively. As Fincher [13] had done, a study of grid size was performed to ensure grid independence. Models using a coarser grid with approximately 500,000 elements and a finer grid with approximately 1.4 million elements were simulated and the change in predicted die surface temperatures were relatively negligible.

This completes the description of the numerical model used in flow boiling simulations; the next section briefly summarizes the ANSYS Fluent solver settings and convergence criteria.

4.3.1.2 Fluent Solver Settings and Convergence Criteria

For flow boiling simulations, the Non-Equilibrium boiling model was used along with the k-ε RNG turbulent model. Radiation was ignored in all cases. For the interaction models between the liquid and vapor phases, the Ishii, Moraga and Ranz-Marshall models were used for the drag coefficient, lift coefficient and heat transfer, respectively. These correlations were given by Eq. (3.3) to (3.10) in the previous chapter. Pressure and velocity were solved using a coupled with volume fractions scheme and other quantities, such as momentum, turbulent kinetic energy (TKE) and turbulent dissipation rate (TDR), were discretized using first order upwind. The relaxation factors for momentum and pressure were set to 0.5 and 0.2, respectively, while relaxation factors were set to 0.3 for

the turbulent terms (TKE, TDR, turbulent viscosity) and 0.6 for other terms (density, body forces, etc). The nondimensional flow Courant number was set to 5.

For solution initialization, the liquid phase and vapor phase temperatures were initialized to 307.15K (15°C subcooled) and 322.15K (saturation temperature of Novec 649), respectively. The initial TKE was reduced from 1 m^2/s^2 to 0.001 m^2/s^2 while the initial TDR was left as the default value of 1 m^2/s^3. Parallel processing was used in which five to eleven computer cores, depending on the number of simultaneous simulations, were used to reduce computational time. BCGSTAB and double precision were also used. Lastly, full convergence was obtained in all cases with flow terms converging to a minimum of 10^{-5} and energy terms converging to a minimum of 10^{-7}.

The remainder of this chapter is dedicated to discussing flow boiling results. For the initial set of results, all boiling parameters (area of influence, frequency of bubble departure, nucleation site density and bubble departure diameter) were set to default, built-in functions. Numerical results were compared to experimental data from Gess [50] and numerical results from Fincher [13]. The next set of numerical results involved user-defined functions for nucleation site density and bubble departure diameter.

4.3.1.3 Default, Built-In Boiling Parameters

To establish a baseline for flow boiling in the cartridge model, all the boiling parameters were set to the built-in default functions. The baseline numerical results for flow boiling are compared to experimental data [50] and Fincher's numerical results [13] in Figure 4.30, which plots heat flux as a function of the temperature difference between the die surface and the inlet temperature of 15°C (34°C subcooled). The volumetric flow rate for the experimental data from Gess [50] ranged from 360 to 1250 mL/min while the

flow rate for both sets of numerical results was fixed at 800 mL/min. It should be noted that the experimental data included the chilled water header (CWH) while both sets of numerical results omitted it to reduce computation time. Fincher noted a relatively minor difference in predicted die temperatures when including the CWH [13].

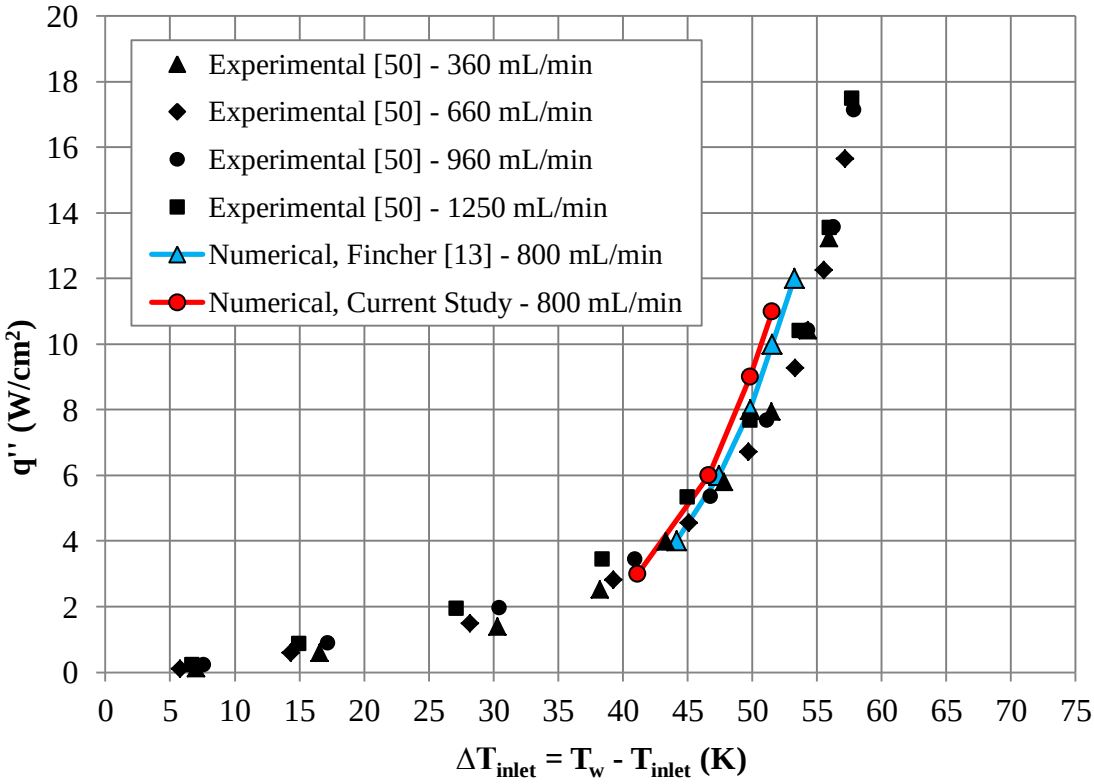

Figure 4.30: Cartridge Model Heat Flux as a Function of Temperature Difference between the Wall and Inlet, All Default Boiling Parameters

Both sets of numerical results were within 1.2°C over the range of heat fluxes simulated with the temperature variations attributed to differences in the mesh or element sizes. The set of boiling parameters used in Figure 4.30 for flow boiling is the same set used in Figure 4.4 (denoted Case A) with pool boiling that resulted in significantly under predicted die temperatures and an incorrect boiling curve slope. While the default boiling parameters resulted in good agreement with experimental data for flow boiling, this

inconsistency from pool to flow boiling continues to emphasize the unpredictable nature of the built-in functions.

4.3.1.4 Combination of User-Defined Functions for NSD and BDD

With a baseline set of results and confidence in the numerical model established, the next set of results incorporates several combinations of user-defined functions (UDF) for bubble departure diameter and nucleation site density. The numerical results with two sets of UDFs can be seen in Figure 4.31 along with the results with all default functions.

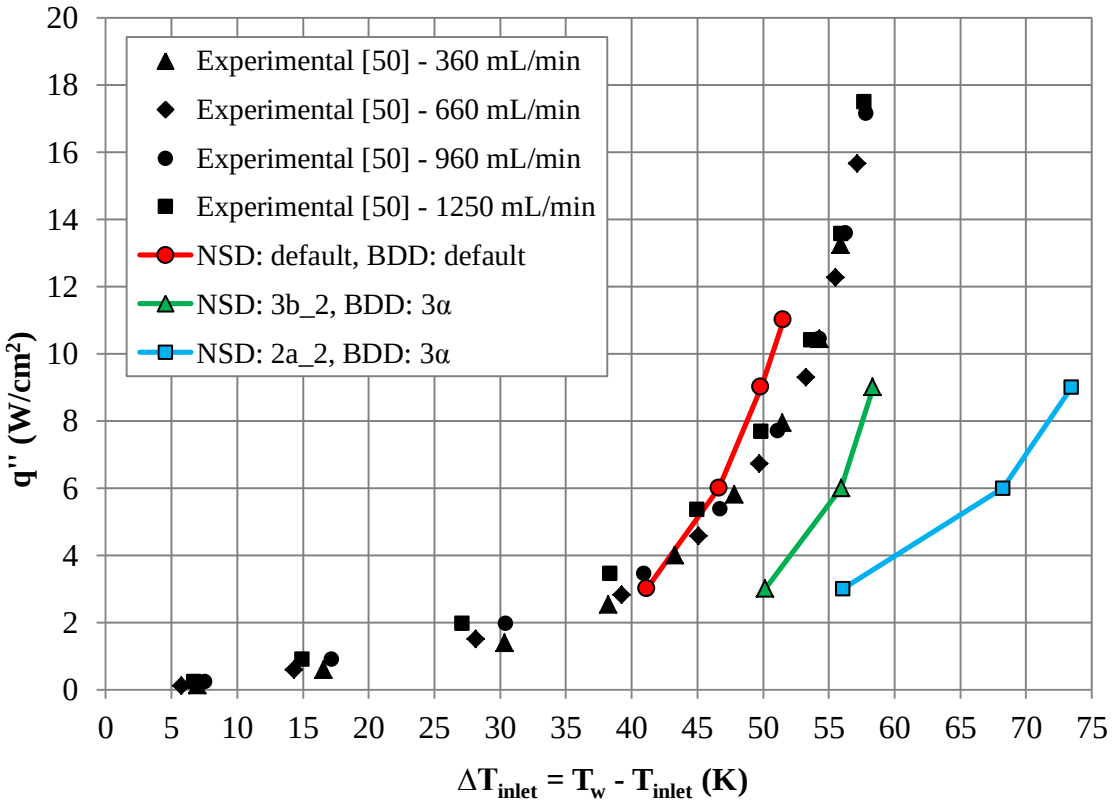

Figure 4.31: Cartridge Model Heat Flux as a Function of Temperature Difference between the Wall and Inlet, User-Defined Functions

In Figure 4.31, the volumetric flow rate for all numerical simulations remained 800 mL/min and all the simulations with UDFs used the bubble departure diameter function

that was most representative of experimental data from Sridhar, et al. [19], i.e. BDD: 3α. The user-defined functions that demonstrated the best agreement with experimental data in the previous pool boiling models (NSD: 2a_2, BDD: 3α) demonstrated poor agreement with experimental data in the flow boiling cartridge model despite the relatively low inlet velocity. The die surface temperatures were over predicted by approximately 20°C in the range of heat fluxes from 3 to 9 W/cm^2. Based on the parametric trials with nucleation site density, a different function (NSD: 3b_2) was also simulated in an attempt to improve agreement with experimental data. While this second NSD function resulted in relatively better agreement with experimental data (die temperatures over predicted by 9°C), the results were overall disappointing especially considering the UDFs used were those that performed well in pool boiling. The poor agreement seen in Figure 4.31 with flow boiling could be an extension of the problems that were seen in the pool boiling simulations where the degree of subcooling was varied (Fig. 4.26). In both cases, more subcooling (from a lower pool or low incoming flow temperature) resulted in higher surface temperatures.

Streamlines showing the flow path and velocity magnitudes for the flow boiling cartridge model can be seen in Figure 4.32 for an inlet volumetric flow rate of 800 mL/min and die heat flux of 6 W/cm^2 using the NSD: 2a_2 and BDD: 3α functions. The effect of the flow distributor can be seen as the flow is directed over the die surfaces to enhance convective heat transfer. The vapor fraction contours on the surfaces of each die can be seen in Figure 4.33 along with their relative magnitudes. The streamlines and vapor fraction contours were generated from the same numerical model. Vapor fractions were extremely under predicted correlating with relatively minor boiling heat transfer.

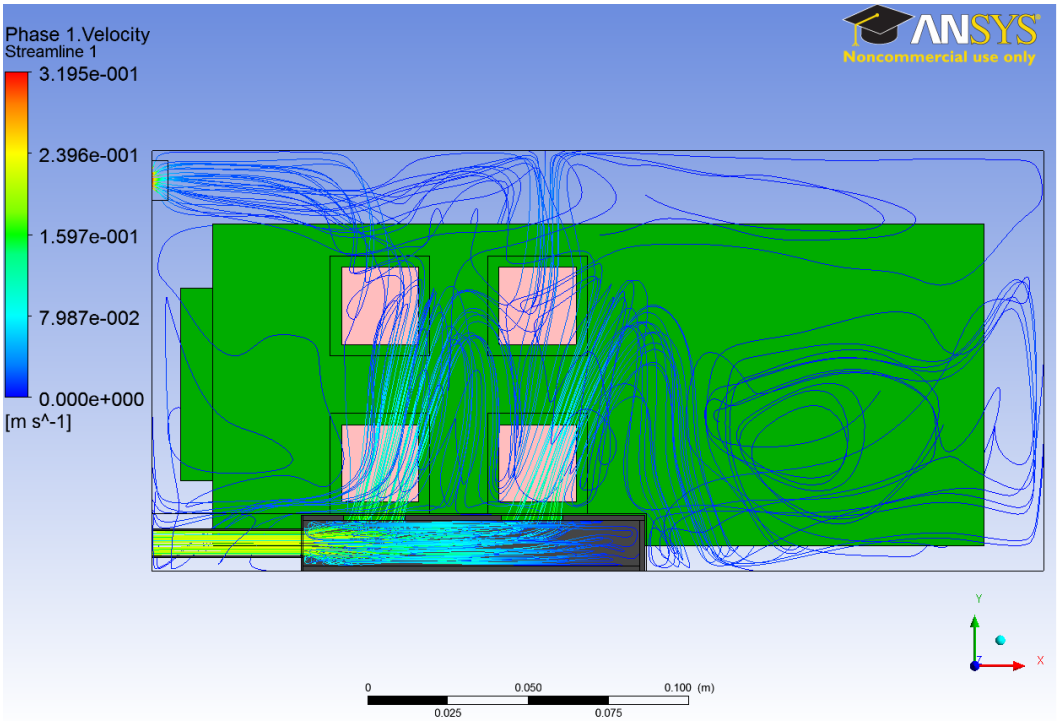

Figure 4.32: Streamlines for Cartridge Flow Boiling Model at 800 mL/min, 6 W/cm^2 and NSD: 2a_2 and BDD: 3α

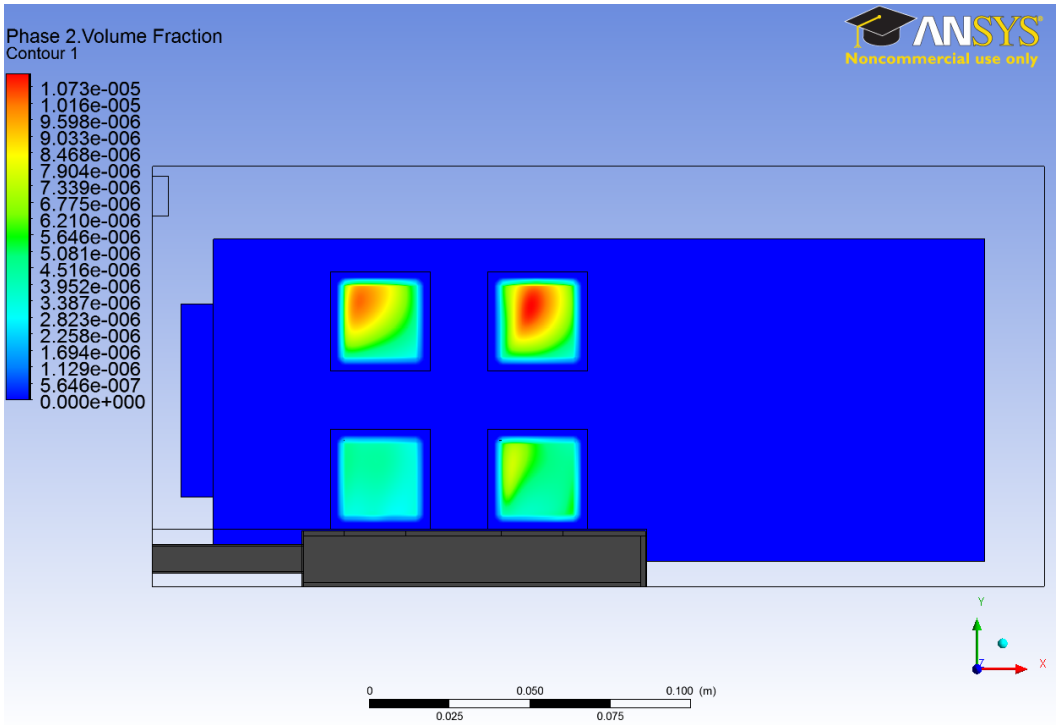

Figure 4.33: Vapor Volume Fraction for Cartridge Flow Boiling Model at 800 mL/min, 6 W/cm^2 and NSD: 2a_a and BDD: 3α

The poor agreement seen with the numerical results in Figure 4.31 and the discrepancy with default functions from pool to flow boiling (Case A) necessitate a closer examination of the boiling model, in particular the boiling parameters that were not examined in this study, such as the area of influence and frequency of bubble departure. The effect of changing the degree of subcooling should also be examined in more detail as it had a tremendous and counterintuitive effect on die surface temperatures in the pool boiling models that was never resolved and could be contributing to the poor agreement seen in flow boiling.

Chapter 5

SUMMARY AND CONCLUSIONS

In this chapter, a brief summary of the pool and flow boiling results will be given along with the most significant conclusions. In the final section, recommendations for future work will also be discussed.

5.1 Pool Boiling Simulations

For the pool boiling simulations, a numerical model based on an experimental setup for high power server modules was simulated using subcooled Novec 649 with a range of nucleation site density and bubble departure diameter functions including built-in functions provided by ANSYS Fluent as well as user-defined functions.

The four combinations of built-in functions based on empirical data, denoted Case A to D, resulted in a range of agreement with experimental data from within 2°C at best to over predicting the die surface temperature by 40°C at worst. The increasing slope of heat flux versus wall temperature typically seen in boiling curves was also not consistently reproduced. This inconsistency and lack of applicability led to parametric trials for nucleation site density and bubble departure diameter to determine general trends and interactions between the various boiling parameters.

Twelve nucleation site density and six bubble departure diameter functions based on the same equation form as the default, built in functions were simulated individually and in combination with one another. Agreement with experimental data improved to

within 1°C over the range of heat fluxes from 3 to 12 W/cm^2 by incorporating experimental data for bubble departure diameter at the appropriate subcooling. The combination of functions that resulted in the best agreement with experimental data was NSD: 2a_2, BDD: 3α and the default formulations for area of influence and frequency of bubble departure. While the twelve nucleation site density user-defined functions deviated from the default built-in formulation, they were still limited to the same equation form that resulted in a linear trend when plotted on a log-log scale. A piecewise nonlinear user-defined function for nucleation site density was explored in combination with the best performing bubble departure diameter function to better capture the boiling curve slope, especially at higher heat fluxes. Improved agreement with experimental data was seen when the numerical results for the piecewise nonlinear and previous nucleation site density functions were compared.

The last two sets of pool boiling simulations included variations of the degree of subcooling and variations of the turbulence model. The k-ε RNG turbulence model was used nearly exclusively in this study. A total of three turbulence models were simulated (k-ε: RNG, k-ε: Standard and k-ω: Standard) with all other parameters being the same. The predicted die surface temperatures were all within 1.2°C with the largest temperature differences occurring between distinct families of turbulence models, i.e. k-ε and k-ω, with negligible temperature differences being predicted by the standard and RNG k-ε turbulent models. The pool of Novec 649 was subcooled 15°C below the saturation temperature for the majority of the pool boiling simulations; however, boiling curves were also generated for 13°C and 18°C using NSD: nonlinear_1c and BDD: 3α. The multiphase results were not particularly promising as several odd characteristics

appeared. The multiphase numerical results suggested that a lower pool temperature (higher subcooling) would result in a higher surface temperature and vice versa for a higher pool temperature (lower subcooling). The single phase numerical results at 1 W/cm^2 collapsed to the same data point suggesting that the multiphase solver or user-defined functions need to be explored further.

5.2 Flow Boiling Simulations

For the flow boiling simulations, a numerical model based on an experimental setup for a four die cartridge was simulated using subcooled Novec 649 and a volumetric inlet flow rate of 800 mL/min. The goal was to expand the user-defined functions that resulted in the best agreement with experimental data under pool boiling conditions to this flow boiling model. A baseline set of heat fluxes were simulated using all default boiling parameters and compared with previous numerical and experimental work. The temperature difference between the wall and inlet predicted by the numerical model with all default boiling parameters was within 1 to 3°C of experimental data. This set of boiling parameters was the same as Case A in pool boiling, which resulted in die temperatures that were under predicted by up to 15°C. This opposite effect of having a set of boiling parameters that resulted in poor agreement in pool boiling yet good agreement in flow boiling continued with user-defined functions. In the pool boiling model, NSD: 2a_2 and BDD: 3α resulted in agreement with experimental data to within 1°C; however, the same set of functions applied to the flow boiling model resulted in the die surface temperatures being over predicted by approximately 18°C. Another nucleation site density function was simulated with BDD: 3α that resulted in better agreement and a boiling curve slope more representative of experimental data; die surface temperatures

were over predicted by approximately 9°C in this case. In all flow boiling simulations, the vapor fraction was significantly under predicted suggesting the simulations were dominated by convective as opposed to boiling heat transfer.

5.3 Recommendations for Future Work

In this study, exploration of the boiling parameters was limited to the nucleation site density and bubble departure diameter functions. The other two boiling parameters, area of influence and frequency of bubble departure, were left as the default built-in functions for all simulations. Future work could include applying user-defined functions to replace these other boiling parameters and exploring their interactions within the multiphase model. In the pool boiling simulations that varied the degree of subcooling, odd behavior that was contrary to physical expectations was seen. The single phase results were as expected; however, the multiphase results with user-defined functions were not. The user-defined functions for bubble departure diameter were based on experimental data for a dielectric fluid (granted, not the same dielectric fluid used in this study); however, no experimental data was available upon which to base the nucleation site density function.

Flow boiling results involving user-defined functions were quite poor with die surface temperatures over predicted and vapor fractions under predicted by a relatively large margin. The function used for the single phase heat transfer coefficient in the convective heat flux term was never explicitly found and could provide further insight on the relative magnitudes of the convective, quenching and evaporative heat fluxes. Also, the pool temperatures calculated in ANSYS Fluent when using built-in functions are based on the temperature of the numerical cell next to the heated surface; this results in

grid dependent solutions and is particularly important with respect to the quenching heat flux. ANSYS Fluent offers a "Quenching Model Correction" in which the pool temperature may be specified as a fixed temperature or may be found at a fixed nondimensional distance from the wall, i.e. a y^+ value. Preliminary simulations were performed using both with the flow boiling model and it was determined the default y^+ value of 250 had a negligible impact on predicted die temperatures. The simulation with a fixed liquid temperature was potentially more promising; however, all simulations with the Quenching Model Correction required four to five times as much computational time as those performed without it.

References

[1] Fruehe, J. "Why are datacenter power and cooling still challenging?" [PDF]. Moor Insights & Strategy. Available: http://www.moorinsightsstrategy.com/wp-content/uploads/2014/06/Why-Are-Datacenter-Power-and-Cooling-Still-Challenging-by-Moor-Insights-and-Strategy.pdf. June 2014. Web. 16 Dec. 2014.

[2] Koomey, J. "Growth in data center electricity use 2005 to 2010." Oakland, CA: Analytics Press. Aug. 1, 2011. http://www.analyticspress.com/datacenters.html.

[3] Khosrow, E., Jones, G. F., and Fleischer, A. S. "A review of data center cooling technology, operating conditions and the corresponding low-grade waste heat recovery opportunities." *Renewable and Sustainable Energy Review.* 31. 622-638. 2014.

[4] Gordon, M. E. "Cramming more components onto integrated circuits." *Electronics*. 114-117. Apr. 19, 1965.

[5] Geisler, K., and Bar-Cohen, A. *Encyclopedia of Thermal Packaging. Set 1: Thermal Packaging Techniques.* Ed. Avram Bar-Cohen. Vol. 3. University of Maryland: World Scientific, 2013.

[6] 3M. (2012). "Playing It Cool." May, 2012 [PDF]. Available: http://multimedia.3m.com/mws/media/802218O/novec-immersion-cooling-process.pdf?&fn=Novec%20Immersion%20Cooling.pdf

[7] Green Revolution Cooling. "Cost savings & comparison." Mar. 2014. http://www.grcooling.com/data-center-cost-savings/

[8] Green Revolution Cooling. "The next big boost for Bitcoin mining: oil immersion cooling." Dec. 2014. http://www.grcooling.com/bitcoin-mining/

[9] Judge, P. “Liquid cooling for data centre servers passes Intel tests.” T*echWeekEurope.* UK. N.p., 5 Sept. 2012. Web. 18 Dec. 2014.

[10] Shah, A. “Intel and SGI cool servers by dunking them.” *PCWorld.* US. N.p., 8 Apr. 2014. Web. 18 Dec. 2014.

[11] Miller, R. “Facebook tests immersion cooling.” *Data Center Knowledge.* iNET Interactive. 21 Dec. 2012. Web. 18 Dec. 2014.

[12] Miller, R. “Dunking for density: new projects pursue 3M’s take on immersion cooling.” *Data Center Knowledge.* iNET Interactive. 13 Nov. 2013. Web. 18 Dec. 2014.

[13] Fincher, S. N. “Numerical simulations of boiling in dielectric fluid immersion cooling scenarios of high power electronics.” Master’s thesis. Auburn University, 2014.

[14] In, W. K., Shin, C. H., and Lee, C. Y. “CFD simulation of subcooled boiling flow in nuclear fuel bundle.” Paper presented at *7th International Conference on Computation Fluid Dynamics (ICCFD7)*, Big Island, Hawaii, July. 9-13, 2012.

[15] Wang, C., Cong, T., Qiu, S., Tian, W., Wu, Y., and Su, G. “Numerical prediction of subcooled wall boiling in the secondary side of SG tubes coupled with primary coolant.” *Annals of Nuclear Energy*. 63. 633-645. 2014.

[16] Kim, H. T., Park, H. K., Kim, Y. T., Bang, K. H., and Suh, J. “Flow boiling in an inclined channel with downward-facing heated upper wall.” *Heat Transfer Engineering.* 35.5. 492-500. 2014.

[17] Narumanchi, S., Troshko, A., Bharathan, D., and Hassani, V. “Numerical simulations of nucleate boiling in impinging jets: Applications in power electronics cooling.” *International Journal of Heat and Mass Transfer*. 51.1. 1-12. 2008.

[18] Končar, B., and Matkovič, M. “Simulation of turbulent boiling flow in a vertical rectangular channel with one heated wall.” *Nuclear Engineering and Design*. 245. 131-139. 2012.

[19] Sridhar, A., Styslinger, S., Duron, C. M., Bhavnani, S. H., Knight, R. W., Harris, D. K., and Johnson, R. W. "Cooling of high-performance server modules using direct immersion." HT2012-58433. *Proceedings of the ASME 2012 Summer Heat Transfer Conference*, Puerto Rico. 2012.

[20] ANSYS, ANSYS Fluent. "14.0 Theory Guide." ANSYS Inc. 2011.

[21] Lavieville, J., Quemerais, E., Boucker, M., and Maas, L. "NEPTUNE CFD V1.0 Theory Manual." EDF. 2005.

[22] Lifante, C., Frank, T., and Burns, A. "Wall boiling modeling extension towards critical heat flux." *15th International Topical Meeting on Nuclear Reactor Thermalhydraulics*. Pisa, Italy. May 12-15, 2013.

[23] Del Valle, V. H., and Kenning, D. B. R. "Subcooled flow boiling at high heat flux." *International Journal of Heat and Mass Transfer.* 28.10. 1907-1920. 1985.

[24] Cole, R. "A photographic study of pool boiling in the region of the critical heat flux." *Journal of American Institute of Chemical Engineers.* 6. 533-542. 1960.

[25] Lemmert, M., and Chawla, L. M. "Influence of flow velocity on surface boiling heat transfer coefficient." *Heat Transfer in Boiling.* Hahne, E., and Grigull, U., Eds., Academic Press and Hemisphere, New York, NY, USA. 1977.

[26] Tolubinski, V. I., and Kostanchuk, D. M. "Vapor bubbles growth rate and heat transfer intensity at sub-cooled water boiling." *4th International Heat Transfer Conference*, Paris, France. 1970.

[27] Končar, B., Kljenak, I., and Mavko, R. "Modeling of local two-phase flow parameters in upwards subcooled flow boiling at low pressure." *International Journal of Heat and Mass Transfer.* 47. 1499-1513. 2004.

[28] Kocamustafaogullari, G., and Ishii, M. "Foundation of the interfacial area transport equation and its closure relations." *International Journal of Heat and Mass Transfer.* 38. 481-493. 1995.

[29] Kocamustafaogullari, G., and Ishii, M. "Interfacial area and nucleation site density in boiling systems." *International Journal of Heat and Mass Transfer.* 26.9. 1377-1387. 1983.

[30] Unal, H. C. "Maximum bubble diameter, maximum bubble growth time and bubble growth rate during subcooled nucleate flow boiling of water up to 17.7 MN/m^2." *International Journal of Heat and Mass Transfer.* 19. 643-649. 1976.

[31] Vyskocil, L., and Macek, J. "Boiling flow simulation in Neptune_CFD and Fluent codes." XCFD4NRS, Grenoble, France. 2008.

[32] Chen, E., Li, Y., and Cheng, X. "CFD simulation of upward subcooled boiling flow of refrigerant-113 using the two-fluid model." *Applied Thermal Engineering*. 29.11. 2508-2517. 2009.

[33] Prabhudharwadkar, D., Lopez de Bertodano, M., and Buchanan, J. "Assessment of the heat transfer model and turbulent wall functions for two fluid CFD simulations of subcooled and saturated boiling." *7th International Conference on Multiphase Flow (ICMF 2010).* Tampa, FL. May 30 - June 4, 2010.

[34] Carey, V. P. *Liquid-Vapor Phase-Change Phenomena.* 2nd edition. New York: Taylor and Francis Group, LCC. 2008.

[35] Gess, J., Bhavnani, S.H., Ramakrishnan, B., Johnson, R. W., Harris, D. K., Knight, R. W., Hamilton, M., and Ellis, C. "Investigation and characterization of a high performance, small form factor, modular liquid immersion cooled server model." *30th Annual Thermal Management, Modeling and Management Symposium, SemiTherm.* San Jose, CA, USA, March 9-13, 2014.

[36] Fluent, ANSYS. "Lecture 8: user defined functions (UDFs)" from customer training material titled *Introduction to ANSYS Fluent*. ANSYS Inc. 2010.

[37] Fluent, ANSYS. "14.0 ANSYS Fluent UDF Manual." ANSYS, Inc. Canonsburg, PA, USA, 2013.

[38] Domalapally, P., Rizzo, E., Richard, L. S., Subba, F., and Zanino, R. "CFD analysis of flow boiling in the ITER first wall." *Fusion Engineering and Design.* 87. 556-560. 2012.

[39] Ying, A., Waku, T., Youchison, D. L., Hunt, R., Zhang, H. G., and Ulrickson, M. A. "A subcooled boiling heat transfer predictive model for ITER EHF FW designs." *Fusion Engineering and Design.* 86. 667-670. 2011.

[40] Ningegowda, B. M., and Premachandran, B. "Numerical simulation of two-dimensional forced convective film boiling flow over a horizontal flat surface." *International Union of Theoretical and Applied Mechanics (IUTAM).* 15. 256-263. 2014.

[41] Sussman, M., and Puckett, E. G. "A coupled level set and volume-of-fluid method for computing 3D and axisymmetric incompressible two-phase flows." *Journal of Computational Physics.* 162. 301-337. 2000.

[42] Mukherjee, A., and Kandlikar, S. G. "Numerical simulation of growth of a vapor bubble during flow boiling of water in a microchannel." *Microfluidics and Nanofluidics.* 1. 137-145. 2005.

[43] Gong, S., and Cheng, P. "Lattice Boltzmann simulation of periodic bubble nucleation, growth and departure from a heated surface in pool boiling." *International Journal of Heat and Mass Transfer.* 64. 122-132. 2013.

[44] Sun, T., and Weizhong, L. "Three-dimensional numerical simulation of nucleate boiling bubble by lattice Boltzmann method." *Computers and Fluids.* 88. 400-409. 2013.

[45] Ishii, M. "Two-fluid model for two-phase flow." *2nd International Workshop on Two-Phase Flow Fundamentals.* RPI, Troy, NY, USA, 1979.

[46] Moraga, F. J., Bonetto, F. J., and Lahey, R. T. "Lateral forces on spheres in turbulent uniform shear flow." *International Journal of Multiphase Flow.* 25. 1321-1372. 1999.

[47] Ranz, W. E., and Marshall, W.R. "Vaporation from drops, Part I." *Chem. Eng. Prog.* 48 (3). 141-146. March 1952.

[48] Ramakrishnan, B., Bhavnani, S. H., Gess, J., Knight, R. W., Harris, D. K., and Johnson, R. W. "Effect of system and operational parameters on the performance of an immersion-cooled multichip module for high performance computing." *30th Annual Thermal Measurement, Modeling, and Management Symposium, SemiTherm.* San Jose, CA, USA, March 9-13, 2014.

[49] Knight, R. W., Fincher, S., Bhavnani, S. H., Harris, D. K., and Johnson, R. W. "A numerical study of single phase dielectric fluid immersion cooling of multichip modules." *Proceedings of the 2012 IMAPS Conference*. San Diego, CA, USA, 2012.

[50] Gess, J., Bhavnani, S. H., and Johnson, R. W. "Thermal resistance and PIV characterization of a line-replaceable compact liquid-cooled server module for high performance computing platforms." *International Mechanical Engineering Congress and Exposition, IMECE*. Montreal, QC, Canada. Nov. 14-20, 2014.

[51] Bhavnani, S. H., Fournelle, G., and Jaeger, R. C. "Immersion-cooled heat sinks for electronics: insight from high-speed photography." *IEEE Transactions on Components and Packaging Technologies.* 24.2. June 2001.

[52] Tong, W., Bar-Cohen, A., and Simon, T. W. "Thermal transport mechanisms in nucleate pool boiling of highly-wetting liquids." *Proceedings of the 9th International Heat Transfer Conference*. 2. 27-32. 2004.

[53] Henry, C. D., and Kim, J. "A study of the effects of heater size, subcooling, and gravity level on pool boiling heat transfer." *International Journal of Heat and Fluid Flow.* 25. 262-273. 2004.

[54] Sathyamurthi, V., Ahn, H. S., Banerjee, D., and Lau, S. C. "Subcooled pool boiling experiments on horizontal heaters coated with carbon nanotubes." *Journal of Heat Transfer*. 131. 2009.

Appendices

Appendix A

SIMULATION SETUP PROCEDURE USING ICEPAK AND FLUENT

The information in this appendix serves as a procedural guide to not only replicating the numerical models in this study but also creating new models for future work. While other ANSYS products, such as ANSYS Workbench, can be used to create and mesh the numerical models, the chosen method presented in this appendix involves the use of two ANSYS products, Icepak and Fluent. Both are computational fluid dynamics programs; however, Icepak provides a more user-friendly graphical interface though it is limited to single phase simulations as it is a simplified frontend to Fluent. While less intuitive, Fluent provides significantly more options including the availability of multiphase solvers. Icepak and Fluent are able to share numerical models via a common file type, known as a "case" file with the .cas file extension.

This appendix begins with Icepak 14.0 followed by Fluent 14.0. In general, the former was used to create and mesh the numerical models while the latter was used to setup multiphase solvers and perform the simulations. This study emphases multiphase simulations; however, Icepak can be used as a standalone program if single phase simulations are desired. This appendix ends with post processing of results using another ANSYS product, CFD-Post 14.0.

A.1 Icepak 14.0

Icepak 14.0 was used to create both the pool boiling and flow boiling numerical models used in this study. Several predefined objects, such as the printed circuit board, help with model creation. Upon opening Icepak, the graphical user interface and prompt in Figure A.1 appear.

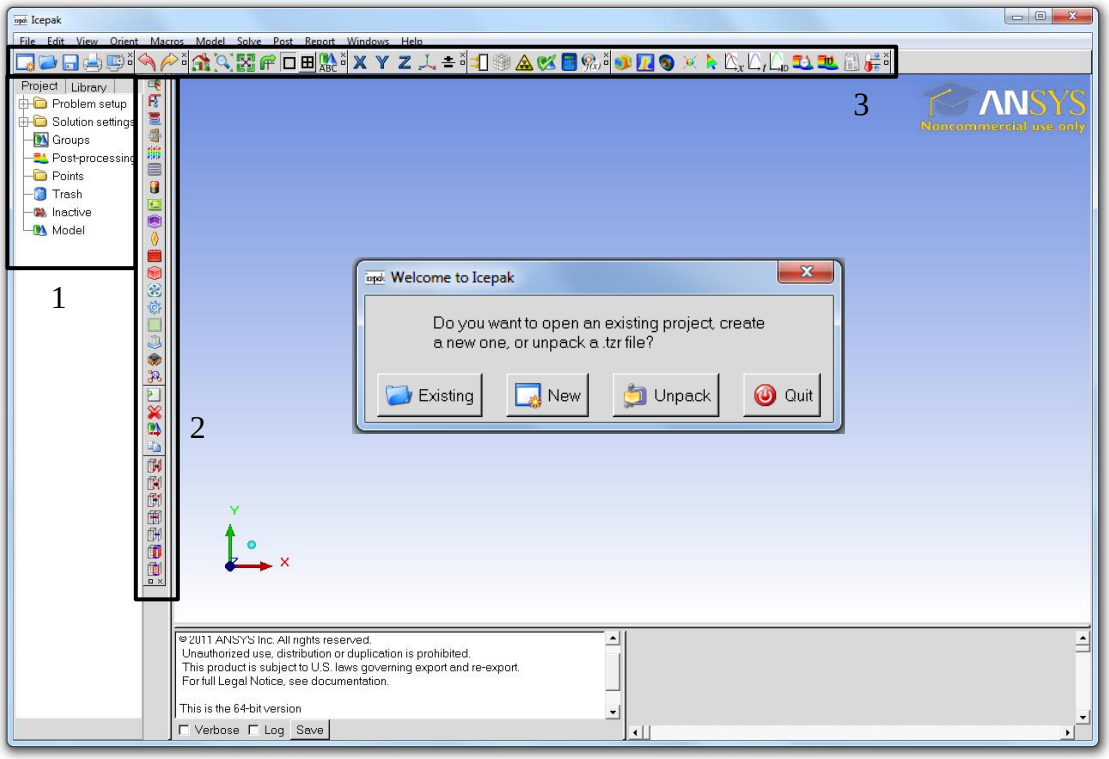

Figure A.1: Icepak 14.0 Opening Prompt and Graphical User Interface

In Figure A.1, there are several regions of interest. On the far left panel, denoted 1, are various features and components of the numerical model. As objects, such as the silicon die or printed circuit board, are created, they will populate this list to provide quick access and through double clicking or right clicking, other options become available. The most used options include translating, rotating or duplicating an object through options

available from right clicking. Typically, specifying material or object properties, such as heat generation, are available through double clicking.

The vertical panel of icons next to the left most panel, denoted 2, includes shortcuts to creating various components, such as source terms, the printed circuit board, blocks for silicon die and openings for flow passages. The horizontal panel across the top, denoted 3, includes shortcuts typically used for changing the orientation of the model or post processing via contours and particle traces. The next section describes the model creation procedure in more detail.

A.1.1 Model Creation

After selecting "New" from the prompt in Figure A.1, a computational cabinet is generated and added to the left most panel; this is shown in Figure A.2.

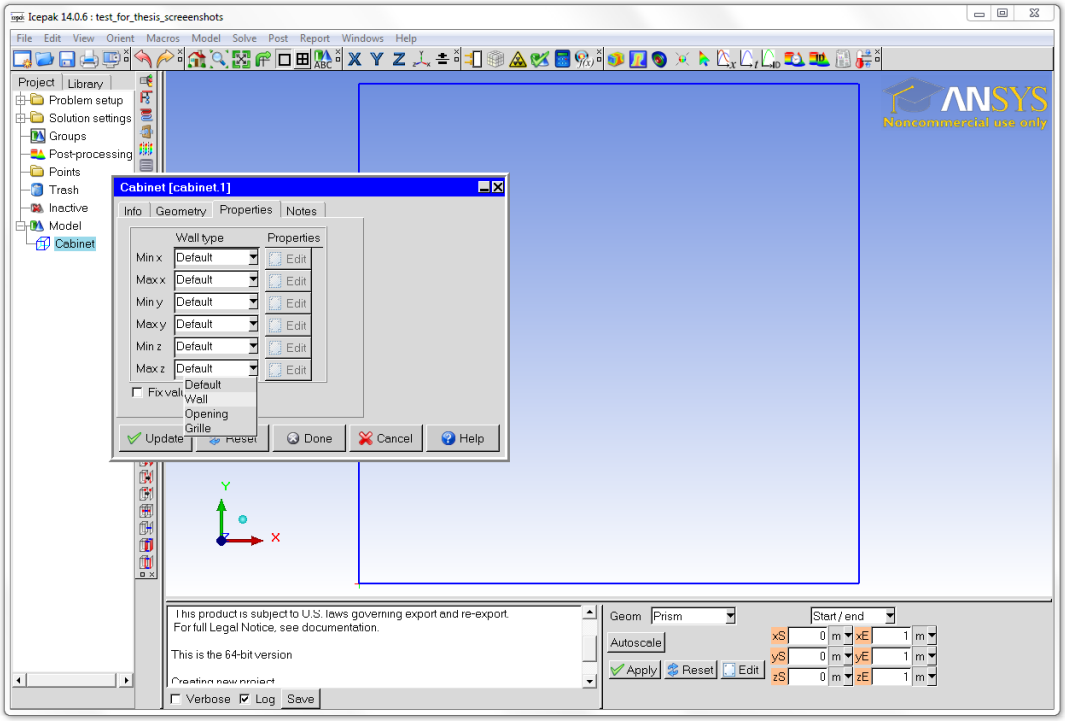

Figure A.2: Computational Cabinet and Associated Options

The computational cabinet is the solution domain and all components of the numerical model must be within the cabinet boundaries to be included in the meshing and simulation. By default, the cabinet is a 1 meter cube with an adiabatic solid wall on the boundaries; however, as shown in Figure A.2, the dimensions can and should be adjusted based on the length scale of the numerical model and the wall boundaries should be modified accordingly. For example, in the pool boiling simulations, the wall boundaries were changed from "Default" to "Opening" and the computational cabinet was reduced to 0.15m x 0.15m x 0.025m to minimize the number of elements.

For the relatively simple pool boiling models, only two components need to be created; these were the silicon die and printed circuit board (PCB). The silicon die was modeled from a "block" from the shortcut panel and the PCB was modeled using the built-in PCB component, also from the shortcut panel. It should be noted that there are more sophisticated built-in models for silicon die that can account for substrate, solder, etc. These are available under the "packages" option from the shortcut and can model PBGA, flip-chips, stacked die and others, also known as compact conduction modules; however, Fincher [13] noted difficulty in performing multiphase simulations with "packages." Figure A.3 shows the computational cabinet (no longer outlined in blue because the boundaries were changed to openings), the die and the PCB along with the window to modify the PCB properties after the appropriate dimensions were set. In both the pool and flow boiling numerical models, the die were modeled as silicon "blocks" due to the difficulty with multiphase simulations when using built-in compact conduction modules. Also, both pool and flow boiling used the same PCB properties with different geometries. The PCB type is compact with the predefined substrate material FR-4. The

trace material was the predefined Cu-Pure and the trace layer had surface thicknesses of 1.2 Cu-oz/ft^2 for both the high and low surface with 16% and 14% coverage for the high and low surface, respectively. These settings for the PCB resulted in an effective plane conductivity of approximately 3.7 W/m·K and normal conductivity of 0.4 W/m·K for the PCB used in the pool boiling models.

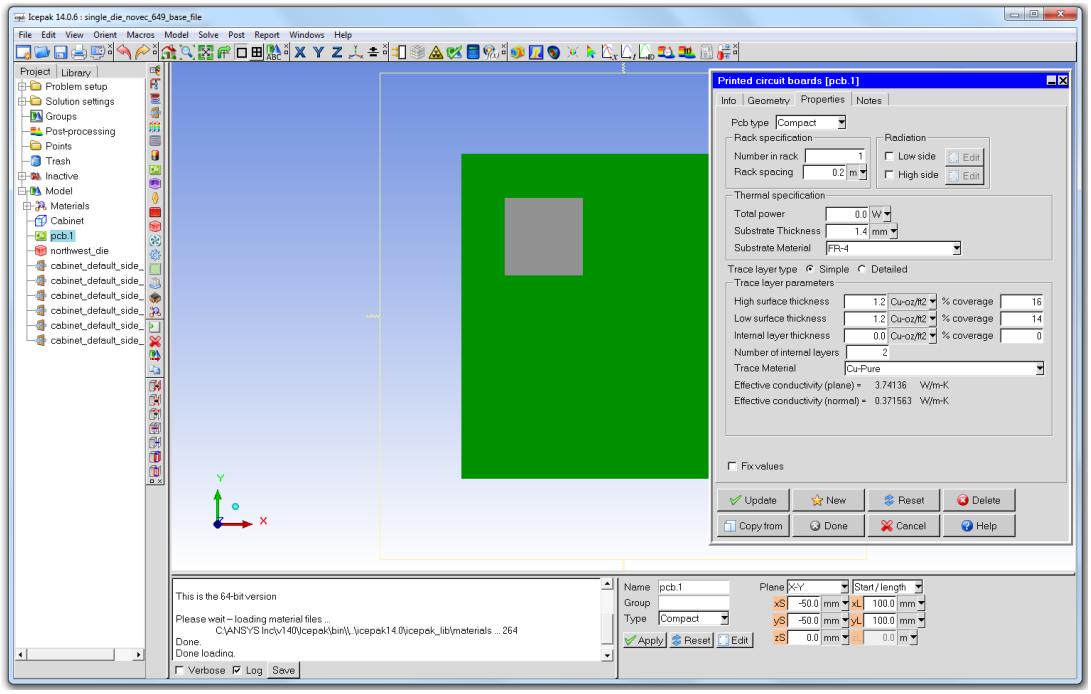

Figure A.3: Numerical Model Creation with Die and PCB

By expanding the **Problem Setup** menu, other options related to the numerical model can be defined. These options include which variables are solved, the flow regime and associated viscous model, and the bulk fluid temperature and pressure. Figure A.4 shows the **Basic Parameter** window with several of these options.

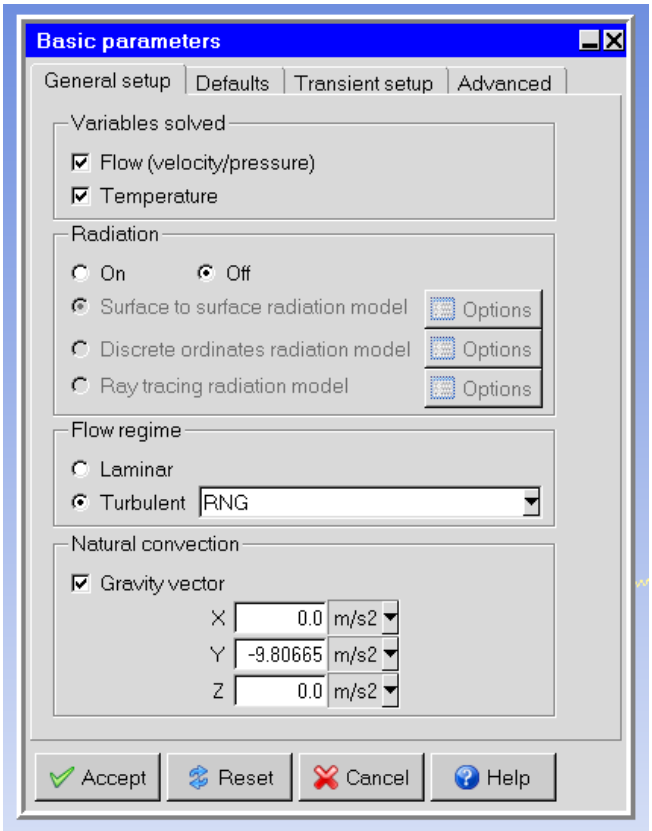

Figure A.4: Basic Parameters Window under Problem Setup

For all numerical models in this study, both the flow and temperature variables were solved, radiation was ignored, the flow regime was turbulent with the RNG solver and the gravity vector was in the usual orientation. While all of these options can be modified in Fluent, the more options that were set in Icepak before importing the model into Fluent, the more time was saved especially with the computational intensive cartridge model. Lastly, by expanding the **Solution Settings** menu, the number of iterations, the number of computer cores and the relaxation factors can be set either to save time or if single phase simulations are desired. This concludes model creation in Icepak for pool boiling models; a similar procedure was used to create the flow boiling models except additional

components, such as “openings” and more “blocks” for the duct, were needed. The next section discusses mesh generation.

A.1.2 Mesh Generation

One of the most critical phases of numerical modeling in this study was the mesh generation. A low quality mesh can result in poor numerical results and more importantly can cause instabilities in the solution and result in convergence problems or excessive oscillations in the residuals. Figure A.5 shows the **Mesh Control** window, which can be accessed from **Model → Generate Mesh** from the menu across the top.

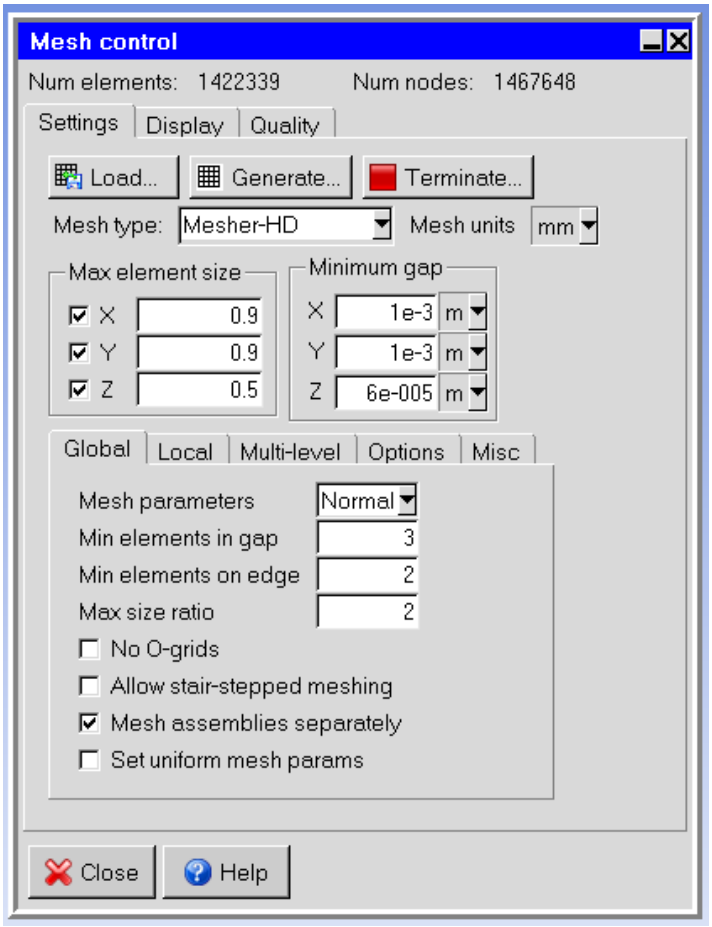

Figure A.5: Mesh Control Window

The “Mesh Control” window has three tabs for settings, display and quality. The **Settings** tab allows the selection of the mesh type and element sizes. In both pool and flow boiling simulations, “Mesher-HD” was used as the mesh type. In situations with more complex geometries or a large quantity of circular objects, another mesh type should be considered. The element sizes in the pool boiling models were 0.9, 0.9 and 0.5 mm for the x, y and z elements, respectively. This resulted in approximately 1.4 million elements and provided a balance between computational time and result quality. Under the second tab, denoted **Display**, the mesh can be view using plane cuts through the model or by selecting entire components. After meshing, the grid should be viewed to determine suitability and that mesh elements are not overly skewed. The last tab, denoted **Quality**, provides additional information about the mesh, such as the element volume, relative degree of skewness and relative face alignment.

This concludes the section on mesh generation. In the next section, the procedure to convert the model into a case file to be imported into Fluent will be discussed.

A.1.3 Case File Creation for Fluent

At this point in the setup, single phase simulations can be performed from Icepak; however, for this study, the Icepak models were converted to a case file and imported into Fluent to perform the multiphase simulations because those options were not available in Icepak. The **Solve** menu can be accessed from **Solve → Run Solution** from the menu across the top. Figure A.6 shows the **Advanced** tab for the **Solve** window.

The **Solve** menu contains three tabs for general setup, advanced and results. Under the **General Setup** tab, the file name can be chosen along with various solver options. It should be noted that if the simulation did not include a sufficient number of

iterations, the simulation can be continued from this tab without loss of data or needing to restart from the beginning. The **Results** tab includes options for setting post processing data and auto save functions.

For the purposes of creating a case file to later be imported into Fluent, the **Advanced** tab is of interest. As shown in Figure A.6 under **Solver Preprocessing**, the box marked "Don't start solver" is selected. This creates a case file with the model components, solver settings and mesh information but does not perform any iterations. The case file is saved in the same location as the Icepak model that was created upon first opening Icepak.

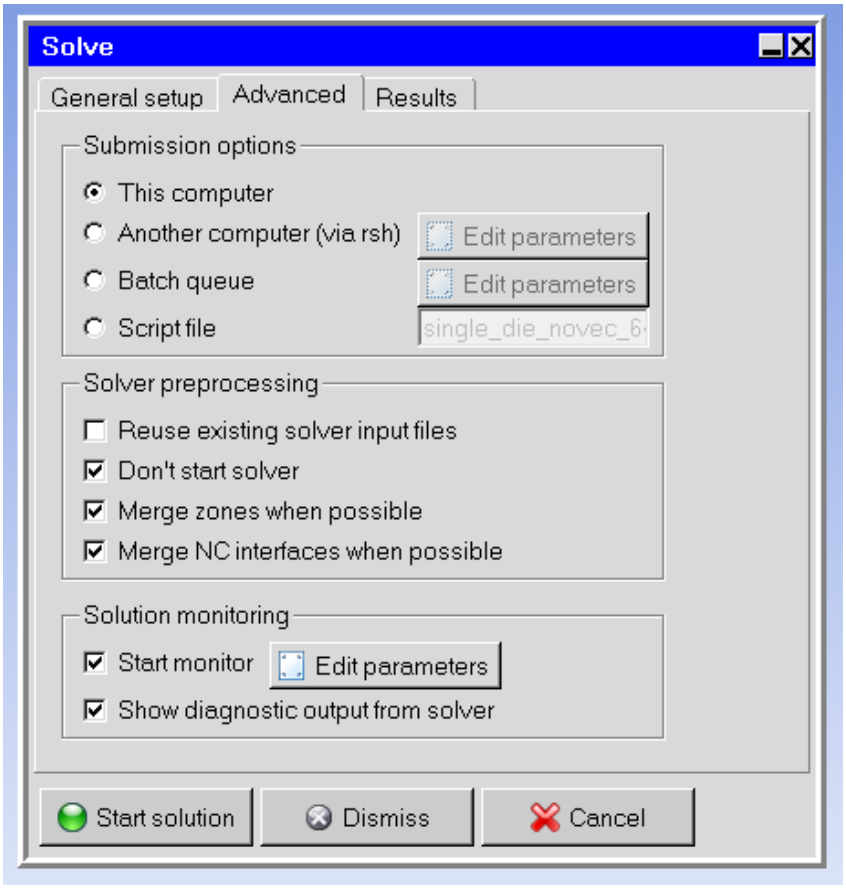

Figure A.6: Solve Window in Icepak

This concludes the description of model creation, mesh generation and case file creation using Icepak 14.0. Again, single phase simulations may be performed by unchecking the box marked “Don’t start solver” in Figure A.6. With the case file successfully created, the next section details importing the case file into Fluent, interpreting user-defined functions and setting the multiphase solver.

A.2 Fluent 14.0

In this section, the procedure to setup multiphase simulations in Fluent using the case file generated from an Icepak model is detailed. First, the prompt upon opening Fluent will be discussed followed by importing the case file. Next, the procedure to interpret, or import, user-defined functions will be described. This section can be skipped if simulations are limited to built-in models. The most detailed section pertains to setting the multiphase solver. Lastly, a brief overview of post processing using another ANSYS product, CFD-Post, will be given.

Upon opening Fluent 14.0, the prompt window shown in Figure A.7 appears. From this window, **Double Precision** should be selected under **Options** and the number of computer cores can be set for parallel processing to reduce computational time.

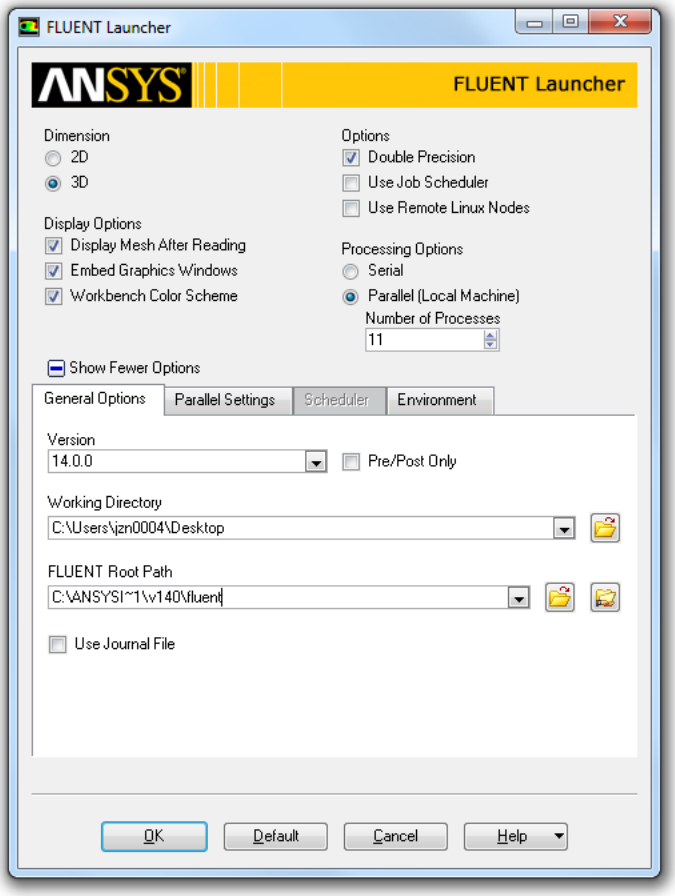

Figure A.7: Fluent 14.0 Launcher Prompt

A.2.1 Importing Case File

After the appropriate options are set in the Fluent launcher window, press **OK** to proceed into Fluent and see the window shown in Figure A.8. Prior to importing a case (.cas) or data (.dat) file into Fluent, the window shown in Figure A.8 appears. There are three primary regions of interest in addition to the usual horizontal menu bar. The left most panel, labeled 1, is where various settings related to the model are defined. In Figure A.8, several of the key parameters are not accessible because a case file has not been imported. The region labeled 2 is an expanded options menu related to whichever parameter is selected from the region labeled 1. Lastly, additional information related to

the model is displayed in the region labeled 3; iterations will appear here during simulations.

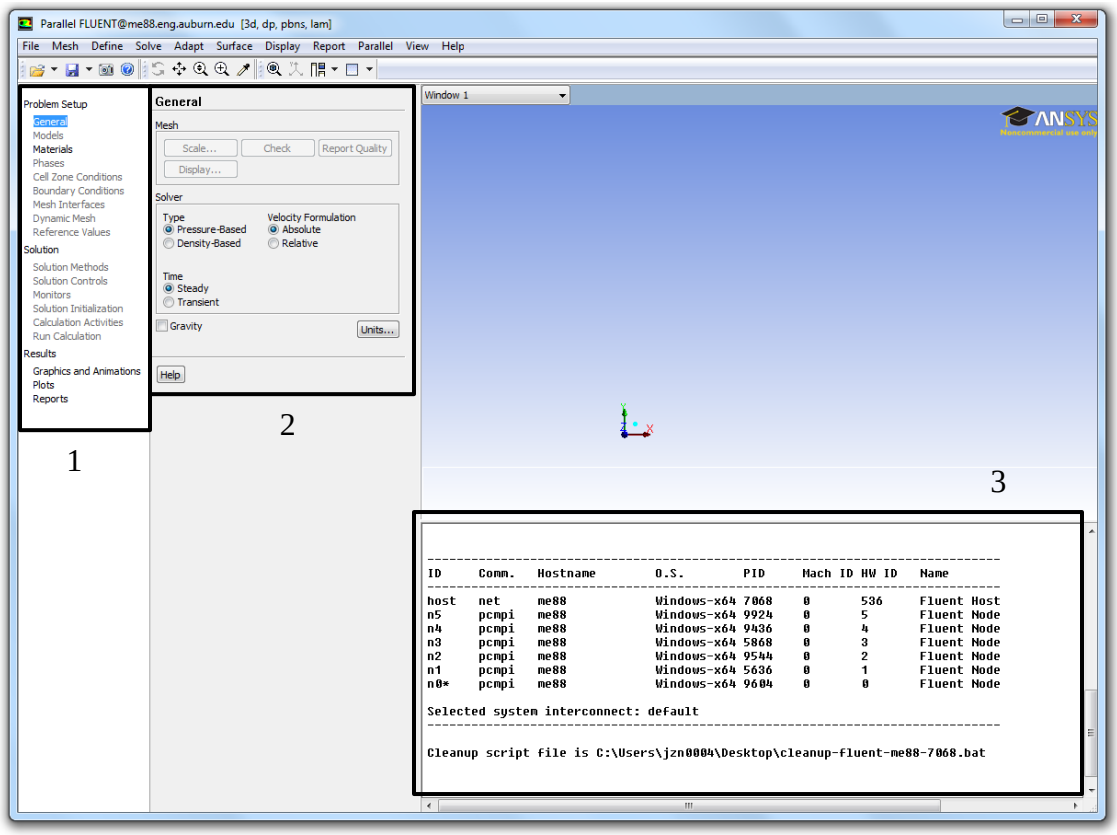

Figure A.8: Fluent 14.0 Window Prior to Importing Case File

A case, data or combination case and data file may be imported from the top menu by selecting **File → Read → Case…** (or Data…, Case & Data…). After loading the model and mesh into Fluent, several options from the left most panel become available based on the case file as shown in Figure A.9; the computational domain for the pool boiling model can also be seen.

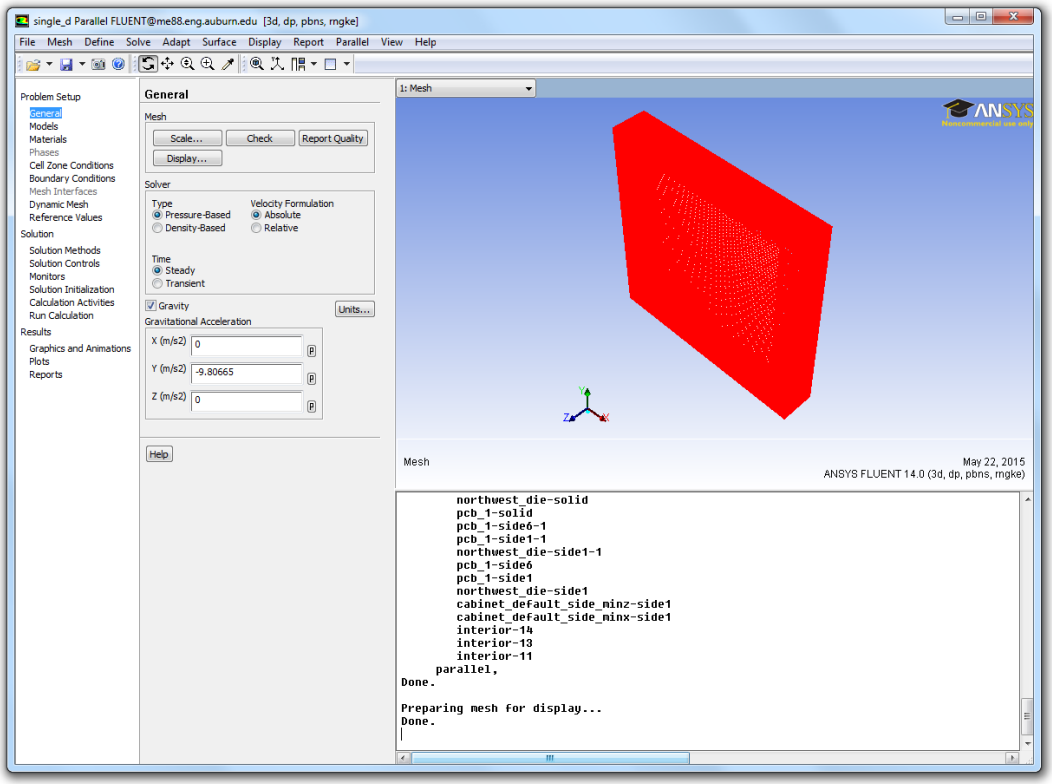

Figure A.9: Pool Boiling Case File Imported into ANSYS Fluent 14.0

It should be noted that the two unavailable options in Figure A.9, **Phases** and **Mesh Interfaces**, will be discussed in a later section. The next section discusses importing, or as Fluent calls the procedure, interpreting user-defined functions (UDFs) into Fluent. This requires a UDF to already be written in C++ code, which can be done in notepad or other simple text editors. The UDFs used in this study are available in Appendix C.

A.2.2 Interpreting User-Defined Functions

If simulations are performed using only built-in functions, this section may be skipped. The application of user-defined functions (UDFs) in Fluent requires two steps, interpreting the source code, a separate text file with the .c file extension, and hooking the UDF to the numerical model. Interpreting a UDF can be done by from the horizontal

menu through **Define → User-Defined → Functions → Interpreted.** This gives the prompt window shown in Figure A.10.

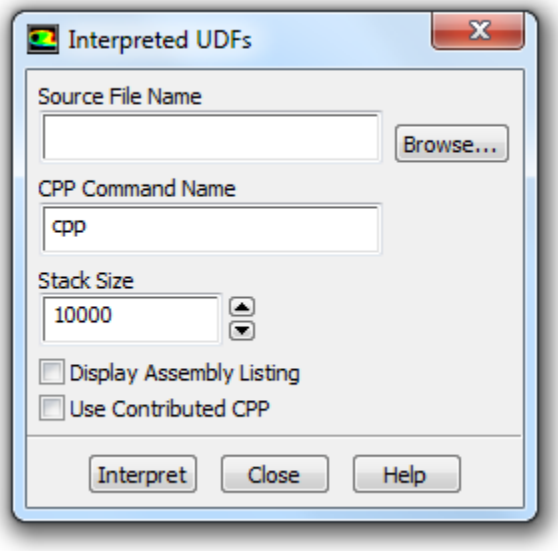

Figure A.10: Prompt Window for Interpreting UDFs

From the prompt in Figure A.10, press **Browse…** and navigate to the chosen UDF. It should be noted that a UDF must be saved in the same folder as the case file and must have the .c file extension. Only one UDF file may be interpreted into the numerical model at a time; however this does not limit the number of default functions in Fluent that can be overridden with a UDF. For example, bubble departure diameter and nucleation site density are two separate boiling functions but both can be replaced by using the same UDF file. See Appendix C for more information on user-defined functions. Once the UDF file is selected, press **Interpret** and wait for Fluent to import the source code. Monitor the command window for error messages related to the UDF. If successful, at this point, the UDF is interpreted but not hooked.

A.2.3 Setting Multiphase Solver and Performing Simulations

After importing the case file and interpreting the UDF (if necessary), the multiphase solvers, in particular the Non-Equilibrium boiling model, and the associated settings need to be specified. The majority of the remainder of this appendix is dedicated to the multiphase settings. Unless stated otherwise, the settings presented in this section were used for both pool and flow boiling simulations.

A.2.3.1 Models

Under the **Models** menu from the left most panel, there are models for multiphase, energy, viscous, radiation, heat exchanger, species, discrete phase, solidification & melting, acoustics and Eulerian wall film. All of these models are off by default for the pool and flow boiling scenarios with the exception of energy and viscous models, which retain the settings from Icepak. Double clicking **Multiphase** opens the window shown in Figure A.11, which has been further expanded to show the Non-Equilibrium boiling model option.

The radio button for the **Eulerian** model should be selected to further show the **Eulerian Parameters** subsection. By selecting the **Boiling Model** under **Eulerian Parameters**, three additional boiling model options appear; these include the RPI, non-equilibrium and critical heat flux boiling models. The Non-Equilibrium boiling model was used nearly exclusively in this study. The other options for scheme and number of Eulerian phases should be left as default. After turning on the multiphase model, a prompt requesting additional property data (for the secondary phase) appears. This allows **Phases** to be selected from the left most panel.

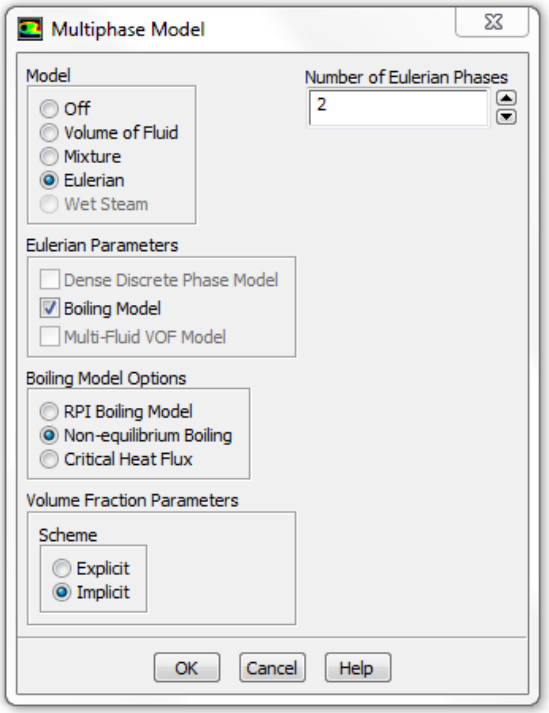

Figure A.11: Multiphase Model Options Window

The viscous model used was the two-equation RNG k-ε model, which should be imported by default if the RNG turbulent model was previously selected in Icepak. By default, the near-wall treatment is based on standard wall functions; however, this study employs non-equilibrium wall functions, which can be accessed by double clicking **Viscou**s. RNG options, model constants and other settings should be left as default.

A.2.3.2 Materials

When the case file is imported into Fluent, the fluid properties, such as those for liquid Novec 649, defined in Icepak are also imported and applied to the numerical model. However, the vapor properties for Novec 649 need to be defined. After selecting **Materials** from the left most panel and double clicking novec_649, the window in Figure A.12 appears for liquid Novec 649 along with its properties.

To create vapor Novec 649 in the numerical model, change the name from "novec_649" to "novec_649_vapor" and press **Change/Create** at the bottom. A prompt asking to overwrite the existing liquid Novec 649 appears. Press **NO**. This will then copy the properties for liquid Novec 649 into a new definition, "novec_649_vapor" that can be modified per vapor properties. Table A.1 lists the liquid and vapor properties for Novec 649. In Figure A.12, all properties for liquid Novec 649 are constant except for density, which is based on the **boussinesq** approximation. When defining the density for vapor Novec 649, the **boussinesq** approximation should be changed to **constant**.

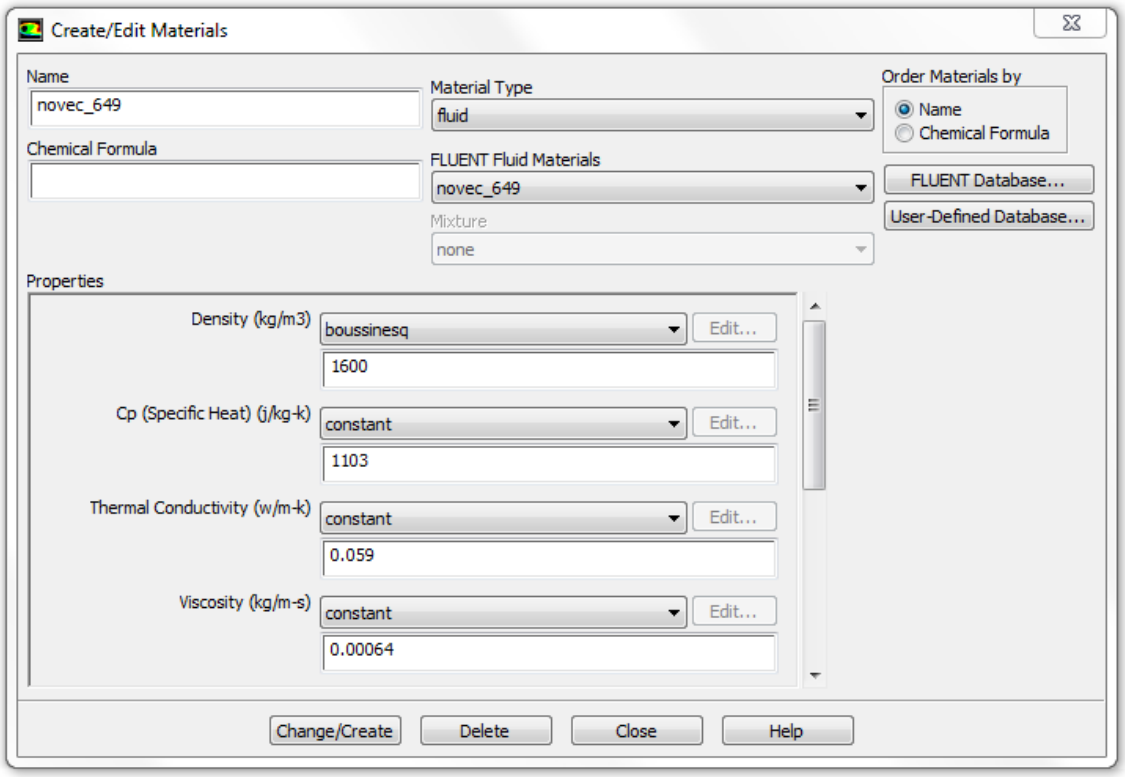

Figure A.12: Create/Edit Materials Window

Table A.1: Liquid and Vapor Properties for Novec 649

Property	Liquid	Vapor
Density (kg/m^3)	1600	5.56
Specific Heat (J/kg·K)	1103	906.4
Thermal Conductivity (W/m·K)	0.059	0.00582
Viscosity (kg/m·s)	0.00064	1.84147×10^{-7}
Standard State Enthalpy (J/kg·mol)	-	2.7808×10^{7}
Thermal Expansion Coefficient (K^{-1})	0.0018	-

When selecting **Materials** from the left most panel, both fluid and solid materials appear; however, the properties for the solid materials were previously defined in Icepak and therefore no changes were made to them in Fluent.

A.2.3.3 Phases

When selecting **Phases** from the left most panel, the two Eulerian phases appear in the adjacent panel for phase 1 (primary) and phase 2 (secondary). By default, phase 1 is set to the fluid imported from Icepak, which in the simulations for this study is the liquid Novec 649. Phase 2 also defaults to liquid Novec 649 and must be changed by double clicking on **phase-2 – Secondary Phase** to open another window. In this window, two changes need to be made. First, the **Phase Material** needs to be changed from "novec_649" to "novec_649_vapor" and secondly, the diameter model should be changed from **constant** to **sauter-mean**. Press **OK** to save the changes.

Also appearing under **Phases** is setting for the interaction between phases, which can be accessed by selecting **Phases** from the left most panel then clicking **Interaction…** from the adjacent panel, which generates the prompt shown in Figure A.13.

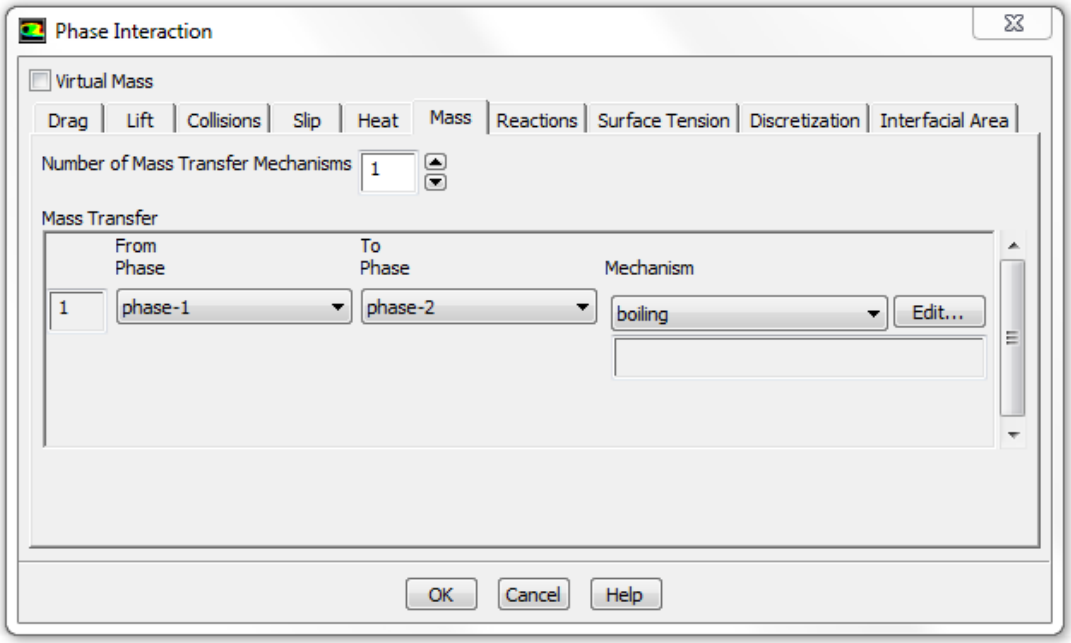

Figure A.13: Phase Interaction Window

The **Phase Interaction** window shown in Figure A.13 may appear differently in other versions of ANSYS Fluent. For example, additional interactions may be included while some of the interactions shown in Figure A.13 may be omitted. For the multiphase simulations used in this study with ANSYS Fluent 14.0, the phase interaction models shown in Table A.2 were selected.

Table A.2: Phase Interaction Models used in ANSYS Fluent 14.0 Multiphase Solver

Drag	boiling-ishii
Lift	boiling-moraga
Collisions	N/A
Slip	N/A
Heat	ranz-marshall
Mass	See Below
Reactions	N/A
Surface Tension	constant – 0.00922249 N/m
Discretization	N/A
Interfacial Area	ia-symmetric (default)

For more information on the phase interaction models used in this study and the reason for their selection over other phase interaction models, see Chapter 3.

For the phase interaction for mass transfer, the number and mechanism needs to be selected. This is where the boiling parameters for the RPI and Non-Equilibrium boiling models can be modified or set to user-defined functions. For the two phase models, the number of mass transfer interactions is 1 and the mass transfer must be changed to reflect from **phase-1** to **phase-2** as shown in Figure A.13. Next to **Mechanism**, pressing **Edit…** opens the window for the boiling model options shown in Figure A.14, which includes the saturation temperature and the four boiling parameters (bubble departure diameter, frequency of bubble departure, nucleation site density and area influence coefficient) set to their respective default built-in functions. By default, the saturation temperature is set to that of water, 373.15 K, and must be changed to the 322.15 K for Novec 649.

At this point, if a user-defined function (UDF) for any of the boiling parameters was previously interpreted into the model, it can be set (or hooked per the terminology in Fluent) to the associated parameter by clicking the dropdown menu, selecting **user-defined** and choosing the appropriate UDF name if multiple functions were included in the same .c file. The interfacial model constants and bubble waiting time coefficient should be left as the default values. Press **OK** to save the changes.

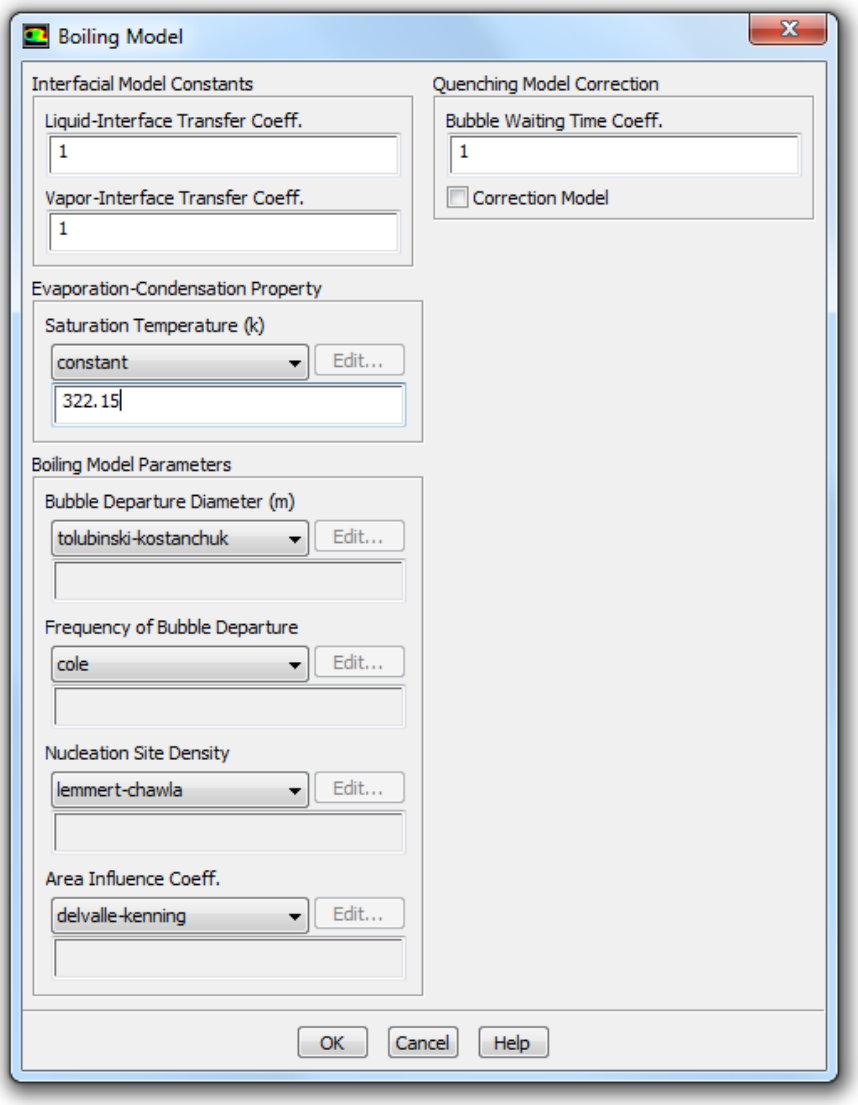

Figure A.14: Boiling Model Options Available from the Mass Tab of Phase Interaction

A.2.3.4 Cell Zone Conditions

In the pool boiling numerical model, there are three cell zones for the fluid, die and printed circuit board. There are significantly more for the flow boiling model as the duct was defined using several blocks and each block corresponds to at least one cell zone. Regardless, if the heat per die was defined in Icepak when the block representing the silicon die was created, then no changes need to be made to the cell zone conditions

for the initial simulations. It should be noted that heat is defined in Icepak in terms of Watts while Fluent converts it to a volumetric generation in W/m^3 based on the die geometry. For example, 3 W/cm^2 corresponds to a volumetric generation of 5×10^7 W/m^3 based on the die dimensions in the pool boiling models. It should also be noted that once the initial Icepak model is created and the corresponding case file is imported into Fluent, changes to the die heat rate can be made from Fluent.

To make these changes, select **Cell Zone Conditions** from the left most panel and then double click the die of interest in the adjacent panel. This opens another window in which the **Source Terms** tab should be selected and then **Edit…** next to the energy term. These windows can be seen in Figure A.15.

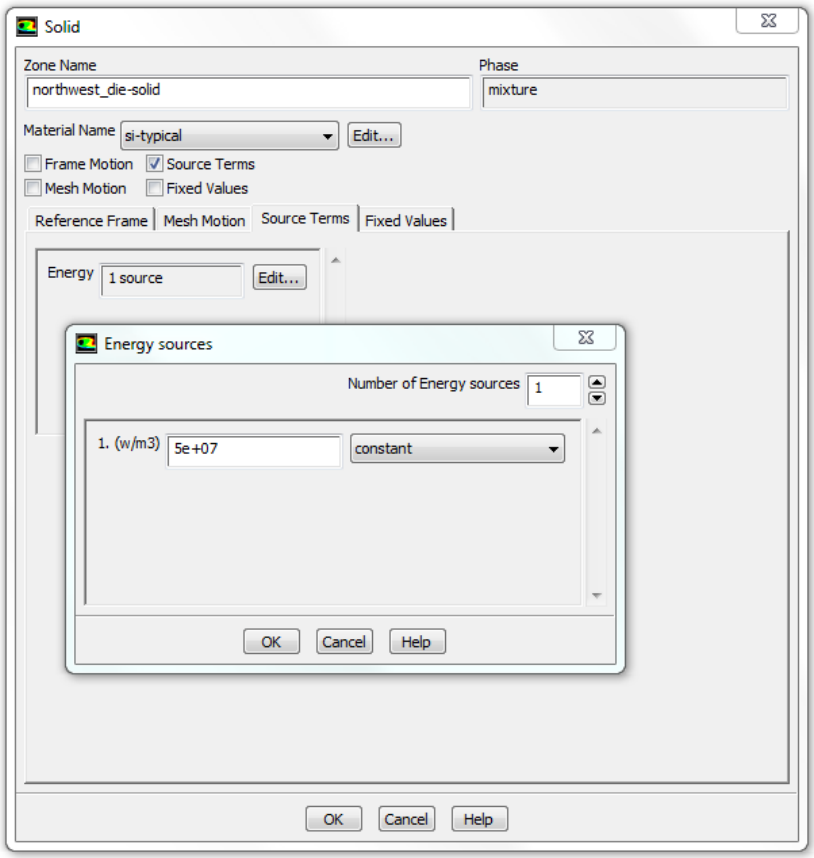

Figure A.15: Energy Sources Window to Define New Volumetric Heat Generation

It should be noted that in the two phase models used in this study, Fluent actually introduces a total of three phases (mixture, phase-1 and phase-2). This is significant because changes to the die heat rate or volumetric generation must be made to all three phases to ensure a previous heat rate is fully overridden. The different phases can be accessed by selecting **Cell Zone Conditions** on the left most panel, then selecting the zone of interest in the adjacent panel. At the bottom of the adjacent panel, the three phases can be switched between.

The next two multiphase settings are **Boundary Conditions** and **Mesh Interfaces**. These are both model and situation dependent. For **Boundary Conditions**, no changes needed to be made for the pool boiling simulations in this study; however, in some situations with flow boiling options within **Boundary Conditions**, specifically the turbulence settings, needed to be modified for the solution to converge. For **Mesh Interfaces**, only non-conformal meshes, such as the one used in flow boiling, require interfaces to be defined. For the pool boiling simulations, which used a conformal grid, **Mesh Interfaces** is unavailable and that section may be skipped.

A.2.3.5 Boundary Conditions

For the pool boiling simulations, the settings under **Boundary Conditions** did not need to be modified. There are zones associated with the cabinet, fluid (denoted "interior" in Fluent), die and printed circuit board for the pool boiling models; there are similar zones for the flow boiling models.

With numerical simulations involving the more complex flow boiling model, the **Boundary Conditions** may need to be modified for convergence. In general, the first simulations of any trial were performed without modifying the settings within **Boundary**

Conditions; however, if instabilities prevented the solution from converging, then the turbulence settings were modified. Typically only the backflow turbulent intensity needed to be changed; specifically, the default backflow intensity of 10% was determined to be too high and values in the range of 2 to 5% eliminated solution instabilities. The turbulent settings can be accessed by selecting **Boundary Conditions** from the left most panel, then selecting the zones corresponding to the cabinet in the adjacent panel and finally pressing **Edit…** with the mixture phase selected. This generates the window shown in Figure A.16.

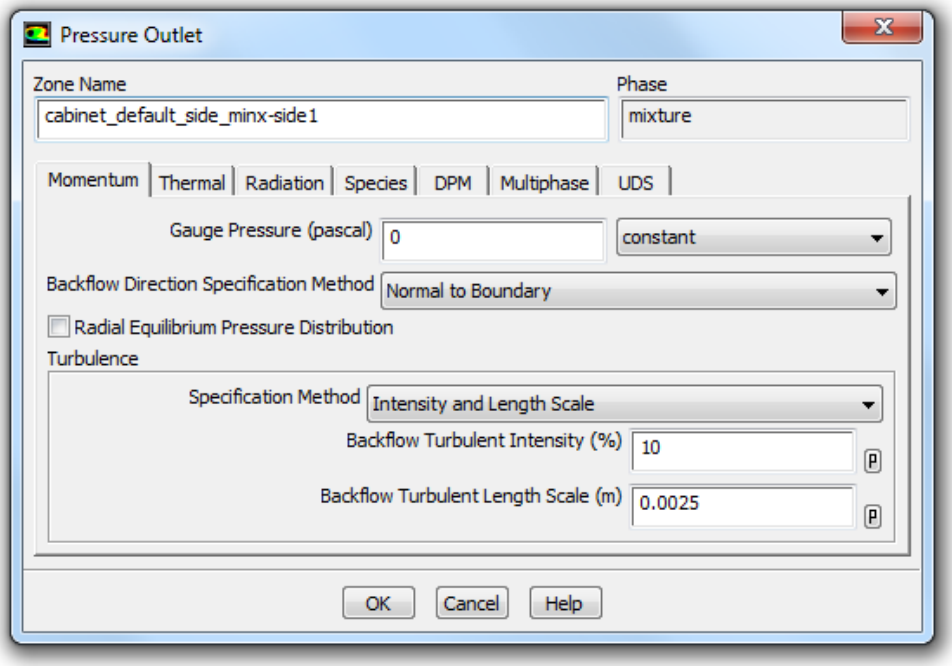

Figure A.16: Backflow Turbulent Intensity Settings for the Cabinet Available from the Boundary Condition Settings

Fincher [13] also calls attention to situations involving a pressure outlet boundary condition in which the backflow temperatures for both liquid and vapor phases default to the primary phase temperature; the secondary phase backflow temperature should be changed accordingly when using multiphase models to prevent numerical instabilities.

These options can be accessed similar to the turbulence setting; however, instead of selecting the **mixture** phase, **phase-2** should be selected. As mentioned previously, the settings within **Boundary Conditions** did not need to be modified for pool boiling simulations and only occasionally were modified for flow boiling when instabilities prevented convergence.

A.2.3.6 Mesh Interfaces

Mesh Interfaces only need to be considered when a non-conformal mesh is used. For the pool boiling simulations used in this study, a conformal mesh was used; therefore, this section can be skipped when considering pool boiling simulations. However, a non-conformal mesh was used in the flow boiling cartridge model. If mesh interfaces are not defined, the simulation will not begin. To access the **Create/Edit Mesh Interfaces** window shown in Figure A.17, select **Mesh Interfaces** from the left most panel then click **Create/Edit** in the adjacent panel.

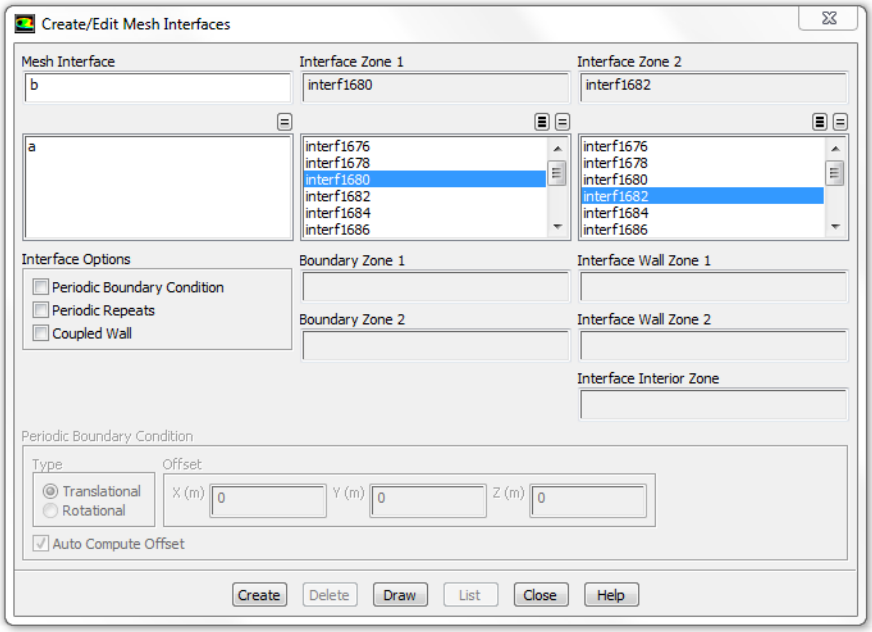

Figure A.17: Create/Edit Mesh Interfaces Window

To create a mesh interface, one interface from **Zone 1** must be matched with the appropriate interface from **Zone 2** and this is repeated until all interfaces are paired; the flow boiling models had 6 pairs of mesh interfaces, labeled a through f. In general, the related interfaces are sequentially numbered. For example, in Figure A.17, "interf1676" and "interf1678" is an appropriate pair. In order to check that the proper interfaces are being merged, the **Draw** option at the bottom should be used. Select one interface from **Zone 1** and press **Draw** to display it. Unselect the interface from **Zone 1,** select a different interface from **Zone 2**, press **Draw** and an appropriate pair will display the same or similar interface. Once a pair of mesh interfaces has been identified, input a name (letters a through f were chosen) and press **Create**. Repeat until all interfaces have been paired exactly once then press **Close** to return to the model.

A.2.3.7 Solution Methods

For the solution methods, select the **Coupled** scheme under **Pressure-Velocity Coupling** and check **the Coupled with Volume Fractions** option. The spatial discretization should be left as the default selection, i.e. least squares cell based for gradient and first order upwind for the other parameters (momentum, volume fraction, turbulent kinetic energy, turbulent dissipation rate and energy). If higher order accuracy is desired, second order options are also available.

A.2.3.8 Solution Controls

The solution controls include the flow Courant number, a set of explicit relaxation factors for momentum and pressure and a set of under-relaxation factors for density, body forces, vaporization mass, volume fraction, turbulent kinetic energy, turbulent dissipation

rate, turbulent viscosity and energy. Table A.3 lists the solution control parameters along with the default values, suggested range and initial values.

Table A.3: Solution Control Parameters with Default and Suggested Values

Parameter	Default	Suggested	Initial
flow Courant number	200	1 – 20	10
momentum	0.75	0.2 – 0.8	0.55
pressure	0.75	0.1 – 0.4	0.25
density	1	0.25 – 0.8	0.6
body forces	1	0.25 – 0.8	0.6
vaporization mass	1	0.25 – 0.8	0.6
volume fraction	0.5	0.25 – 0.8	0.6
turbulent kinetic energy	0.5	0.25 – 0.8	0.3
turbulent dissipation rate	0.5	0.25 – 0.8	0.3
turbulent viscosity	1	0.25 – 0.8	0.3
energy	1	0.25 – 0.8	0.6

For pool and flow boiling simulations, converged solutions were achieved using the initial set of solution control values in general; however, pressure and momentum were decreased on occasion when the solution became unstable especially at higher heat rates or flow velocities. To further improve solution stability, the **bi-conjugate-gradient stabilizer (BCGSTAB)** was used. This can be accessed by selecting **Solution Controls** from the left most panel, then clicking **Advanced…** from the adjacent panel and selecting **BCGSTAB** from the dropdown menu under **Stabilization Method**.

A.2.3.9 Monitors

By default, there is only one monitor (for residuals) active to view solution convergence and the absolute criteria are typically not set to a sufficiently small value. To adjust the convergence criteria, select **Monitors** from the left most panel, then select **Residuals – Print, Plot** and click **Edit…** to access the **Residual Monitors** window. Absolute convergence criteria can be modified for 12 variables; these include continuity,

velocity for both phases and all three directions, energy for both phases, turbulent kinetic energy (k), turbulent dissipation rate (ε) and volume fraction for phase 2. The absolute criteria for continuity and both turbulent terms are set to 10^{-7} by default; however, all other terms are set to 0.001 and need to be reduced to 10^{-7} as well. Due to residual oscillations and the complex nature of multiphase boiling, all of the 12 residuals are unlikely to reach 10^{-7}. For the pool and flow boiling simulations in this study, all residuals reached a minimum of 10^{-5} with liquid phase velocity residuals typically lower than 10^{-6} and energy residuals typically lower than 10^{-7}.

In addition to monitoring the residuals, surface monitors were also created. For pool boiling simulations, one surface monitor was created for the single die while four surface monitors were created for flow boiling with each monitor corresponding to one of the die in the cartridge model. The surface monitors were typically tracking an average die temperature over all iterations. Once all of the residuals had reached a sufficiently low value and the change in temperature from one iteration to the next was less than 0.01°C for over 250 iterations, the solution was deemed converged. To create a temperature surface monitor, select **Monitors** from the left most panel, then click **Create…** under **Surface Monitors** in the adjacent panel. The window in Figure A.18 appears. In order to view the temperature monitor, check the **Plot** option. To use the same monitor as the ones in this study, change the **Report Type** to **Area-Weight Average**, change the **Field Variable** to **Temperature…** and select the appropriate objects under **Surfaces**. The window shown in Figure A.18 is representative of the temperature surface monitor for one die; repeat as necessary. It should be noted that by default the additional

monitors are displayed on separate plot windows. Multiple surface monitors can be displayed on the same plot window by changing the window number if desired.

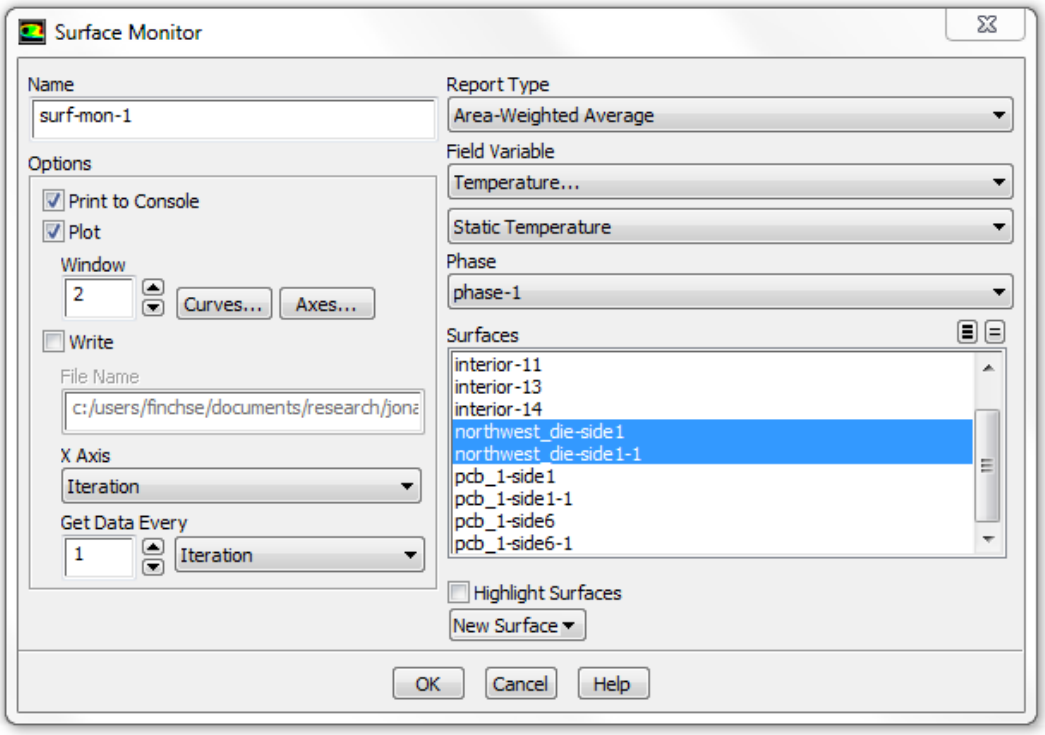

Figure A.18: Surface Monitor Window to Create Temperature Monitors

A.2.3.10 Solution Initialization

For solution initialization, the default standard initialization method is sufficient. Several variables appear when **Solution Initialization** is selected from the left most panel; however, many can be left at the default value with the exception of turbulent kinetic energy, phase-1 temperature and phase-2 temperature. The default values for turbulent kinetic energy (TKE) and turbulent dissipation rate (TDR) are 1 m^2/s^2 and 1 m^2/s^3, respectively; however, the TKE value is too high for the length scales in both pool and flow boiling. TKE was set to an initial value of 0.0001 m^2/s^2 in pool boiling and 0.001 m^2/s^2 in flow boiling while TDR was left at the default value.

The phase-1 and phase-2 temperatures are both set to 300 K by default; however, these also need to be adjusted. The phase-1 temperature should be set to the bulk liquid fluid temperature and the phase-2 temperature should be set to the saturation temperature of Novec 649 (322.15 K). Once these values have been adjusted, press **Initialize**.

A.2.3.11 Run Calculation

The last item before a simulation may begin is setting the number of iterations. This may be accessed by selecting **Run Calculation** from the left most panel. Set the number of iterations to a sufficiently large number and press **Calculate** to begin the simulation. Typically, 3000-4000 iterations were set for the initial simulation. For pool boiling simulations where the heat flux varied from 3 W/cm^2 to 6 W/cm^2 to 9 W/cm^2, approximately 3500 iterations were required to sufficiently converge the 3 W/cm^2 case and then 1500-2000 iterations were required to converge the subsequent heat fluxes. When the solution has sufficiently converged press **File → Write → Case & Data…** from the menu across the top.

A.3 CFD-Post 14.0

Once the solution has converged and the data file has been saved, post processing can be done using several methods and software packages. Post processing includes generating contour plots for temperature, velocity and other variables of interest as well as recording the converged die surface temperatures. While Icepak and Fluent have post processing options available within those software packages, it was determined that ANSYS CFD-Post 14.0 provided a cleaner user interface and provided more options regarding post processing.

Upon opening CFD-Post 14.0, the graphical user interface shown in Figure A.19 appears. Solution data files may be loaded into CFD-Post from **File → Load Results…** The interface is very similar to Icepak; for the purposes of post processing, two regions of shortcuts are particularly relevant. In Figure A.19, the region labeled 1 has shortcuts for creating vector, contour, streamline and particle trace plots while the region labeled 2 has shortcuts to quickly change the orientation.

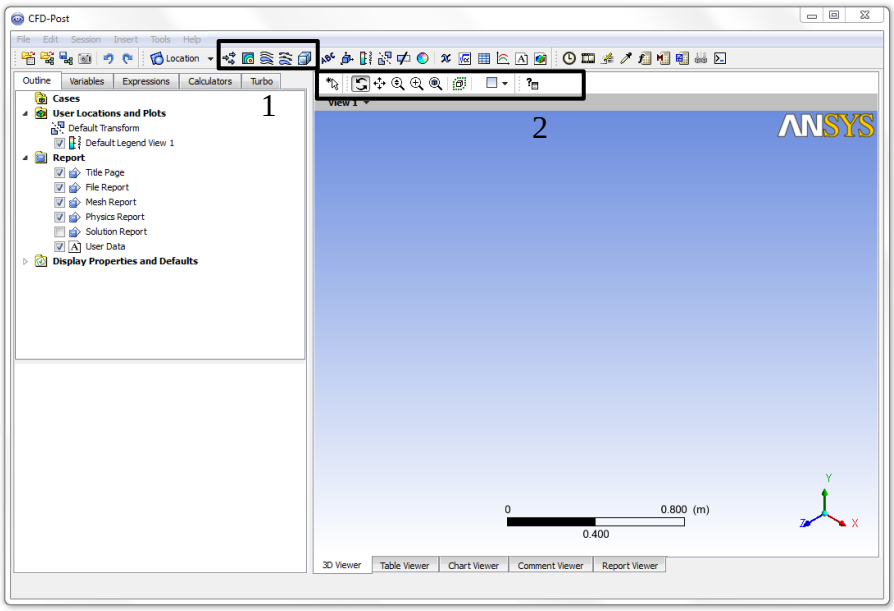

Figure A.19: ANSYS CFD-Post 14.0 Graphical User Interface

After loading a data file into CFD-Post, a wireframe of the numerical model appears in the main window while the components, such as the die and printed circuit board, populate the left most panel. For both the pool and flow boiling models, the maximum die surface temperature is of interest; these temperatures were found by applying a temperature contour plot to the die and printed circuit board (PCB). After pressing **Contour** from region 1 in Figure A.19, the options shown in Figure A.20 become available at the bottom of the left most panel. The "…" next to **Locations** should be pressed to show all components in the model and then all of the die and PCB components should be selected. The **Variable** should be changed to **Phase 1. Temperature** and the **# of Contours** should be set to a reasonably high number for the best resolution.

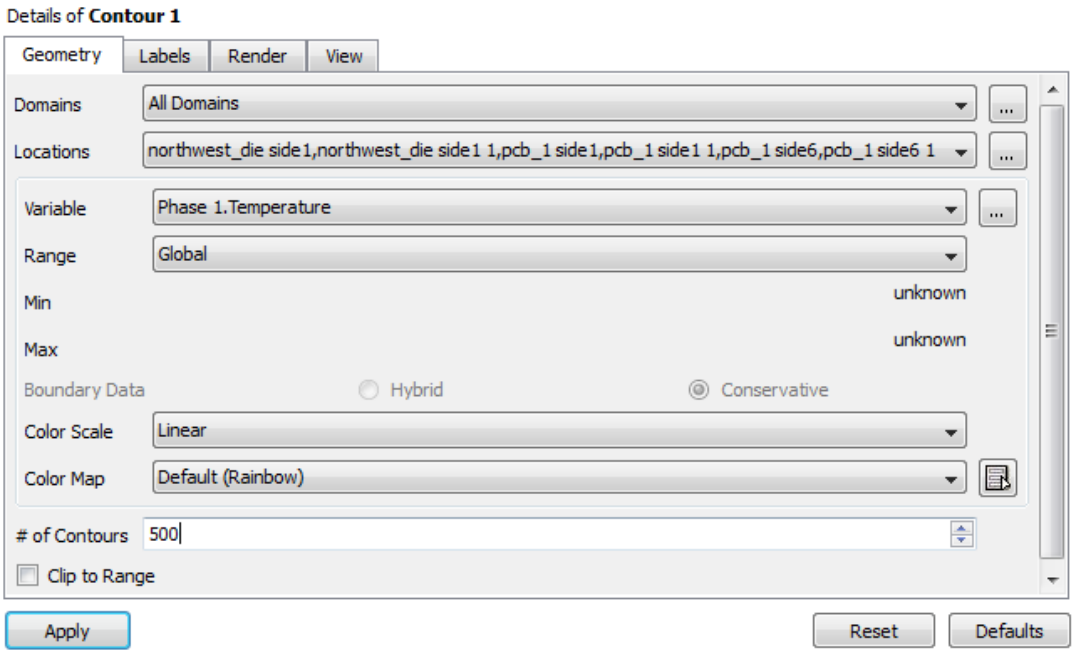

Figure A.20: Contour Plot Options Panel

After the temperature contour plot has been generated, the maximum die surface temperature can be recorded in Excel for further data processing. A similar procedure can be used to generate particle traces and vector plots. On occasion, a contour on a plane perpendicular to the surface of the die and PCB may be desired. To do this, the plane must be inserted into the model using the menu at the top, **Insert → Location → Plane** then the orientation and location of the plane can be supplied. For a temperature contour on a perpendicular plane, the same procedure as detailed above is followed except rather than selecting the die and PCB as the **Locations**, the plane is selected.

This concludes Appendix A in which the three software packages used in this study (ANSYS Icepak, Fluent and CFD-Post) were discussed in detail. As a quick summary, Icepak was used to create the numerical models and generate the mesh, Fluent was used to setup multiphase solvers and perform the calculations and CFD-Post was used to generate contour plots and extract the solution results.

Appendix B

NSD AND BDD USER-DEFINED FUNCTIONS

In this appendix, the user-defined functions for nucleation site density (NSD) and bubble departure diameter (BDD) used in this study are presented. First, the functional forms of the nucleation site density and bubble departure diameter functions are repeated followed by tables containing the coefficients needed to reproduce the simulated functions, including the Reference and Fluent Default coefficients along with the user-defined coefficients. The equation form for the nucleation site density user-defined functions is given by Eq. (B.1),

$$N_w = C_1(T_w - T_{sat})^{C_2} \tag{B.1}$$

where N_w is the nucleation site density in m^{-2}, T_w and T_{sat} are the wall and saturation temperatures in °C or K, respectively, and C_1 and C_2 are constants. Table B.1 summarizes the coefficients needed to replicate the NSD user-defined functions. The equation form for the bubble departure diameter user-defined functions is given by Eq. (B.2),

$$D_w = (C_3)e^{-C_4(T_{sat}-T_{pool})} \tag{B.2}$$

where D_w is the bubble departure diameter in meters, T_{sat} and T_{pool} are the saturation and bulk liquid pool temperatures in °C or K, respectively, and C_3 and C_4 are constants. The "Fluent Default" for bubble departure diameter is not the same as the "Fluent Default" for

nucleation site density. Table B.2 summarizes the coefficients needed to replicate the BDD user-defined functions. The coefficients for the first set of NSD functions were based on Reference [25]. For example, NSD: 1a, 2a and 3a share the same C_1 as the Reference [25] function while NSD: 1b, 2b and 3b share the same C_2. The second set of NSD coefficients was based on observations of numerical results that used the first set of NSD functions. For BDD, C_3 of the α-functions was based on experimental data while C_4 of the β-functions was based on Reference [26] and the Fluent Default, Eq. (4.12).

Table B.1: Summary of Coefficients for Nucleation Site Density Functions

Function	$\mathbf{C_1}$ $(\mathbf{m^{-2}K^{-C_2}})$	$\mathbf{C_2}$ $(-)$
Reference [25]	31.1	4.5
Fluent Default, Eq. (4.11)	15,500	1.8
1a	31.1	3.5
2a	31.1	4.0
3a	31.1	5.0
1b	1	4.5
2b	10	4.5
3b	100	4.5
1a_2	225	2.5
2a_2	15	3.5
3a_2	0.15	5.2
1b_2	0.1	4.5
2b_2	0.5	4.5
3b_2	5	4.5

Table B.2: Summary of Coefficients for Bubble Departure Diameter Functions

Function	$\mathbf{C_3 \times 10^3}$ $\mathbf{(m)}$	$\mathbf{C_4}$ $\mathbf{(K^{-1})}$
Reference [26]	1.32	0.02
Fluent Default, Eq. (4.12)	0.60	0.02
1α	0.52	0.01
2α	0.52	0.03
3α	0.52	0.05
1β	1.4	0.02
2β	1.2	0.02
3β	1.0	0.02

Appendix C

SOURCE CODE FOR NSD AND BDD USER-DEFINED FUNCTIONS

In this appendix, the source code used to implement user-defined functions for nucleation site density (NSD) and bubble departure diameter (BDD) into the multiphase solver of Fluent 14.0 is presented. The source code was written in notepad and saved with a .c file extension. The same source code can be used for both pool and flow boiling simulations; however, the source code (.c file) must be in the same folder as the case file.

Each UDF used in ANSYS Fluent begins with #include "udf.h" to incorporate a library of pre-defined macros, termed "DEFINE macros." There are hundreds of DEFINE macros organized into categories, such as general purpose, model-specific and multiphase only. In this study, the DEFINE_BOILING_PROPERTY macro is used in every UDF and occasionally multiple times in the same UDF. Each instance of DEFINE_BOILING_PROPERTY allows any one of the built-in functions for area of influence, frequency of bubble departure, bubble departure diameter or nucleation site density to be replaced with the function written in the UDF. With the exception of inputting a unique name to identify the macro in Fluent, the other eight arguments are fixed based on the macro and has this form: **DEFINE_BOILING_PROPERTY(name, f, t, c0, t0, from_index, from_species_index, to_index, to_species_index).** Table C.1 describes each of the arguments passed from Fluent into the UDF.

Table C.1: DEFINE_BOILING_PROPERTY Macro Arguments

name	name chosen to identify the macro in Fluent
f	index that identifies a wall face
t	pointer to the wall face thread
c0	cell index that identifies the cell next to the wall
t0	pointer to the mixture-level cell thread
from_index	liquid phase in boiling models
from_species_index	ID of liquid species
to_index	vapor phase in boiling models
to_species_index	ID of vapor species

There were four primary source code files for NSD only, BDD only, combination of NSD and BDD, and the nonlinear NSD function (which also included a BDD UDF). Simple modifications to the source code files, typically changes to 2-4 lines, were done to change from one NSD function to the next or one BDD function to the next.

The source code presented in Section C.1 will replace the built-in nucleation site density function with NSD: 1a where the variables "lead_coefficient" and "exponent" refer to the coefficients C_1 and C_2, respectively. There will not be an option to replace the bubble departure diameter using the code in Section C.1. Conversely, the source code in Section C.2 will replace the built-in bubble departure diameter function with BDD: 1α but does not supply a user-defined function for nucleation site density. The variables "bdd_coeff" and "bdd_exponent" refer to C_3 and C_4, respectively. The source code presented in Section C.3 will allow both NSD and BDD to be replaced by NSD: 1b and BDD: 1α, respectively. The source code given in Section C.4 will replace the built-in NSD function with the piecewise nonlinear equation given by Eq. (4.21) and will replace the built-in BDD function with BDD: 1α.

C.1 Source Code for Nucleation Site Density Only

```
#include "udf.h"
#define lead_coefficient 31.076
#define exponent 3.5
DEFINE_BOILING_PROPERTY(NSD_1a,f,t,c0,t0,from_index,from_species_index,to_i
ndex,to_species_index)
{
real temp_sat, temp_wall, delta_T, correlation_factor, calculated_temp_raised_to_power,
nsd;
temp_sat = C_STORAGE_R(c0,t0,SV_SAT_TEMPERATURE);
temp_wall = F_T(f,t);
delta_T = temp_wall - temp_sat;
correlation_factor = pow(lead_coefficient,1);
calculated_temp_raised_to_power = pow(delta_T,exponent);
nsd = correlation_factor*calculated_temp_raised_to_power;
return nsd;
}
```

C.2 Source Code for Bubble Departure Diameter Only

```
#include "udf.h"
#define bdd_coeff 0.00052
#define bdd_exponent 0.01
DEFINE_BOILING_PROPERTY(BDD_1a,f,t,c0,t0,from_index,from_species_index,to_
index,to_species_index)
{
real diam_b, subcool;
int liq_phase = from_index;
Thread **pt0 = THREAD_SUB_THREADS(t0);
real T_SAT = C_STORAGE_R(c0,t0,SV_SAT_TEMPERATURE);
real T_l = C_T(c0, pt0[liq_phase]);
subcool = T_SAT - T_l;
```

```
diam_b = bdd_coeff*exp(-bdd_exponent*subcool);
return diam_b;
}
```

C.3 Source Code for Combinations of NSD and BDD

```
#include "udf.h"
#define bdd_coeff 0.00052
#define bdd_exponent 0.01
#define nsd_coeff 1
#define nsd_exponent 4.5076
DEFINE_BOILING_PROPERTY(BDD_1a,f,t,c0,t0,from_index,from_species_index,to_
index,to_species_index)
{
real diam_b, subcool;
int liq_phase = from_index;
Thread **pt0 = THREAD_SUB_THREADS(t0);
real T_SAT = C_STORAGE_R(c0,t0,SV_SAT_TEMPERATURE);
real T_l = C_T(c0, pt0[liq_phase]);
subcool = T_SAT - T_l;
diam_b = bdd_coeff*exp(-bdd_exponent*subcool);
return diam_b;
}
DEFINE_BOILING_PROPERTY(NSD_1b,f,t,c0,t0,from_index,from_species_index,to_i
ndex,to_species_index)
{
real temp_sat, temp_wall, delta_T, correlation_factor, calculated_temp_raised_to_power,
nsd;
temp_sat = C_STORAGE_R(c0,t0,SV_SAT_TEMPERATURE);
temp_wall = F_T(f,t);
delta_T = temp_wall - temp_sat;
correlation_factor = pow(nsd_coeff,1);
```

```
calculated_temp_raised_to_power = pow(delta_T,nsd_exponent);
nsd = correlation_factor*calculated_temp_raised_to_power;
return nsd;
}
```

C.4 Source Code for Piecewise Nonlinear Nucleation Site Denisty

```
#include "udf.h"
#define bdd_coeff 0.00052
#define bdd_exponent 0.05
#define lead_coefficient_1 225
#define exponent_1 2.5
#define lead_coefficient_2 0.0000067
#define exponent_2 7.885
DEFINE_BOILING_PROPERTY(BDD_3a,f,t,c0,t0,from_index,from_species_index,to_
index,to_species_index)
{
real diam_b, subcool;
int liq_phase = from_index;
Thread **pt0 = THREAD_SUB_THREADS(t0);
real T_SAT = C_STORAGE_R(c0,t0,SV_SAT_TEMPERATURE);
real T_l = C_T(c0, pt0[liq_phase]);
subcool = T_SAT - T_l;
diam_b = bdd_coeff*exp(-bdd_exponent*subcool);
return diam_b;
}
DEFINE_BOILING_PROPERTY(NSD_nonlinear_1c,f,t,c0,t0,from_index,from_species
_index,to_index,to_species_index)
{
real temp_sat, temp_wall, delta_T, correlation_factor_1,
calculated_temp_raised_to_power_1, correlation_factor_2,
calculated_temp_raised_to_power_2, nsd;
```

```
temp_sat = C_STORAGE_R(c0,t0,SV_SAT_TEMPERATURE);
temp_wall = F_T(f,t);
delta_T = temp_wall - temp_sat;
if (delta_T < 25)
{
correlation_factor_1 = pow(lead_coefficient_1,1);
calculated_temp_raised_to_power_1 = pow(delta_T, exponent_1);
nsd = correlation_factor_1*calculated_temp_raised_to_power_1;
}
else
{
delta_T >= 25;
correlation_factor_2 = pow(lead_coefficient_2,1);
calculated_temp_raised_to_power_2 = pow(delta_T, exponent_2);
nsd = correlation_factor_2*calculated_temp_raised_to_power_2;
}
return nsd;
}
```

Appendix D

TWO PHASE SIMULATION RESULTS

In this appendix, results from both pool boiling of the single die model and flow boiling of the four die cartridge model are provided in tabular form. Plots of heat flux as a function of subcooled temperature difference were generated from data in these tables.

D.1. Pool Boiling Numerical Results

This section includes the numerical results from pool boiling simulations of the single die in Novec 649. Results include the parametric study for the built-in boiling parameters (Table D.1), the parametric study for user-defined nucleation site density (NSD) functions (Table D.2), the parametric study for user-defined bubble departure diameter (BDD) functions (Table D.3), combinations of NSD and BDD (Table D.4), piecewise nonlinear NSD (Table D.5), variation of degree of subcooling (Table D.6) and variation of the turbulence model (Table D.7). In the tables, N.S. stands for Not Simulated.

Table D.1: Numerical Results for Built-In Boiling Parameters (Case A to D)

Case A

$q'' \ (W/cm^2)$	ΔT_{pool} (K)
3	21.55
5	23.65
7	25.35
8	26.45
9	28.95

Case B

$q'' \ (W/cm^2)$	ΔT_{pool} (K)
3	30.45
5	35.65
7	39.15
9	41.95
11	44.55

Case C

$q'' \ (W/cm^2)$	ΔT_{pool} (K)
3	36.75
5	39.85
7	41.55
9	42.75
11	43.75

Case D

$q'' \ (W/cm^2)$	ΔT_{pool} (K)
3	59.55
6	77.65
9	84.95

Table D.2: Numerical Results for Nucleation Site Density User-Defined Functions

		$q'' \ (W/cm^2)$			
	Function	3	6	8	9
ΔT_{pool} (K)	NSD: 1a	28.65	31.75	N.S.	33.85
	NSD: 2a	25.35	27.45	N.S.	29.55
	NSD: 3a	21.75	22.95	24.75	N.S.
	NSD: 1b	30.85	33.75	N.S.	35.45
	NSD: 2b	25.25	27.15	N.S.	29.25
	NSD: 3b	21.45	22.75	24.65	N.S.
	NSD: 1a_2	31.35	36.45	N.S.	39.65
	NSD: 2a_2	31.05	34.85	N.S.	37.15
	NSD: 3a_2	30.75	33.25	N.S.	34.85
	NSD: 1b_2	38.65	43.55	N.S.	46.05
	NSD: 2b_2	32.95	36.25	N.S.	38.25
	NSD: 3b_2	26.75	28.85	N.S.	30.35

Table D.3: Numerical Results for Bubble Departure Diameter User-Defined Functions

		q'' (W/cm^2)			
	Function	3	6	8	9
ΔT_{pool} (K)	BDD: 1α, NSD: 1b	30.85	33.95	N.S.	35.95
	BDD: 2α, NSD: 1b	32.05	35.05	N.S	36.85
	BDD: 3α, NSD: 1b	33.25	36.35	N.S.	37.95
	BDD: 1β, NSD: 1b	26.75	29.05	30.25	N.S.
	BDD: 2β, NSD: 1b	27.45	29.75	31.05	N.S.
	BDD: 3β, NSD: 1b	28.25	30.65	N.S.	32.55

Table D.4: Combination of NSD and BDD User-Defined Functions

NSD: 1a_2, BDD: 3α

q'' (W/cm^2)	ΔT_{pool} (K)
3	35.35
6	41.45
9	44.55
11	46.15

NSD: 2a_2, BDD: 3α

q'' (W/cm^2)	ΔT_{pool} (K)
3	34.15
6	38.35
9	40.45
11	41.55
12	42.05

Table D.5: Piecewise Nonlinear Nucleation Site Density User-Defined Functions

NSD: nonlinear_1c, BDD: default

q'' (W/cm^2)	ΔT_{pool} (K)
3	31.35
6	36.45
9	39.65
10	40.15
11	40.65

NSD: nonlinear_1c, BDD: 3α

q'' (W/cm^2)	ΔT_{pool} (K)
3	35.35
6	40.45
9	41.65
10	41.95
11	42.15

Table D.6: Variation of Degree of Subcooling with NSD: nonlinear_1c, BDD: 3α

		q'' (W/cm^2)				
	Subcooling	1	3	6	9	10
ΔT_{pool} (K)	13°C	23.25	32.75	37.85	39.15	39.45
	15°C	23.25	35.35	40.45	41.65	41.95
	18°C	23.25	39.15	44.15	45.45	45.75

Table D.7: Variation of Turbulence Model with NSD: 2a_2, BDD: 3α

		$q'' \ (W/cm^2)$		
	Turbulence Model	3	6	9
ΔT_{pool} (K)	Standard k-ω	32.85	37.05	39.55
	Standard k-ε	34.05	38.15	40.25
	RNG k-ε	34.15	38.35	40.45

D.2 Flow Boiling Numerical Results

This section includes the numerical results from flow boiling simulations of the four die cartridge model in Novec 649. Results include baseline numerical results using all default boiling parameters (Table D.8) and combinations of user-defined functions for nucleation site density and bubble departure diameter (Table D.9). In the tables, N.S. stands for Not Simulated.

Table D.8: Flow Boiling Numerical Results for Built-In Boiling Parameters

$q'' \ (W/cm^2)$	ΔT_{pool} (K)
3	41.15
6	46.65
9	49.85
11	51.55

Table D.9: Combination of NSD and BDD User-Defined Functions (Flow Boiling)

NSD: 2a_2, BDD: 3α

$q'' \ (W/cm^2)$	ΔT_{pool} (K)
3	56.05
6	68.25
9	73.45

NSD: 3b_2, BDD: 3α

$q'' \ (W/cm^2)$	ΔT_{pool} (K)
3	50.15
6	55.95
9	58.35